Application of Diamond Films to Electric Propulsion: Low Energy Sputter Yield Measurement and MPD Plasma Assisted Chemical Vapor Deposition

Thesis by
John J. Blandino

In Partial Fulfillment of the Requirements
for the Degree of
Doctor of Philosophy

California Institute of Technology
Pasadena, California
2001
(Defended April 3, 2001)

Acknowledgments

The work described in this thesis was made possible through support of the Jet Propulsion Laboratory, California Institute of Technology, under contract with the National Aeronautics and Space Administration and the James Irvine Foundation.

I am grateful to my advisor, David Goodwin, for his sustained support for my research over the time it took to complete. His friendship, patience, and guidance are deeply appreciated and made completion of this work possible. John Brophy, who served on my committee and was my JPL supervisor for several years provided invaluable guidance through many discussions and provided critical review of my work on numerous occasions. I am also grateful to my other committee members; Fred Culick and Joe Shepherd from Caltech and Mark Cappelli from Stanford, for their valuable comments, suggestions, and discussions.

During my initial efforts at Caltech, I benefited enormously from the support, advice, and mentoring of more senior graduate students. Nick Glumac, Dave Kaufman, and Ho-Seon Shin always made themselves available if needed and I owe them much for helping me succeed.

I would like to thank Prof. Marc Nicolet of Caltech for use of the ultra-high vacuum sputter deposition facility and Richard Koba of Crystalline Materials Corp. for providing the CVD diamond sample used for the sputter yield measurements. Most of the work described was carried out in the electric propulsion test facilities at the Jet Propulsion Laboratory and there are numerous individuals who provided valuable assistance and advice. I am thankful to Joel Sercel for providing encouragement and support of my efforts to pursue a research program at Caltech. Everyone in the Advanced Propulsion Technology Group has been very supportive with their friendship and advice in all of my years at JPL. Keith Goodfellow provided me with the hands-

on training I needed to safely operate and repair the cathode test facility and was always willing to take time out from his busy schedule to answer my many questions. Charles Garner was very generous with his time to help with the sample profilometry and planning of the erosion tests. Al Owens, Bill Thogmartin, Bob Toomath, and Dennis Fitzgerald were always ready to help with component fabrication and electrical design and taught me practical laboratory technique. I also benefited from numerous discussions on ion engine operation and plume physics with Joe Wang and John Anderson. In completing my thesis, John Ziemer and Olivier Duchemin provided much welcome advice in the use of LaTeX.

It is difficult to overstate how much my friendships with Stephanie Leifer and Jay Polk have meant to me personally and contributed to the successful completion of my dissertation. As my officemate at JPL and later as a fellow graduate student at Caltech, Stephanie was always available to listen to questions, concerns, or just discuss the topic of the day. Jay has been a good friend and mentor for much of my time at JPL. Despite his very full schedule, he has always made the time to patiently listen to any questions or concerns regarding my research and share his technical expertise when needed. As my supervisor, he helped sustain financial support for my research and arrange my JPL workload so that I could complete my thesis. His effort did not go unnoticed and I am more grateful than I can say.

On a more personal note, I would like to thank my wife, Pam, for her unfailing patience and support. I could not have finished without her willingness to put so many plans on hold, and to take on so many of the tasks needed to support our daughters and their schooling. I am indebted to my mother for her never-ending and unconditional support and encouragement. To my Aunt Rita, who to me has been a second mother and calming influence in times of trouble, I thank her for

her encouragement and support, in so many ways for so many years. Finally, I am forever grateful to my brother Peter who introduced me to science and a lifelong love of learning. His continued influence is evident to me in each academic milestone and accomplishment I have ever enjoyed.

Abstract

Progress made in the area of chemically vapor deposited (CVD) diamond films has led to its consideration for a number of novel applications. One potential application under evaluation at the Jet Propulsion Laboratory involves the use of diamond films as coatings for ion thruster electrodes which are subject to sputter erosion. In order to assess their benefit in mitigating sputter erosion as a failure mode it was necessary to first measure the erosion rate compared with molybdenum and carbon-carbon when subjected to ion bombardment.

Sputter yields were measured for polycrystalline diamond, single crystal diamond, a carbon-carbon composite, and molybdenum subject to xenon ion bombardment. The tests were performed using a 3 cm Kaufman ion source to produce incident ions with energy in the range of 150 - 750 eV and a profilometry-based technique to measure the amount of sputtered material. The yields increased monotonically with energy with values ranging from 0.16 atoms/ion at 150 eV to 0.80 at 750 eV for the molybdenum and 0.06 to 0.14 for the carbon-carbon. At 150 eV the yield for both diamond samples was 0.07 and at 750 eV, 0.19 and 0.17 for the CVD and single crystal diamond respectively. In terms of erosion rate, this translates into a factor of 7 - 12 lower erosion rate for diamond compared to molybdenum and at least a factor of 1.5 compared to carbon-carbon.

With the erosion rates established, the remaining effort concentrated on the experimental and analytical investigation of an electromagnetic (magnetoplasmadynamic or MPD) plasma source for diamond CVD using a mixture of methane and hydrogen. Specific questions to be addressed included identifying the implications of higher velocity, dissociation, and ionization levels than those expected in an electrothermal (arcjet) plasma source. An experimental facility was used in which the process condi-

tions produced were representative of the high temperature, ionization, and dissociation levels one would expect from an MPD in an actual reactor although not the high velocity. Numerous trials were conducted using methane to hydrogen mixture ratios of 1.5 - 3.5 percent by volume, four different methane injector configurations, and substrate biasing at potentials of 25 - 75 V positive with respect to facility ground. These tests were performed at discharge currents of 700 - 950 A at approximately 18 V (12 - 17 kW).

Crystalline films were produced with predominantly (110) oriented facets. X-ray diffraction spectroscopy was used to identify at least one unambiguous diamond peak in each sample with numerous films containing metal or metallic carbide impurities. Growth rates of 0.8 to 6.3 μm/hr were measured. The films all exhibited poor Raman spectra with no well defined peak at 1332 cm^{-1} and a broad background possibly due to high background levels of nitrogen, defects, and contamination.

The question of high velocity and high ionization level was investigated analytically using estimated hydrogen MPD plume data from the literature. For conditions expected with an MPD source, Knudsen numbers in the plume are calculated to be approximately 0.1 in the free stream and less than 0.01 (i.e., transition-continuum boundary) in the stagnation boundary layer. The heavy particle static temperature in the plume is expected to be on the order of 10000 K in the core. For Mach numbers in the range 1.0 - 2.0, the stagnation temperature can be expected to reach peak values of over 20000 K. This temperature far exceeds the range of available thermodynamic and transport databases for hydrocarbon mixtures needed to model stagnation boundary layer chemistry and growth rates, so a scaling relation was used to obtain a relative comparison of the atomic hydrogen mole fraction at the substrate for an electrothermal and electromagnetic accelerated plasma source. Because of its

higher jet velocity and lower operating pressure, the electromagnetic source operates in more of a convection dominated regime resulting in a calculated hydrogen mole fraction at the substrate approximately 40 percent higher than that predicted for an electrothermal accelerator.

An energy balance was used to determine an upper bound on the level of electron heating obtainable for a given bias current density. Results show that even for pressures of a few Torr and ionization fractions of 5 - 25 percent, the required current for a few thousand degree increase in electron temperature over the heavy particle gas temperature is on the order of several tens of A/cm^2. From this analysis it is concluded that high plasma conductivity in an MPD plume and electron energy losses through inelastic molecular collisions will preclude the effective use of ohmic heating of the electrons as a means of enhancing electron catalyzed dissociation in the boundary layer.

Estimates were made of the optimal residence time for methane decomposition in the plume in order to maximize the flux of methyl radicals and atomic hydrogen to the substrate; two species which have been identified as having a significant role in high rate, high quality diamond synthesis. At pressures of 100 Pa and 333 Pa, which approximate the pressure in the plume and stagnation regions, there is little recombination of the hydrogen even at a temperature of 5000 K which one could expect well into the thermal boundary layer for an MPD stagnation flow. The methyl mole fraction reaches a maximum at a residence time of 1 - 3 μsec. Achieving adequate entrainment and mixing of the methane in the hydrogen jet on such a short time scale is a very difficult challenge.

Two major conclusions of this thesis are: 1) The lower erosion rate measured for CVD diamond as compared with molybdenum makes coating of grid electrodes with

CVD diamond a possible option for extending the lifetime of ion thrusters worth further investigation. 2) Based on both the experimental and analytical investigation of the MPD source for diamond deposition, the potential for higher growth rates than those obtainable with more conventional plasma sources is not significant enough to offset the disadvantages associated with contamination of the film due to metal vapor from the high current electrodes and poor entrainment of the carbon precursor gas due to the short residence time in the plume.

Contents

List of Figures

List of Tables

Chapter 1

Background and Motivation

1.1 Introduction to CVD Diamond Films

In the last decade there has been a significant increase in research directed towards understanding the synthesis of diamond and diamond-like materials at low pressures from a gas phase carbon precursor. First demonstrated in the 1950s in both the former Soviet Union and the United States, the number of laboratories actively investigating this technique increased rapidly in the 1980s as a result of Japanese advances in identifying a variety of gas activation schemes [1]. Because of its unique combination of thermal, electronic, mechanical, and chemical properties, diamond has seen increasing use in a wide range of scientific and engineering applications. Diamond and other covalently bonded solids are among the hardest known materials making them particularly attractive in the form of thin film coatings for components subject to chemical exposure or mechanical wear. Diamond is transparent in the visible and infrared wavelengths resulting in its application to windows and coatings for sensors required to operate in corrosive or high temperature environments. Diamond has a

thermal conductivity fifteen times that of silicon and five times that of copper at room temperature as well as a very low coefficient of thermal expansion [1].

The relatively recent development of low pressure chemical vapor deposition (CVD) of diamond over areas of many square centimeters has resulted in new potential applications for diamond films. One promising application is that of heat sinks for high power electronic components. Heat sinks require the capability of fabrication in the form of a thin film, either bonded to or directly deposited on the component. For opto-electronic device applications, the quality of the film with respect to defects and impurities is of greater importance than the growth rate. For other applications such as wear resistant coatings and heat sinks, the thickness, area and adhesion properties of the film become more important. Economic production of diamond films for heat sinks and other applications will require successful scaling of the relevant processes to industrial production levels through some form of batch processing.

The basic elements important to low pressure chemical vapor deposition of diamond are depicted in Figure 1.1. A gas phase source of carbon such as methane is introduced into a chamber along with a hydrogen diluent gas. Typically the methane is only a few percent of the total gas flow by volume. Some source of energy is needed to dissociate and activate the gas into various species essential to the growth chemistry. Many activation sources have been employed successfully including a hot filament, oxygen-acetylene flame, RF and microwave induced plasma discharges, and the DC-plasma arc. Some of the gas species which have been found to play an important role in the growth kinetics are indicated in Figure 1.1. While a definitive chemical pathway has yet to be agreed upon, there is widespread consensus that the presence of atomic hydrogen and various hydrocarbon radicals, particularly methyl, play a key role [2–4]. Production of adequate amounts of the atomic hydrogen and

hydrocarbon radical species needed for growth is of fundamental importance for any gas activation scheme. It is believed that atomic hydrogen serves to terminate dangling carbon bonds on the growing surface. These hydrogenated surface sites play an intermediate role in the reactions with methyl radicals which incorporate carbon into the lattice. Atomic hydrogen preferentially etches graphite deposits, resulting in higher quality films. The substrate can be any of a variety of materials with silicon or molybdenum a common choice. Diamond crystallites (isolated diamond crystals which later coalesce into a continuous film) will nucleate on the substrate after a period of time which depends upon numerous variables including substrate temperature, surface preparation (such as scratching with diamond paste) and gas phase species concentrations. As adjacent crystallites grow together, a continuous film is formed. The growth rate of the film will depend on the type of process used but can range from less than a micron per hour for a hot filament reactor to hundreds of microns per hour for DC arcjet plasma sources [5].

1.2 Application of CVD Diamond to Electric Propulsion

There are a number of electric propulsion devices which have been under investigation since the 1960s for space applications. While quite varied in their implementation, these devices all share the common goal of converting electrical power into directed jet power of a propellant gas which has been accelerated to high velocity. Many of these devices necessarily involve the use of materials located adjacent to high temperature plasmas where they are subject to significant thermal loads and in some cases bombardment from energetic ions as well. One such device is the electron bombardment

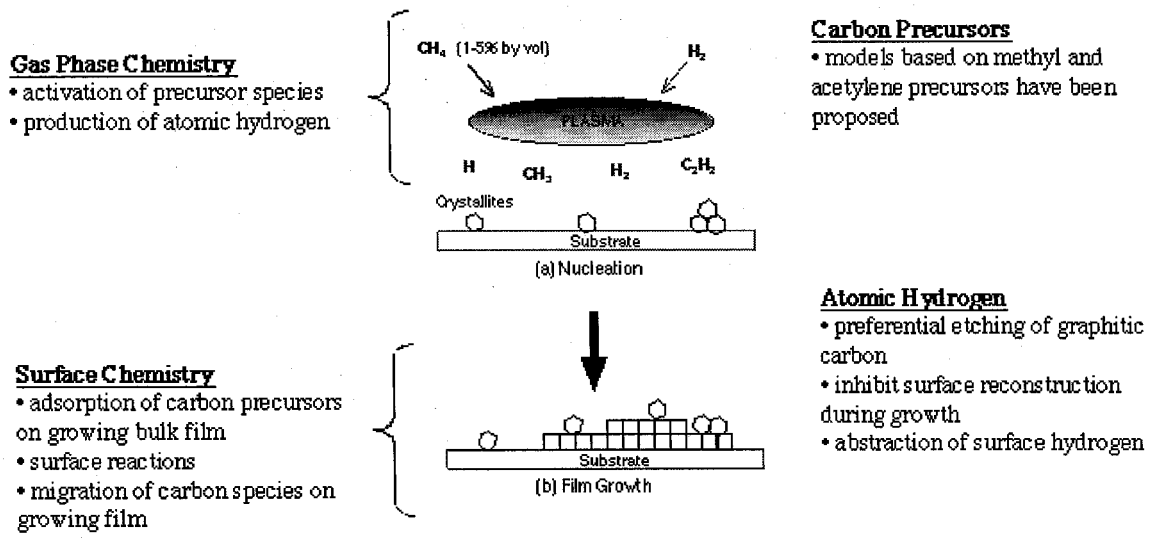

Figure 1.1: Basic processes in low pressure, chemical vapor deposition of diamond film include passing carbon precursor and hydrogen diluent gases through a plasma for activation. This produces atomic hydrogen and hydrocarbon radicals, essential to film deposition, which then proceed to (a) nucleate on substrate followed by (b) growth of the bulk film.

ion thruster such as is currently in use in NASA's Deep Space 1 (DS1) probe. This mission represents the first use of an ion thruster for deep space exploration. Use of these thrusters on extended deep space missions requires operational lifetimes in excess of 10,000 hrs. Extending the lifetime of components subject to ion bombardment in these devices is therefore fundamental to their successful application. As will be shown in Chapter 2, polycrystalline diamond films have the potential of minimizing the life limiting erosion of components from ion sputtering. Before discussing the specific advantages of diamond films for ion thrusters, the basic operation of these devices will be described.

Figure 1.2 is a schematic of an ion bombardment thruster such as the one flying on DS1. Its components serve to provide three basic functions; production of plasma, acceleration of plasma ions to high velocity (typically 30 km/sec), and neutralization

of the resultant beam in order to control the electric potential of the spacecraft. The plasma is produced in a discharge chamber into which the propellant gas is injected. A combination of high atomic mass and low first ionization potential makes xenon an attractive propellant for this application. Electrons are emitted from a centrally located hollow cathode maintained at roughly a kilovolt positive of spacecraft ground potential. Magnets located around the perimeter of the discharge chamber induce helical trajectories in the emitted electrons which travel to the discharge chamber walls maintained at anode potential (roughly 30 V positive of the cathode). The helical paths for the electrons increase their residence time in the discharge chamber resulting in a higher probability of an ionizing collision with a neutral gas atom. The ion optics consist of a positively biased "screen" grid and negatively biased "accelerator" grid forming the downstream boundary of the discharge chamber (some systems have a third "decelerator" grid). These grids are disk shaped structures usually made of molybdenum (as in the DS1 thruster) but can be made of a carbon composite as well. The grids are perforated with thousands of holes roughly 1-2 mm in diameter and are separated by a gap of 0.6 mm. When a potential difference of 1100 - 1300 V is applied across these grids an electric field is established which extracts and accelerates ions from the discharge chamber, emitting them as a collimated beam. Were it not for a separate neutralizer, this beam of positive ions would rapidly result in the negative charging of the spacecraft and subsequent stalling of the beam. This neutralizing function is provided by an externally mounted hollow cathode similar to the one in the discharge chamber. Ion thrusters such as these are capable of imparting significantly greater changes in velocity to a spacecraft for a given mass of propellant as compared with a more conventional chemical thruster.

Work conducted in recent years has significantly improved our understanding of

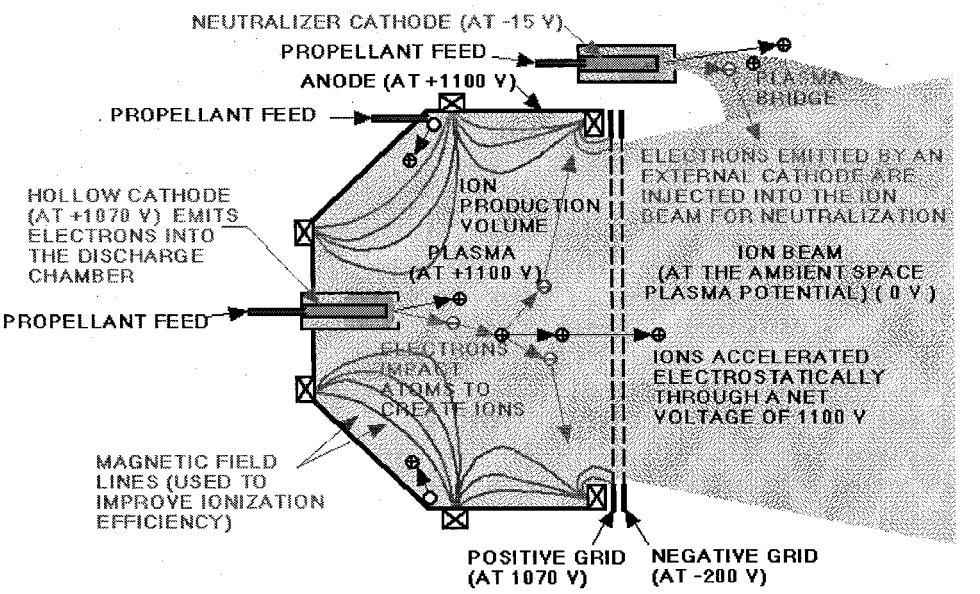

Figure 1.2: Electron Bombardment Ion Thruster

the physical mechanisms which limit the lifetime of ion thrusters. Foremost among these mechanisms is the erosion of the accelerator grid (in two grid optics) from bombardment with charge-exchange (CEX) ions created in a region immediately downstream of the thruster [6, 7]. The physical processes which lead to the production of these ions is illustrated in Figure 1.3 which has been adapted from Monheiser and Wilbur [6]. This figure represents a plot of the axial, centerline plasma potential in the region between and immediately downstream of the two grids. In this plot the horizontal "zero" potential line represents a reference ground which the plasma potential approaches as the beam travels into the far-field downstream (and which can differ from the spacecraft ground by a 10 - 20 V). Because the accelerator grid is biased 100 - 200 V negative of spacecraft ground, the plasma potential will have a dip followed by a small potential hill immediately downstream of the accelerator grid. Energetic ions produced within the discharge chamber have no difficulty surmounting this potential barrier. A separate population of lower energy ions is produced,

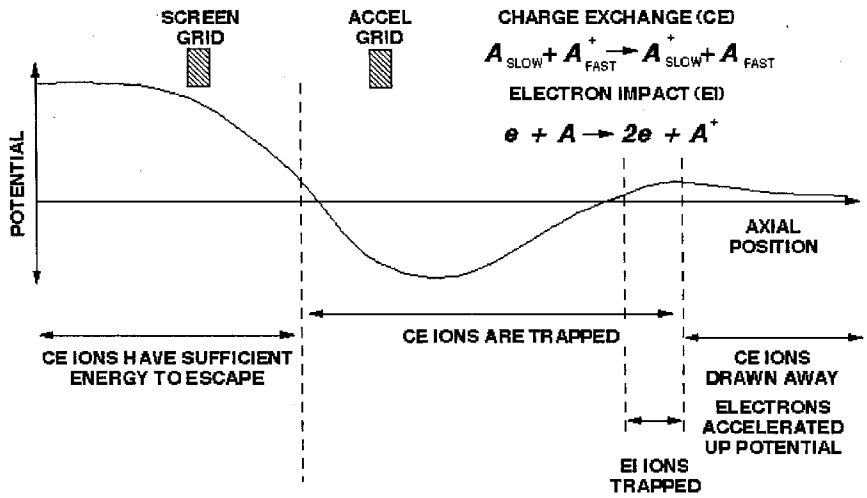

Figure 1.3: Mechanism of charge-exchange ion production in ion thrusters (adapted from Reference [6])

however, by a combination of electron impact and charge-exchange collisions.

Charge-exchange ions are formed when a slow neutral atom collides with a fast ion resulting in a slow ion and a fast neutral. These are produced in a region extending at least a few millimeters downstream of the ion thruster. The source of the slow neutrals is a flux of unionized gas atoms which escape the discharge chamber through the grids. In ground based tests, an additional source of neutrals will be the background gas in the test facility. Several studies have investigated this process and attempted to model it using particle-in-cell (PIC), and Monte-Carlo simulations [8–10]. The slow ions produced in the CEX reactions have insufficient kinetic energy to escape the negative potential well created by the accelerator grid and are accelerated back towards the thruster where they can impinge on the downstream face of the grid or on the hole walls. Over time, this process will lead to the erosion of the webbing between holes in the grid as shown in Figure 1.4 resulting in structural weakening and possibly neutralizer electron back-streaming (i.e. flow of electrons back towards

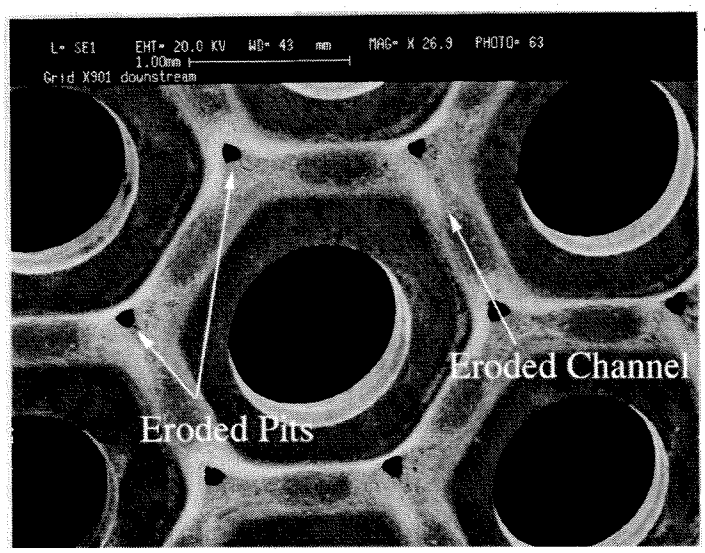

Figure 1.4: Downstream side of an accelerator grid after 900 hr test at 5 kW

the positively biased screen grid). The potential to reduce this erosion has been the primary motivation to incorporate diamond in the fabrication of the grids. The energy range of interest corresponds to the kinetic energy of the CEX ions impinging on the grid which will depend on where they are formed as well as the bias of the accelerator grid. This value will be in the range of 100 - 750 eV depending on the operating point chosen for a particular mission.

As early as the 1960's, efforts to characterize the sputter yield of various elements had identified the improved resistance to erosion of carbon as compared with molybdenum [11,12] when bombarded with xenon and krypton ions. As a result of its lower erosion rate, as well as its negative coefficient of thermal expansion, a program to develop and test ion optics fabricated from carbon-fiber carbon-resin (carbon-carbon) was initiated at the Jet Propulsion Laboratory [13]. More recently, advances in the chemical vapor deposition (CVD) of polycrystalline diamond films prompted an effort to assess the potential benefits of diamond and the feasibility of applying some of

these CVD processes to further improve upon the carbon based grid technology. Two possible strategies were considered to maximize the potential benefit of CVD diamond for thruster grids. Because the primary concern is erosion of the grid exposed to CEX ion impingement, the first strategy involves coating a molybdenum or carbon-carbon grid with a film of diamond. The second involves growing a diamond film grid thick enough (of order 1 mm) to be self supporting. The brittleness of 1 mm diamond film is comparable to that of a graphite panel of the same thickness. The emphasis of this effort would be on the use of diamond for the accelerator grid which is subject to the most severe erosion. However, the same fabrication techniques would be applicable to a screen or decelerator grid. The next section will briefly discuss some thermal, mechanical, and electrical properties of diamond as they pertain to the requirements of the accelerator grid for the ion thruster.

1.2.1 Material Properties Relevant to Ion Thruster Optics

A great deal of interest has surrounded the development of CVD diamond in recent years. Much of this interest is due to the unique combination of desirable properties found in both natural diamond as well as high quality polycrystalline diamond deposited from a vapor phase. Three of the properties most relevant to the application of diamond to ion optics are discussed below.

Thermal Conductivity

In an ion thruster operating using a hollow cathode electron source in the discharge chamber, the thermal environment to which the grids are subjected will be dominated by the cathode and the plasma created within the discharge chamber. Once the thruster is in steady state operation, the cathode temperature will be close to 1100

Material	κ $(W/m/K)$	Notes:
Molybdenum	138	@ 293 K, Ref: [13]
P-100	520	@ 294 K, Ref: [13]
Diamond	2000	@ 293 K, Ref: [1]
Copper	401	@ 293 K, Ref: [1]

Table 1.1: Thermal conductivity of candidate grid materials

C while the discharge chamber walls will be less than 300 C. While the screen grid will shield a fraction of this radiant heat from the accelerator grid, the temperature could still reach a value of 200 - 300 C unless the heat is removed. In addition, the accelerator grid will be subject to heating from impingement of CEX ions on the downstream face, although this is a small heat flux, on the order of a Watt. Heat is removed from the grid by radiation as well as conduction to the thruster body. To the extent possible, one would like to maximize the conduction in order to lessen the radial temperature gradient and therefore the degree to which the grid will distort due to thermal expansion. Table 1.1 lists the room temperature thermal conductivities of molybdenum, P-100 (a commercially available carbon fiber used in the fabrication of carbon-carbon composite panels), diamond and copper.

Coefficient of Thermal Expansion

As previously mentioned, heating of the accelerator grid results in a deflection as a result of the radial thermal expansion. This is a consequence of the fact the grid is rigidly fixed in the mounting ring along its perimeter. For a given steady state temperature during operation one would like to minimize this distortion. One reason is that the deflection of the grid surface will alter the spacing between the grids which is approximately 0.5 mm. Changes in the spacing will alter the attainable beam

Material	α $(10^{-6}/K)$	Notes:
Molybdenum	5.43	@ 800 K, Ref: [13]
P-100	-1.5	@ 800 K, Ref: [13]
Diamond	3.8	@ 800 K, Ref: [1]

Table 1.2: Coefficient of Thermal Expansion of candidate grid materials

current for a given beam voltage and if severe enough could result in more frequent arcing or even contact between the grids. Table 1.2 lists the Coefficient of Thermal Expansion (CTE) for molybdenum, P-100, and diamond. The P-100 composite is the most desirable in this respect because of its negative CTE. A negative CTE implies a contraction of the material upon heating which will tend to stiffen the grid making it more rigid. Although diamond is seen to have a CTE thirty percent lower than that of molybdenum, it is high enough that dishing of the grid would probably still be required.

Electrical Resistivity

Diamond has a band gap of 5.5 eV making it an excellent electrical insulator with a breakdown field of 10^9 V/m. Chemically vapor deposited diamond is routinely doped with boron to make it a p-type semiconductor. It is more difficult to make a n-type semiconductor although this has also been attempted with mixed results by implantation of ions such as carbon or doping with phosphorus [14, 15]. Ideally, the electrical current which must be conducted by the accelerator grid is only that due to CEX ion impingement and should not exceed tens of milliamperes at a grid bias of several hundred volts. As the data in Table 1.3 illustrate, the resistivity of diamond films can span many orders of magnitude depending on the level of doping. Much of the resistivity data available for diamond is for homoepitaxial structures used in

Material	ρ ($\mu\Omega/K$)	Notes:
Molybdenum	0.052	@ 273 K, Ref: [17]
P-100	2.5	@ 294 K, Ref: [13]
Graphite	13.8	@ 273 K, Ref: [17]
Diamond		@ 300 K, Ref: [16]
	25	heavily doped: $n_{boron} = 10^{22} cm^{-3}$
	10^8	lightly doped: $n_{boron} = 10^{19} cm^{-3}$

Table 1.3: Electrical resistivity of candidate grid materials

device research. The data in Reference [16] and shown in Table 1.3, for example, is for films deposited on diamond substrates. Nevertheless, the range of values is representative of what can be achieved even for polycrystalline films. Because the currents involved are small and the effect of resistive heating will be mitigated by the high thermal conductivity, the attainable resistivity for diamond films should not pose a problem.

1.2.2 Application of Diamond to Grid Technology

Diamond Coated Molybdenum Grid

Molybdenum is commonly used successfully as a substrate for diamond deposition. In addition molybdenum has been used in the fabrication of ion thruster grids for many years. For these reasons deposition of diamond directly on a molybdenum grid to form a coating emerged early as an option to obtain some of the benefits of diamond. The advantages of this scheme include the structural rigidity afforded as a result of the metal. In this case the diamond acts primarily as a sputter resistant coating which may be only a few tens of microns in thickness. A sample of molybdenum grid material from an older generation ion thruster (3 mm hole diameter) was used in one experiment to evaluate the growth of diamond film in the region along the

walls within the holes and on the face of the webbing. This deposition was performed in an oxygen-acetylene flame diamond synthesis reactor by H. Shin at Caltech. In this reactor, the substrate sits directly below a planar flame during deposition. The gas flows downward at the substrate resulting in a stagnation flow. The flow geometry establishes a species concentration boundary layer above the substrate through which methyl and atomic hydrogen can diffuse to the growing film surface. This diamond coating was deposited during a three hour deposition run using an oxygen to acetylene ratio of 1.17 and a burner-substrate distance of 1 cm. The substrate temperature during the deposition was approximately 900 C. The SEM image in Figure 1.5(b) shows a region adjacent to one of the holes. The spherical features within the hole are probably non-diamond carbon while the crystalline structures on the face of the webbing 1.5(c) and seen at higher magnification in Figure 1.5(d) are probably diamond. A definitive determination would require additional analysis such as X-Ray diffraction or Raman spectroscopy. The presence of the non-crystalline deposits in the hole suggest the lower temperatures and/or gas species concentrations unfavorable for diamond formation. The erosion due to CEX ion impingement is expected to occur in both the webbing between holes as well as in the hole walls. The formation of diamond on the webbing surface as evident in Figure 1.5 was encouraging although the amorphous coating on the hole walls is likely to be less effective in minimizing erosion.

One disadvantage of coating molybdenum with diamond stems from the differing CTE. As a molybdenum substrate is allowed to cool after deposition of a diamond film, the film usually peels off as a result of the differing amounts of contraction. This could be a concern given the thermal cycling to which an ion thruster grid would be subject during a mission. However, one of the most important applications

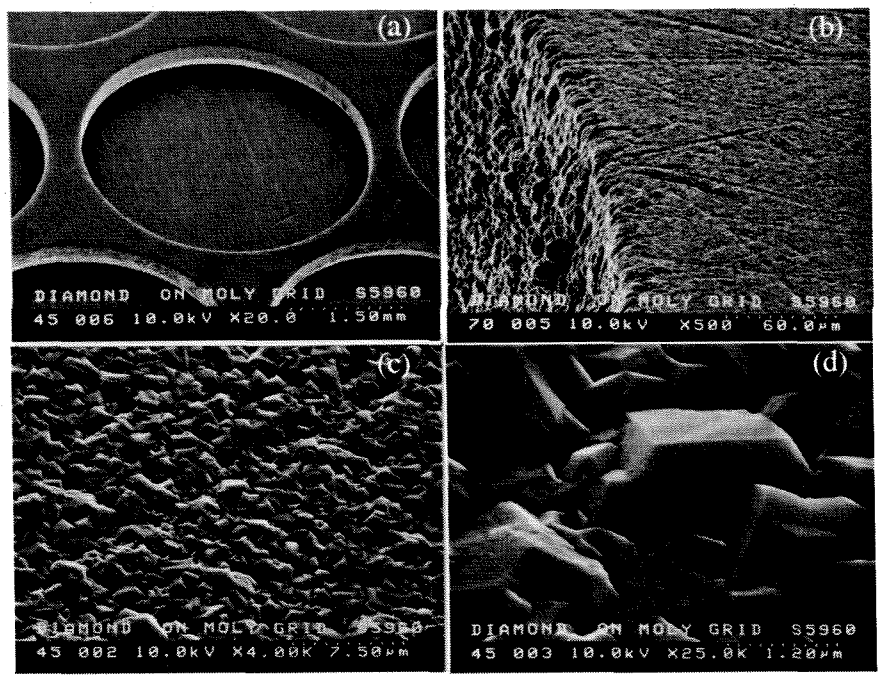

Figure 1.5: Diamond film deposited on molybdenum ion thruster grid: (a) 20 X overview of 3 mm holes, (b) 500 X transition from crystalline film on webbing between holes to "ball" like structures lining inner wall of hole, (c) 4000 X, crystalline film on webbing area, (d) 25,000 X close-up of crystallites (Film deposited by H. Shin of Caltech using an oxygen-acetylene flame reactor)

of diamond coatings is for machine tool bits which are subject to thermal cycling under much more severe mechanical stresses. The adhesion can be improved by using interlayers between the diamond and metal. Molybdenum carbide is one example [18].

Free Standing Diamond Grid

A second fabrication option is to deposit a thick film which is self supporting. Such a free-standing diamond grid would have some important advantages over the diamond coated molybdenum. One advantage is that the adhesion is not an issue. A second advantage is that the CTE for the grid is lower since it is not restricted to that of its metal backing. A significant drawback of the free standing grid is the loss of flexural

rigidity obtained from the molybdenum. Polycrystalline diamond is exceedingly hard but also brittle. Thus far no information has been found quantifying the flexural rigidity of free standing CVD diamond films but small samples, even those approximately a millimeter thick, are fragile and require careful handling. The process for growing a free-standing grid would essentially be the same as the coated molybdenum except the film grown would have to be hundreds or thousands of microns thick and poor adhesion would be desirable in order to remove the diamond from its substrate. It may be possible to grow the diamond on a substrate with holes in order to produce a grid with holes. However, because of the thickness involved, the diamond film may grow laterally as well as vertically, thereby closing off the holes. If this is the case it would then be necessary to first produce a free-standing diamond disk, and then machine the holes (with a laser for example). An alternative to deposition on a molybdenum substrate (with or without holes) is to deposit the diamond film on a silicon substrate which has been patterned with silicon dioxide using standard lithographic techniques. The benefit here is that the film will be selectively deposited on the silicon and not on the oxide. In this way it is possible to pattern the wafer with oxide "dots" where the grid holes are supposed to be. Because the diamond nucleation density on SiO_2 is several orders of magnitude lower than on Si, the oxide essentially inhibits the growth. Once the film has been deposited, the substrate can be removed with an acid. While this approach involves more process steps, it may be desirable if the separation of the diamond from a molybdenum substrate with holes is difficult to accomplish without damaging the webbing between the holes.

Diamond Coated Carbon-Carbon Grid

One last promising option which has only received a limited amount of attention is that of coating a carbon-carbon grid with diamond film. This scheme has the advantage of potentially incorporating many of the benefits of carbon-carbon and diamond. In particular, the carbon-carbon panel provides the flexural rigidity as in the coated molybdenum case but does not suffer from the relatively high CTE. Deposition of diamond has been demonstrated on carbon fiber composites with the crevices between adjacent fibers providing favorable nucleation sites. However, because carbon-carbon has a negative CTE, the adhesion issue for thicker films could pose a problem.

1.3 Summary

This Chapter has presented a brief description of key processes in the low pressure chemical vapor deposition of diamond films. Some of diamond's desirable properties from an engineering standpoint were discussed with attention focusing on the potential application of diamond films to extend the life of ion thruster optics subject to ion bombardment. Assessing the real benefit of diamond for this application required a knowledge of the sputter yields of diamond film subject to xenon ion bombardment in an energy range of interest for these devices. This data was not available and so the first task undertaken as part of this thesis was the characterization of these yields. This series of experiments and results are the subject of Chapter 2. It will be shown that diamond has a lower erosion rate compared to molybdenum which is the current material in use for these thrusters. Having established the potential benefits, the research evolved into an assessment of techniques for high growth rate synthesis.

The highest growth rates to date have been recorded with DC arcjet assisted

CVD, and a description of this device along with a review of work performed using this technique over the last fifteen years is presented in Section 3.1. Several characteristics of another plasma source, the magnetoplasmadynamic or MPD arc, suggest it could provide substantial benefits upon scaling up to the power levels and substrate areas of interest to industry. This device will also be described in Section 3.2 along with a review of the limited published data available on application of the MPD to materials processing. Chapter 4 presents results of the first attempts to use an MPD specifically for diamond deposition. Understanding application of the MPD to diamond synthesis requires a closer evaluation of the jet characteristics unique to this device. Chapter 5 will present a comparison of the arcjet and MPD sources for diamond CVD with particular attention to the benefits (or drawbacks) from higher velocity and ionization level. The Chemkin package of chemical kinetic analysis software is used to look at methane pyrolysis in order to estimate optimal residence times for methane in the plume. These results are also presented in Chapter 5. Final conclusions as to the applicability of the technique and its application are presented in Chapter 6.

Chapter 2

Low Energy Sputter Yield Measurements

2.1 Introduction

Improvements in quality, reproducibility, and growth rates have made diamond films attractive for a variety of applications in the fields of electronics, optics, and tribology among others [19–21]. As discussed in the last chapter, one potential application under evaluation at the Jet Propulsion Laboratory involves the use of diamond films as coatings for ion thruster electrodes which are subject to sputter erosion [22]. A number of studies have examined the sputtering characteristics of both single crystal and polycrystalline diamond at incident ion energies less than 2.0 keV. Most of these have used argon [23–28] as the incident ion species with some work also evaluating neon [27,29] and oxygen [23,25,30–32]. One study considering the role of nitrogen in the reactive etching of diamond also used 2 keV xenon ions [33].

Different experimental approaches used to quantify removed material have in-

cluded profilometry to measure eroded depth profiles as well as direct mass loss measurements. A variety of ion sources have also been used including immersion of a self biased target into an RF plasma, and externally accelerated ion beams using Kaufman and ECR sources. While most of these studies involved exposure of the samples to energetic ions at normal incidence, a systematic evaluation of the incidence angle dependence of the yield of the (100) face of single crystal diamond subject to argon ion bombardment has also been reported [23]. In the present paper, results for the sputter yield and corresponding erosion rate of diamond subject to xenon ion bombardment at energies of 150, 250, 500, and 750 eV are presented. The yield and erosion rate for molybdenum and carbon-carbon composite, both in use as electrode materials for ion thrusters, were also determined.

2.2 Experiment

The experimental approach consisted of exposing selectively masked areas of the different samples to an ion beam for a prescribed period of time. The depth of the resulting eroded valley can then be measured to calculate the number of atoms removed due to ion sputtering. A probe located adjacent to the samples records the beam current density which can then be integrated to determine the incident ion dose. During exposure of the samples it is important to minimize the influence of residual facility gases. Previous work suggests that the presence of nitrogen can lower the erosion rate of metals [34] whereas oxygen in the presence of energetic ions can reactively etch diamond [31, 32]. In tests by Efremow et al. [33], a NO_2 gas jet is directed towards a diamond surface while the target is under bombardment with 2 keV xenon ions which provide the activation energy required to form CO and CO_2

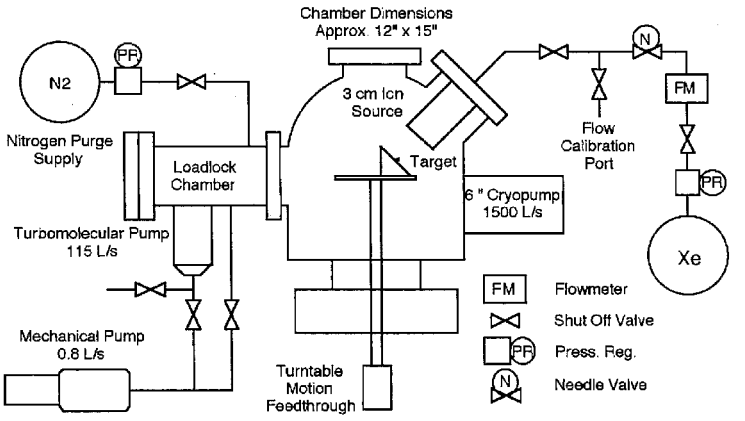

Figure 2.1: Schematic of the Ultra-High-Vacuum test facility

volatiles. Minimizing contamination is therefore essential to obtain accurate sputter yields. The system used was an ultra-high-vacuum chamber with a 3 cm Kaufman ion source (Commonwealth Scientific Corp.) normally used for sputter deposition. The ultra-high-vacuum system is shown in Figures 2.1 and 2.2.

The system is pumped with a turbomolecular pump (115 l/sec) backed by a small mechanical pump (0.8 l/sec) down into the 10^{-4} Pa (10^{-6} Torr) range and then with a 6" cryopump (1500 l/sec) to the 10^{-7} Pa (10^{-9} Torr) range. The base and test pressures for each of the cases are summarized in Table 2.1. In addition, the chamber was baked at over 100 C every evening for several hours. The samples were located approximately 6.7 cm downstream of the source exit plane. Although a greater source-target distance would be desirable to achieve a more uniform incident flux, the distance used was constrained by the chamber dimensions (approximately 30 cm high by 38 cm in diameter). The experimental approach included centering the probe on the point of maximum current density in the beam which was subject to some drift over the duration of each test. This was accomplished through a combination of vertical translation and rotation of the sample platform (see Figure 2.1).

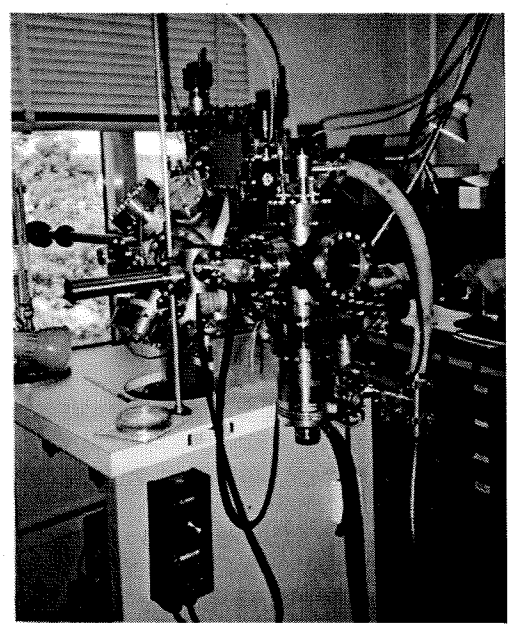

Figure 2.2: Photograph of the Ultra-High-Vacuum test facility used for sputter yield measurements

Energy	Base Pressure	Test Pressure	j_{ave} Moly, C-C, CVD Diam.	j_{ave} Sing. Cryst. Diam.	Incidence Angle
(eV)	(Torr x 10^9)	(Torr x 10^4)	(mA/cm^2)	(mA/cm^2)	(deg)
150	7.7	2.1	0.6 ± 0.1	0.6 ± 0.1	12
250	1.1	2.1	1.4 ± 0.2	1.4 ± 0.2	12
500	11.0	2.1	3.1 ± 0.7	3.0 ± 0.7	15
750	2.3	2.1	4.6 ± 1.1	4.4 ± 1.1	9

Table 2.1: Base and test pressures, average current densities at the target, and the time averaged incident angles: Uncertainty in incidence angles can be approximated by the beam divergence to be $\pm$ 5-10 degrees

Table 2.1 lists the calculated incidence angles for the four tests assuming the beam originates at the center of the source exit plane and terminates at the center point of the probe. Because the probe position is adjusted slightly at various times throughout the test to insure it is located at the point of maximum current density, the incidence angles reported in Table 2.1 have been time averaged over the duration of each test. The samples used in the test were mounted on a fixture and covered with a tantalum foil mask designed to expose only a limited portion of the target to the beam. After the exposed area of the samples had been eroded, the depth of the eroded valley in the target material was measured with a profilometer. The CVD diamond sample used was commercially produced in a DC arcjet CVD process and polished (on one side) to a mirror finish. Since only one sample was available for these measurements, it was rotated between tests to expose different areas. Two of the tests (at 150 eV and 250 eV) were performed on the unpolished side of the sample. Most of the single crystal diamond samples had (110) oriented surfaces. A (100) oriented sample was also used. These diamond samples were 2 mm diameter, 0.27 mm thick disks produced commercially.

2.3 Analysis

2.3.1 Number of Sputtered Target Atoms

A key assumption inherent in the use of a profilometer to estimate the number of atoms removed from the target is that the eroded valley depth corresponds to an averaged volume removed per unit area where in fact it only represents the eroded profile at the location where the trace is taken. A true average would require multiple profilometer scans and then an integration of the "slices" to calculate the eroded

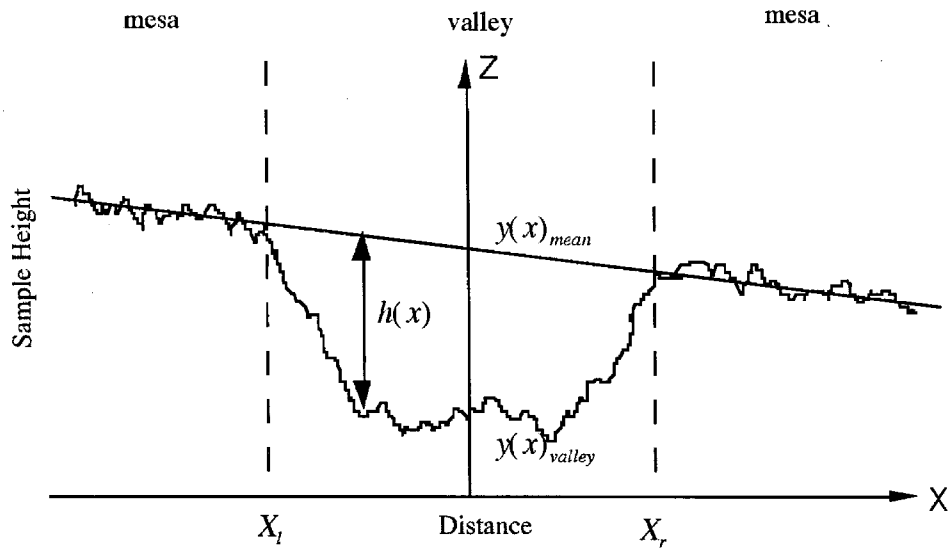

Figure 2.3: Diagram of eroded region on samples showing relationship between mesa and valley regions

volume. The relevant dimensions used in the calculation of eroded depth are illustrated in Figure 2.3. Measuring the depth only at the center of the valley does not adequately take into account the profile of the valley walls which may not be vertical. It was found that the valleys in molybdenum tended to have more vertical walls than the ones in polycrystalline diamond, in which the valley walls sloped gently. In order to calculate a sputtered volume per unit of exposed surface area, a mean effective depth is first defined on the basis of the measured depth profile according to

$$h_{eff} = \frac{1}{(X_r - X_l)} \int_{X_l}^{X_r} (y(x)_{mesa} - y(x)_{valley}) dx \tag{2.1}$$

The traces obtained from the profilometer were scanned into a computer and digitized. In addition to facilitating the integration in Equation 2.1, this digitized mesa-valley-mesa profile could be subjected to statistical analysis to quantify surface roughness. A least-squares line fit through the mesa points establishes a datum,

$y(x)_{mesa}$, from which the valley depth at each x location can be measured. The effective depth h_{eff} is then used to calculate the volume of material removed per unit surface area. The shape of the opening in the tantalum mask determined the geometry of the exposed sample area and hence the eroded volume. For the molybdenum, carbon-carbon, and CVD diamond samples the eroded volume was a linear channel. For these cases the cross section depicted in Figure 2.3 represents a slice across the width of this linear channel whose long axis extends into the page. For this geometry the removed volume per unit of exposed surface area is equal to the effective depth given by Equation 2.1:

$$h_{V/A} = h_{eff} \tag{2.2}$$

For the single crystal diamond samples, the opening in the tantalum mask was a circle producing an eroded volume which was roughly cylindrical. This volume could be estimated by revolving either half of the cross-sectional area represented in Figure 2.3 about the axis of revolution (Z-axis). For this geometry the removed volume per unit of exposed surface area is given by

$$h_{V/A} = \left(\frac{4r_c}{X_r - X_l}\right) \tag{2.3}$$

where r_c is the perpendicular distance from the axis of revolution to the centroid of the cross-sectional area. Once the removed volume per unit area has been determined, the number N_A of target atoms removed per unit area is given by

$$N_A = \rho h_{V/A} \frac{N_{avo}}{M} \tag{2.4}$$

where N_{avo} is Avogadro's number, M, the target molecular weight, and ρ, the target density. The values for the sample density used in calculating the yields were 10.2

g/cm^3 for molybdenum, 1.65 g/cm^3 for carbon-carbon, and 3.5 g/cm^3 for the CVD diamond. The CVD diamond sample was a square roughly 1 cm on a side and less than a millimeter thick. It had a chip and some cracks which made a volume estimate difficult to obtain accurately. For this reason the density was estimated to be that of single crystal diamond. SEM imaging of the sample did not reveal any evidence of porosity, suggesting this assumption is valid within the experimental uncertainty. The density of the CVD sample cannot exceed that of single crystal diamond. If the density is lower, the sputter yield calculated using Equation 2.4 will be lower as well.

2.3.2 Incident Dose of Energetic Particles

The ion current incident on the target was measured and recorded throughout the test using a planar probe. The probe surface was a 1.6 mm diameter tungsten disk which was biased to 25 V below facility ground to ensure operation in the ion saturation regime. There are several factors which affect the incident ion dosage estimate and contribute to the experimental uncertainty in the reported measurements. These include secondary electron emission from the probe, thermal charge-exchange ions and energetic neutrals incident on the probe, collection of doubly ionized gas atoms, and non-uniformity of the beam current density. Each of these will be discussed in the following paragraphs.

Secondary Electron Emission

Because a secondary electron emitted from a current probe is indistinguishable from an arriving ion, operation either at high energies or with probe materials with a high secondary electron emission coefficient requires a correction. In this work, the measured current was corrected for secondary electron emission using data from Ref-

erence [35]. For a tungsten probe with ion energies below 1 keV, this correction is small (< 1.5 percent).

Thermal Charge-Exchange Ions and Energetic Neutrals

Charge-exchange collisions occur when an energetic ion exchanges an electron with a thermal neutral producing a thermal ion and an energetic neutral. These collisions can occur between atoms of the same species (symmetric resonant collisions) or between atoms of different species (asymmetric nonresonant collisions) [36]. Fast neutrals will sputter the target but will not be accounted for in the current measurements while thermal ions may be collected by the current probe but are likely to be below the sputter energy threshold of most target materials. Whether the contribution of charge-exchange ions is relevant for a particular experiment depends in large part on the type of ion source used. When a self-biased sample is placed in an RF plasma, for instance, the ions will gain their energy as they accelerate through the sheath. Because the sheath thickness is likely to be small relative to the mean free path for charge-exchange collisions, it is unlikely a significant population of energetic neutrals would be produced. For a Kaufman source the energetic ions travel through several centimeters of neutral gas before reaching the target. Because the base pressure for these tests was relatively low ($\approx 10^{-9}$ Torr), the dominant source of gas atoms available to become charge-exchange ions will be the neutral xenon from the discharge chamber, a fraction of which will drift out through the grids and into the beam. The ratio of the beam current to the total gas mass flow rate (expressed as a current) is defined as the gas utilization efficiency. For commercial ion sources used primarily for sputter deposition (as opposed to propulsion), this efficiency can be quite low resulting in significant loss of neutral gas through the grids. For each of the four

cases presented here, this efficiency was less than ten percent. For this reason, a correction must be made to avoid over (or under) estimating the dosage of energetic sputtering ions (or atoms). The total current collected at the probe is given by

$$J_p = J_b(1 + \gamma_2) + J_{cex} + \gamma_2 J_n \tag{2.5}$$

where J_b is the energetic beam ion current, γ_2 the secondary electron emission coefficient, J_{cex} is the charge-exchange ion current incident on the target (i.e., the flux of thermal charge-exchange ions reaching the probe) and $\gamma_2 J_n$ is the current registered as a result of secondary electrons emitted when an energetic neutral atom arrives at the probe. In this last term, the flux of energetic neutral atoms has been expressed as an equivalent current. The combined equivalent current of energetic particles striking the target will consist of both beam ions and energetic neutrals:

$$J_{energetic} = J_b + J_n \tag{2.6}$$

Solving Equation 2.5 for the beam ion current and substituting into Equation 2.6 the energetic particle current can be rewritten as

$$J_{energetic} = \beta J_p \tag{2.7}$$

where the factor β evaluated at the target axial location is given by

$$\beta = \frac{\left(1 + \frac{J_n}{J_b}\right)}{1 + \frac{J_{cex}}{J_b} + \gamma_2 \left(1 + \frac{J_n}{J_b}\right)} \tag{2.8}$$

Because one is really interested in dosages, the currents are integrated over the exposure time τ to obtain an expression for the total delivered energetic particle dosage per unit area N_E :

$$N_E = \frac{\beta}{eA_p} \int_0^\tau J_p(t)dt \tag{2.9}$$

where A_p is the collection area of the probe used to measure the incident ion current. By removing the β factor from inside the integral, we have neglected any time dependence of the current ratios in Equation 2.8. To evaluate the above integral for the energetic particle dosage, the charge-exchange ion and energetic neutral ratios used in Equation 2.8 must be determined independently. To estimate these ratios, a simple one-dimensional model for the plume was developed. In this model the plume is assumed to spread out at some fixed divergence half-angle. At the source exit plane, a flux of beam ions and thermal atoms drift axially downstream where charge-exchange collisions are assumed to occur. Some beam ions will be converted to charge-exchange ions which are then assumed to form a Maxwellian population at a temperature representative of the ambient gas in the vacuum chamber, T_a . These ions drift isotropically at the thermal velocity and can therefore escape the control volume radially. This is a substantially simplified representation of the process in which CEX ions are lost from the plume. A more accurate representation, such as one might obtain through a particle-in-cell numerical simulation, would capture the acceleration of the CEX ions in a pre-sheath and sheath at the beam edge boundary. The ion density and plasma potential gradients through the sheath would be solved self-consistently such that the ions exit at the Bohm velocity.

Beam ions and energetic neutrals produced in charge exchange collisions are assumed to travel with a velocity v_b given by

$$v_b = \sqrt{\frac{2e\phi_b}{m_i}} \tag{2.10}$$

where ϕ_b is the potential difference through which the ions are accelerated. This po-

tential is approximately equal to the beam voltage of the Kaufman source. Assuming only single ions are present (as discussed later) the average beam ion density right at the source exit plane is given by

$$n_{bo} = \frac{J_{bo}}{ev_b A_g} \tag{2.11}$$

where J_b is the total beam ion current at the source exit plane and A_g is the accelerator cross-sectional area. Because of low scattering angles, the energetic neutrals produced in these collisions are assumed to continue in their original direction with the same energy [36]. A consequence of this assumption is that energetic particles, whether ions or neutrals, are not scattered out of the control volume. In addition to producing energetic neutral atoms, the charge-exchange collisions also produce thermalized ions with a velocity v_{th} corresponding to the ambient temperature of the gas in the chamber T_a :

$$v_{th} = \sqrt{\frac{8kT_a}{\pi m_i}} \tag{2.12}$$

The volume occupied by the beam between the exit plane and the target establishes a control volume throughout which the continuity of beam and charge-exchange ions is imposed (i.e., no recombination). From the requirement of continuity and again assuming only single ions, a pair of equations for the beam and charge-exchange ion number density were derived:

$$\frac{dn_b}{dz} = -n_b n_n \sigma - n_b \frac{2\lambda}{r} \tag{2.13}$$

$$\frac{dn_{cex}}{dz} = 4 n_b n_n \sigma \left(\frac{v_b}{v_{th}}\right) - n_{cex} \frac{2(\lambda + 1)}{r} \tag{2.14}$$

In these equations, σ is the cross section for charge exchange ion production (singly ionized from ground state), n_b, n_{cex}, and n_n are the beam ion, charge exchange ion, and neutral gas number densities respectively, and λ is a bean divergence parameter given by

$$\lambda = \tan(\alpha) \tag{2.15}$$

where α is the beam half-angle. In Equation 2.13 for the beam ions, the first term represents the loss of ions through collisions while the second term represents the reduction in density due to the expansion of the beam. Similarly, in Equation 2.14 for the charge-exchange ions, the first term represents the production of thermal ions through collisions while the second term includes both the reduction in density due to beam expansion as well as the loss due to radial drift out of the control volume. The absence of a plasma potential in the second term of Equation 2.14 is a consequence of the assumption of a purely axial variation in ion density (i.e., uniform radial density distribution consistent with the simplifications discussed earlier with regard to the Bohm velocity). The gas utilization efficiency previously mentioned is given as the ratio of the beam current to the mass flow rate $\dot{m}$ expressed as a current:

$$\eta_u = \frac{J_{bo}}{\left(\frac{\dot{m}}{m_i}\right) e} \tag{2.16}$$

This efficiency can then be used to determine the neutral density assuming free molecular flow at the source exit plane n_{no} :

$$n_{no} = \frac{4 J_b}{e v_{thd} A_g \phi_o} \left(\frac{1 - \eta_u}{\eta_u} \right) \tag{2.17}$$

where v_{thd} is the thermal velocity based on the temperature in the discharge chamber (Equation 2.12 with $T = T_d$, the temperature in the discharge chamber), and ϕ_o is

the open area fraction for the accelerator grid (equal to 0.45 for the source used). The mean free path for elastic scattering of neutral atoms will be on the order of several meters. Therefore, the energetic neutrals resulting from charge-exchange collisions are assumed to preserve their original direction. Upon solving for the centerline beam ion flux, the fast neutral flux at the target position can be calculated as well by requiring that directed energetic particles be conserved. Equations 2.13 and 2.14 assume a superimposed background neutral density distribution n_n . A centerline neutral density distribution derived for an ion thruster in Reference [37] was used for this analysis. The background neutral density function includes a decaying term representing gas drifting through the source accelerator grid as well as a constant term representing the ambient background gas pressure in the chamber:

$$n_n = \frac{1}{\left(1-\frac{1}{\sqrt{2}}\right)}\frac{n_{no}}{2}\left(1-\frac{1}{\sqrt{1+\left(\frac{r_t}{z}\right)^2}}\right)+n_{na} \tag{2.18}$$

Before solving for the required ratios in Equation 2.8, Equations 2.13 and 2.14 were re-written in nondimensional form. All number densities were normalized to the exit plane beam ion number density given by Equation 2.11, and all distances normalized to the thruster radius r_t :

$$\tilde{n}_b = \frac{n_b}{n_{bo}}, \tilde{n}_n = \frac{n_n}{n_{bo}}, \tilde{n}_{cex} = \frac{n_{cex}}{n_{bo}}$$

and

$$\tilde{z} = \frac{z}{r_t}, \tilde{r} = \frac{r}{r_t}$$

where $\tilde{r} = 1 + \lambda\tilde{z}$. With these definitions, the non-dimensional equations can be written as

$$\frac{d\tilde{n}_b}{dz} = -\tilde{n}_b\tilde{n}_n(n_{bo}r_t\sigma) - \tilde{n}_b\frac{2\lambda}{\tilde{r}} \tag{2.19}$$

$$\frac{d\tilde{n}_{cex}}{dz} = 4\tilde{n}_b\tilde{n}_n(n_{bo}r_t\sigma)\left(\frac{v_b}{v_{th}}\right) - \tilde{n}_{cex}\frac{2(\lambda+1)}{\tilde{r}} \tag{2.20}$$

Solving Equations 2.19 and 2.20 requires some assumption regarding boundary conditions. At the source exit plane, one expects that no significant amount charge exchange ions have yet been produced and the beam ion density is given by Equation 2.11. The boundary conditions would therefore be

$$\tilde{n}_b[\tilde{z} = 0] = 1 \tag{2.21}$$

$$\tilde{n}_{cex}[\tilde{z} = 0] = 0 \tag{2.22}$$

The model assumes the thermal charge-exchange ions can drift upstream. In reality some will be accelerated upstream towards the negatively biased downstream grid. As a result the boundary condition given by Equation 2.22 is more likely to be a number close to but not equal to zero. This uncertainty is factored into the uncertainty estimates in the reported data discussed below. Once Equation 2.19 - 2.22 have been solved, the ratios needed for Equation 2.8 are given by

$$\frac{J_n}{J_b} = \left(\frac{1 - \tilde{n}_b\tilde{r}^2}{\tilde{n}_b\tilde{r}^2}\right) \tag{2.23}$$

$$\frac{J_{cex}}{J_b} = \frac{\tilde{n}_{cex}}{4\tilde{n}_b}\left(\frac{v_{th}}{v_b}\right) \tag{2.24}$$

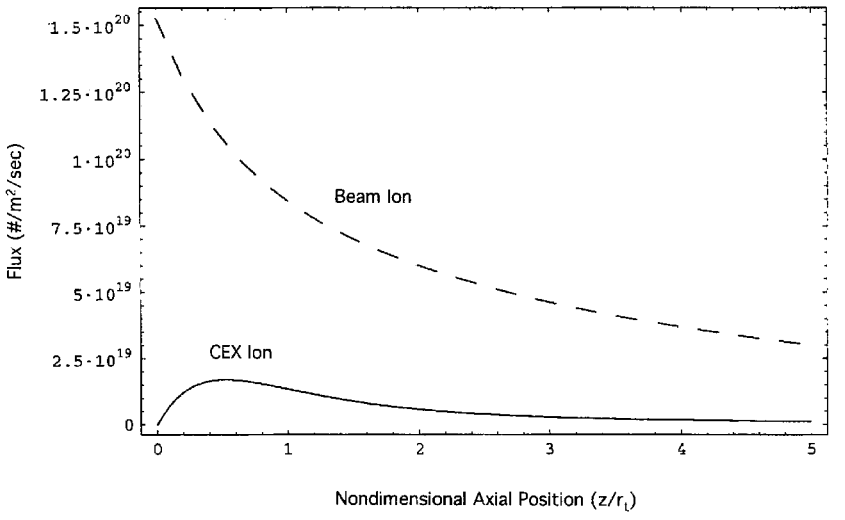

Figure 2.4: Calculated charge-exchange and beam ion flux as a function of axial position

Beam Diameter: D_b	3.3	cm
Grid Open Area Frac.: ϕ_o	0.45	
Beam Divergence Half-Angle: α	7	deg
Beam Voltage: V_b	500	V
Beam Current: J_{bo}	0.0209	A
Mass Flowrate: $\dot{m}$	0.35	mg/sec
Test Chamb. Press: P_a	2.1 x 10^{-4}	Torr
Test Chamb. Gas Temp: T_a	400	K
Disch. Chamb. Gas Temp: T_d	500	K
Non-Dim.Target Position: $\tilde{Z}_t$	4.066	

Table 2.2: Test parameters for the 500 eV case used in numerical calculation of fluxes to estimate contribution of charge-exchange ions to total measured current: Gas temperatures were estimates. Sensitivity of solution to these estimates was factored into uncertainty as discussed in text.

Figure 2.4 shows the charge exchange and beam ion fluxes as a function of the nondimensionalized axial coordinate. This plot corresponds to the solution of Equation 2.19 - 2.22 for the 500 eV case. The specific test conditions for this solution are listed in Table 2.2. The values of β calculated for the four cases considered ranged from 1.6 - 2.0.

Doubly Ionized Incident Atoms

Because the probe will count the arrival of a double ion as two single ions, it is necessary to calculate the equivalent single ion dosage at the target. Knowing the double to single ion ratio enables one to correct for double ion dosage in terms of the *number* of incident ions, it is much more difficult to correct for *damage* caused by the double ions which impact with twice the energy. In the present investigation, the discharge voltage was 35 - 36 V, and the gas utilization efficiency ranged from 2.1 - 8.5 percent. For these conditions, the neutral density is expected to be too high to support any significant number of doubly ionized atoms and the fraction of double ions can be assumed negligible. The yield is then given by the ratio of atoms removed to incident energetic particles:

$$Y = \frac{N_A}{N_E} \tag{2.25}$$

which can be expressed in terms of the previous expressions as

$$Y = \frac{h_{V/A}\rho e N_{avo} A_p}{M\beta \int_0^\tau J_p(t)dt} \tag{2.26}$$

Beam Nonuniformity

In these experiments the probe and target was located only 6.7 cm (2.64 in) from the source. With the target and source in such proximity, a potentially significant uncertainty in the measured current is introduced by nonuniformity of the beam profile. During the experiment, the probe was centered on the point of maximum current in the beam. This was checked at various times during the experiment by moving the probe slightly and observing the probe current. The eroded portions of the samples are located within a 1.27 cm (0.5 inch) diameter circle centered on the probe. Non-uniformity of the beam resulted in the current density decreasing away from the probe. Over time, the non-uniformity worsened as a result of localized erosion of the ion source accelerator grid. The resulting perturbation in the beam symmetry was noticeable in a subsequent mapping of the current profile as shown in Figure 2.5. To correct the dose calculation for beam non uniformity, the density profile maps were used to estimate the incident current at the location of the exposed sample as a fraction of the maximum beam current.

2.4 Results

The yield measured for molybdenum is presented in Figure 2.6 along with data from Rosenberg and Wehner [11] and Weijsenfeld et al. [12]. Both of these previous studies used biased targets placed in plasma sources to provide the incident ions and utilized measurement of target mass loss to determine the quantity of sputtered material. Another difference between these earlier studies and the present one is the fact the incidence angle in the present work varied between 9 - 15 degrees as shown in Table 2.1. Despite this difference, the agreement is seen to be good.

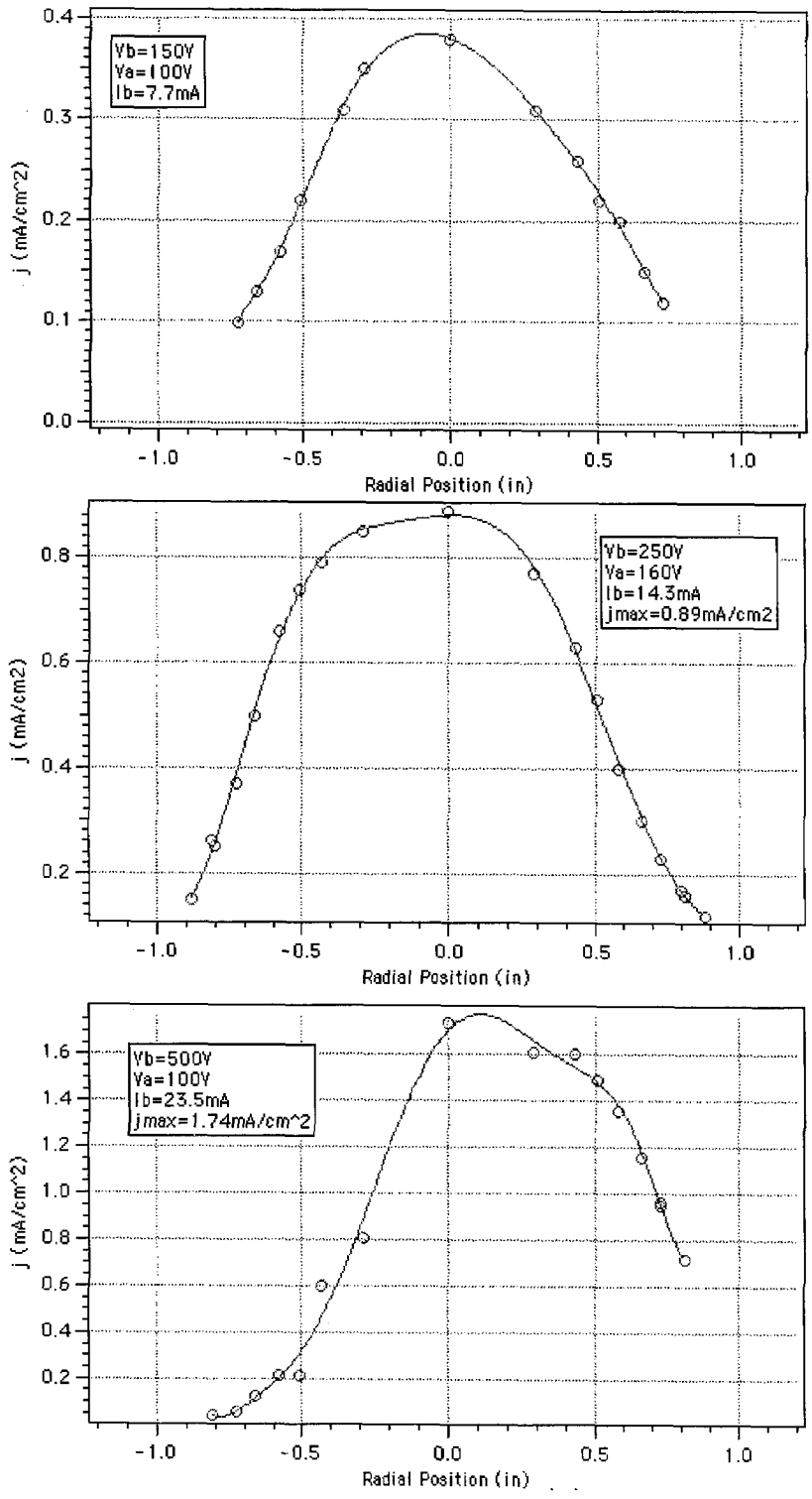

Figure 2.5: Measured current density profiles for beam energies of 150 V (top), 250 V (center) and 500 V (bottom): 750 V case was not mapped due to deterioration of grid.

The absolute yield data for the diamond and carbon-carbon are presented in Figures 2.7 - 2.9. The carbon-carbon yield shown in Figure 2.7 increases monotonically with energy, as expected from previous investigations with graphite [11]. Unlike graphite, the carbon-carbon composite consists of graphitic fibers woven together in a carbonaceous matrix, which is in part graphitic and part glassy carbon [38]. Although these targets were polished before testing, examination of the profilometer traces reveal an increase in surface roughness for the carbon-carbon after exposure to the beam, probably resulting from local variation in yield between the fibers and the matrix. The monotonic increase in yield with increasing energy is similar to that reported previously for graphite.

The sputter yield of the polycrystalline diamond is shown in Figure 2.8. To within experimental uncertainty, the sputter yield appears to increase monotonically with energy. The measured decrease at 250 eV is within the experimental uncertainty due to ion flux nonuniformity and slight variation in incidence angle.

The sputter yields for the single crystal diamond are shown in Figure 2.9. Single crystal yields are known to be dependent on both the crystallographic plane and its orientation relative to the incident beam [39] with the incidence angle of the bombarding ions having a much more pronounced effect on the yield of single crystal materials as compared to polycrystalline ones. This is due in part to channeling effects in which incident ions can penetrate more deeply into the target when the beam is aligned with specific lattice directions. Energy deposition at these deeper layers usually result in lower sputter removal of material and appear as a series of dips superimposed on the characteristic $\cos^{-1}$ yield versus incidence angle curve. Whetten et al. measured sputter yields of (100) single crystal diamond subject to argon ion bombardment at 500 eV as a function of incidence angle [23]. The measured values

ranged from approximately 0.14 at normal incidence to 0.28 at an angle of 25 degrees. The value measured here for xenon at the same energy was nominally 0.07 at an incidence angle of approximately 15 degrees. The SEM photos in Figure 2.11 show the after-exposure topography of the CVD and single crystal diamond samples at energies of 500 and 750 eV. At 500 eV, the characteristic pit diameter is roughly 3 - 4 microns for the CVD diamond (Figure 2.11(a)) and 0.2 microns for the single crystal diamond (Figure 2.11(b)). The pits in the CVD diamond sample at 500 eV also appear slightly elongated as one might expect from non-normal ion incidence. At 750 eV, the CVD sample (Figure 2.11(c)) showed approximately the same pit diameter and distribution as the 500 eV case whereas the single crystal sample (Figure 2.11(d)) showed no evidence of pitting. This sample showed evidence of bombardment induced damage or preferential etching as evident in the raised mesa-like features. These structures were very limited and most of the surface was featureless. Other groups have reported and proposed explanations for damage induced structural transformation of (110) single crystal diamond surfaces subject to argon ion irradiation at 1 keV [28], and polycrystalline diamond subject to neon ion irradiation at 0.1 - 1.6 keV [29]. It is possible that the xenon irradiation at 0.75 keV produced the structures observed in Figure 2.11(d) through some structural transformation similar to that previously reported by these groups but this phenomenon was not investigated further.

For engineering calculations, the erosion rate is often a more meaningful way to present comparisons of sputtering data since one does not have to correct for differing material densities to assess relative performance. The erosion rate is related to the sputter yield by the following relation:

$$\dot{R} = \frac{h_{V/A}}{\tau} = \left(\frac{M}{e\rho N_{avo}}\right) Y\bar{j} \tag{2.27}$$

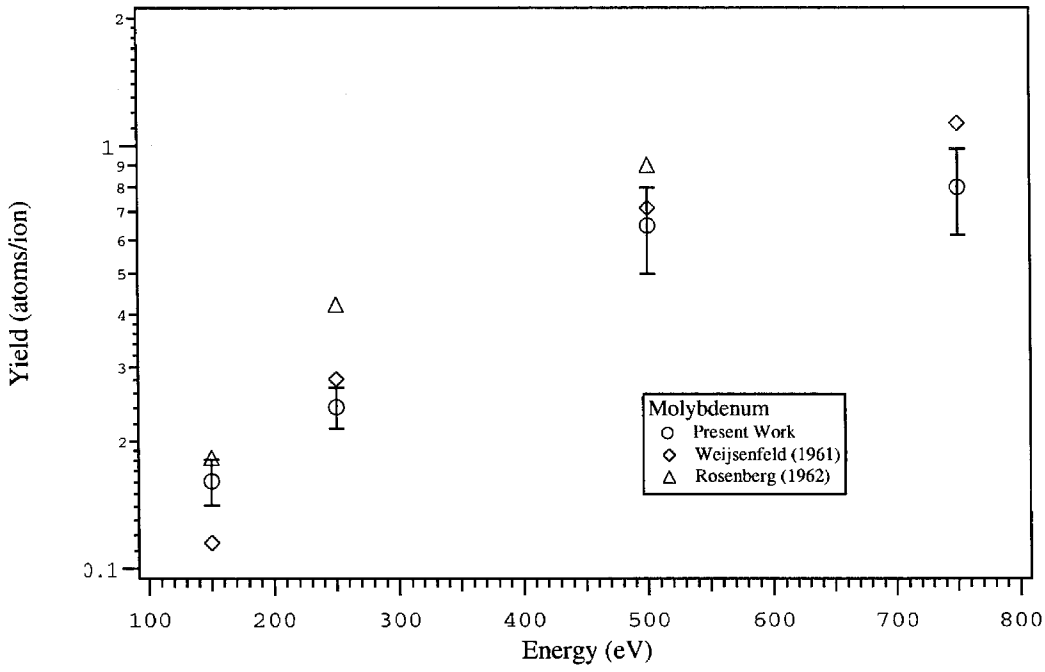

Figure 2.6: Comparison of molybdenum yield with data of Weijsenfeld and Rosenberg

where $\bar{j}$ is the mean current density (including energetic neutrals) averaged over the duration of the exposure. This can be determined from the previous expression (Equation 2.9) for the dosage of energetic particles by

$$\bar{j} = \frac{e}{\tau} N_E = \frac{\beta}{\tau A_p} \int_0^\tau J_p(t) dt \tag{2.28}$$

The erosion rate results for the three materials are presented in Figure 2.10 with values normalized to a current density of 1 mA/cm^2. Although carbon-carbon and diamond have the same molecular weight, the density of diamond is higher. As evident from Equation 2.26, the yield is proportional to the product of the eroded depth and the density. For this reason while the yield of diamond is higher than carbon-carbon, its erosion rate is lower because of its higher density.

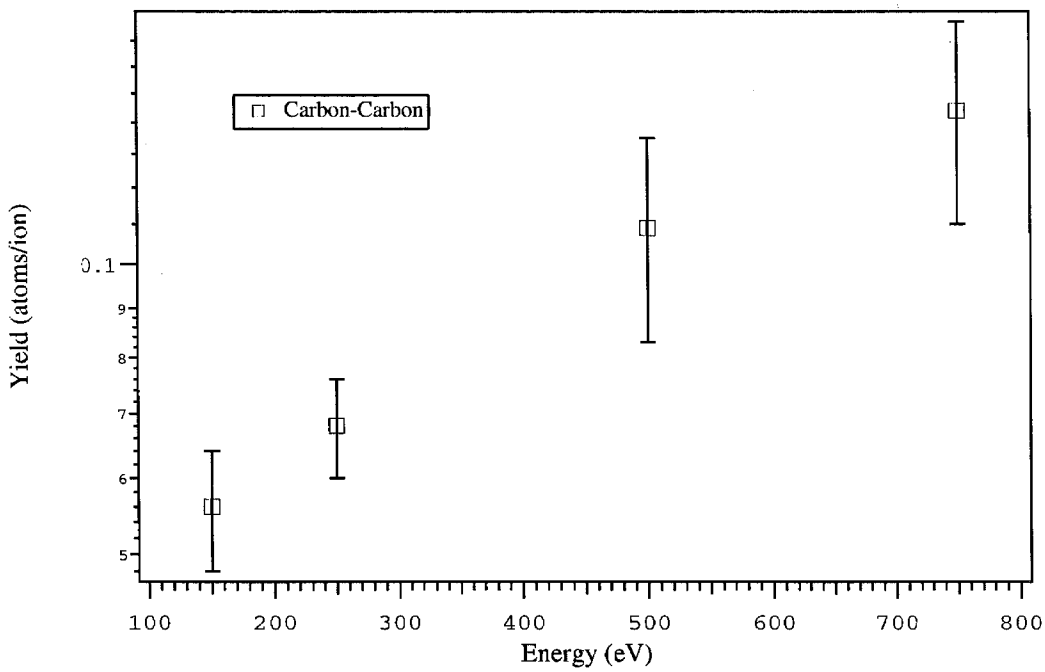

Figure 2.7: Sputter yields for carbon-carbon composite

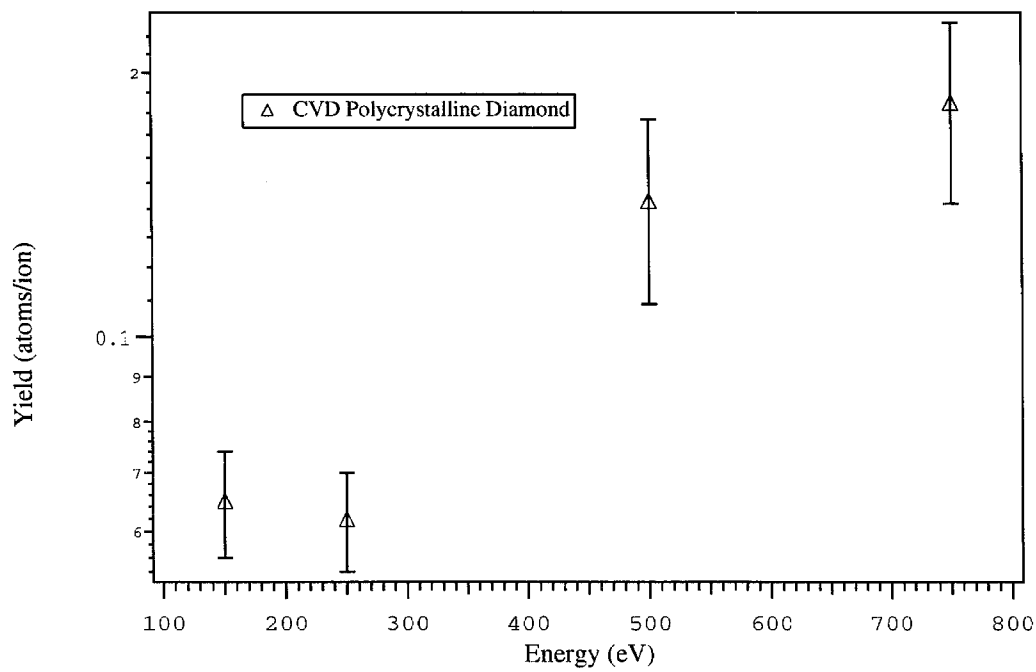

Figure 2.8: Sputter yields for polycrystalline CVD diamond

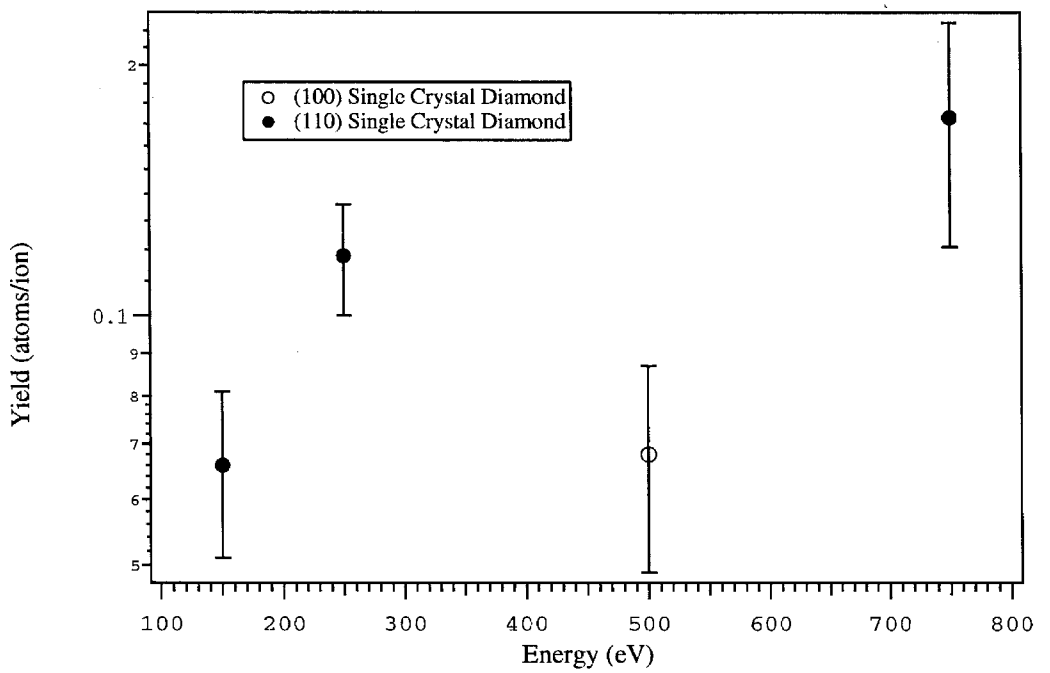

Figure 2.9: Sputter yields for single crystal diamond

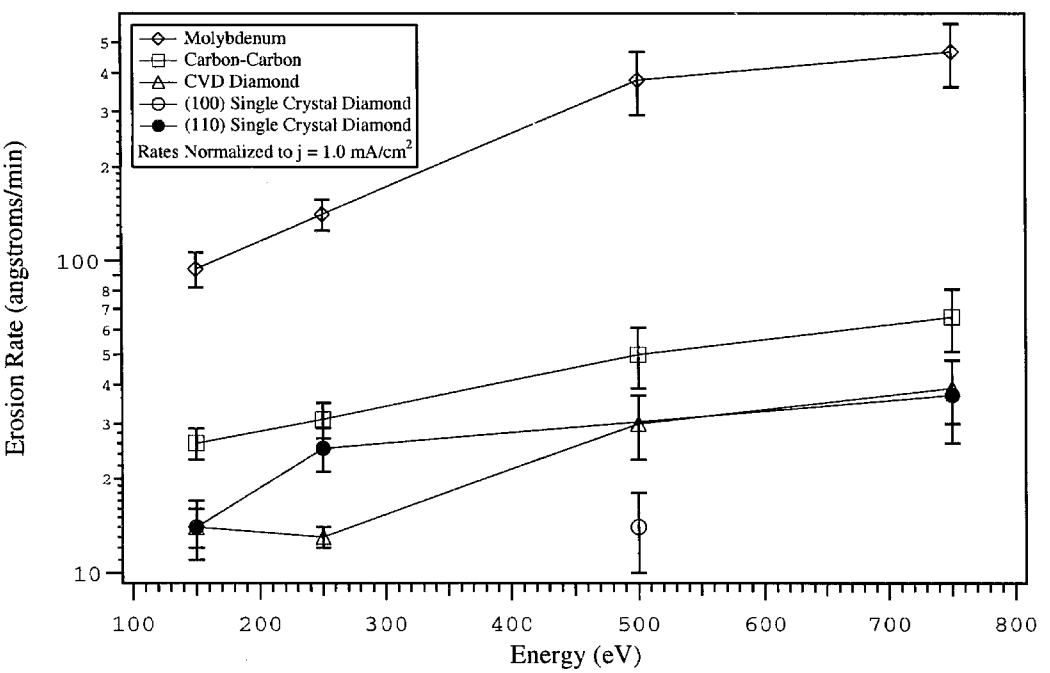

Figure 2.10: Erosion rates normalized to incident current density of 1 mA/cm^2

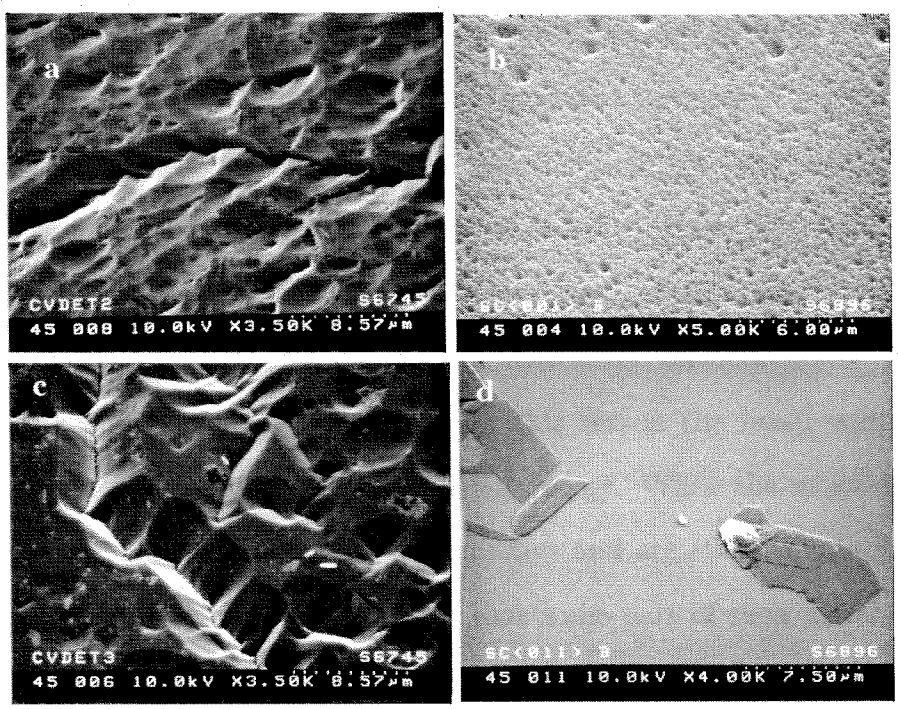

Figure 2.11: Post-exposure SEM images of diamond samples: (a) CVD diamond at 3500X, incident ion energy 500 eV, (b) single crystal (100) diamond at 5000X, incident ion energy 500 eV, (c) CVD diamond at 3500X, incident ion energy 750 eV, (d) single crystal (110) diamond at 4000X, incident ion energy 750 eV

The uncertainty estimate presented along with the data in this section include a number of contributions. The two largest contributions to the uncertainty in the data come from 1) the uncertainty in the calculation of the factor β given by Equations 2.8 and 2.5) the uncertainty introduced by the location of the sample in the non-uniform beam which has roughly a gaussian profile over the target. These two factors account for approximately ninety-five percent of the total uncertainty in the yield data. To the extent the plume model is valid, the uncertainty in the β factor is a result of uncertainties in some of the variables used in the solution of the differential equations 2.19 - 2.22. In particular, the actual values for the gas temperature in the plume (T_a), discharge chamber (T_d), and boundary condition (Equation 2.22) were unknown.

Bounding ranges for each of these were used to calculate uncertainty bounds in the calculation of β. This uncertainty was then propagated throughout the data analysis along with other contributions such as that associated with eroded depth and target density to determine the overall uncertainty shown in Figures 2.6 - 2.10. The ions produced by the Kaufman source have a narrow energy distribution and are assumed to be monoenergetic. Both the beam and neutralizer filament power supply are grounded to a common facility ground. For this reason the beam voltage should provide a very good estimate of the beam ion energy. While the molybdenum and carbon-carbon samples are electrically conductive and are effectively grounded, the diamond samples are good insulators such that some part of their surface area will likely be at the floating potential when exposed to the plasma beam. However, with the exception of the small unmasked area, all the samples are in secure contact with a conducting and grounded mounting fixture. Therefore localized charging of the insulating samples is not expected to be significant. The horizontal error bar on the energy in Figures 2.6 - 2.10 can be estimated from the specifications of the beam power supply. The power supply used has an accuracy of approximately 2 percent which translates into a spread of $\pm$ 3 V at an energy of 150 eV and $\pm$ 15 V at an energy of 750 eV.

2.5 Conclusions

Sputter yields were measured for molybdenum, carbon-carbon, single crystal, and polycrystalline diamond subject to xenon ion bombardment in the energy range of 150 to 750 eV. An estimate was made of charge-exchange ion production in the plume and used to correct the recorded ion dosages on the target in order to determine sputter

yields and erosion rates. The results indicate that CVD diamond film should provide a factor of 7 - 12 improvement in erosion rate over molybdenum and at least a factor of 1.5 over carbon-carbon. Finally, qualitative examination of the post-exposure surface topography for the CVD and single crystal diamond revealed significant differences in both the size and distribution of impact related pits.

Chapter 3

Direct Current Arc Sources for Diamond CVD

3.1 Arcjet Assisted Diamond CVD

3.1.1 Description of the DC Arcjet

The direct current arc plasma source refers to a class of devices in which a constricted arc is used to heat a gas which can then be expanded through a nozzle to form a high velocity jet. Such devices have been used for several decades both as industrial cutting tools (plasma heaters and torches) as well as thrusters for spacecraft propulsion (arcjets). For a space thruster, the need to make this acceleration process as efficient as possible and the thruster as lightweight and compact as possible has resulted in a large number of investigations since the 1960s into the basic physical processes at work.

A diagram of an arcjet is shown in Figure 3.1. A cylindrical cathode is located within a plenum formed in a concentric anode. Both of these electrodes are usually

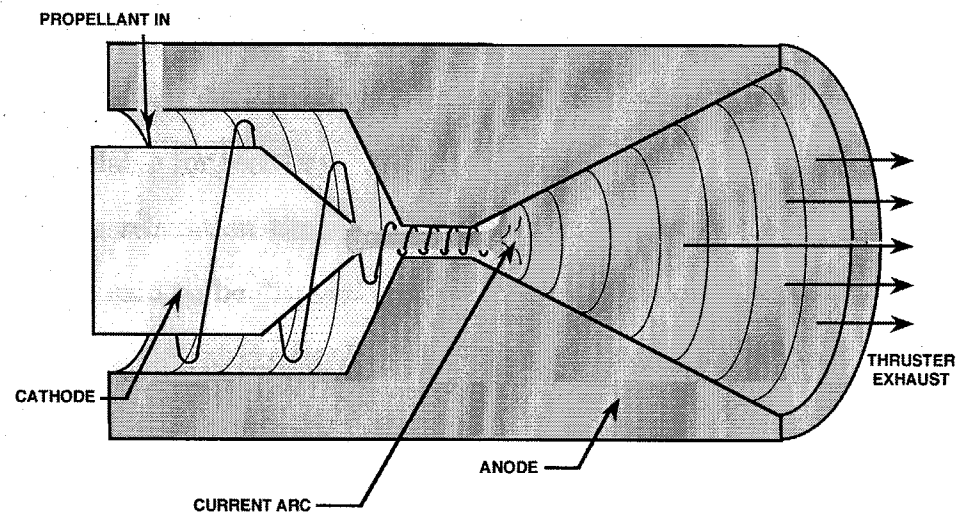

Figure 3.1: Direct Current arc plasma source

made from tungsten or graphite. A collimated arc is established between the cathode and the anode which will extend through the throat and attach to the anode just downstream of the throat in a diffuse column. Gas is injected into the volume between the electrodes with a tangential velocity component to induce a swirl which helps stabilize the arc as well as improve heat transfer efficiency. Arcjets have been built and tested at power levels ranging from a few kilowatts to several tens of kilowatts. Typical operating conditions for a 30 kW arcjet operating on hydrogen include a current of roughly 150 A, terminal voltage of 200 V, flowrate of 0.1 g/sec and a chamber pressure of 1 atm with a resulting exhaust velocity of 15 km/sec [40].

Two of the biggest differences between the plasma torch and an arcjet is the choice of gas used and the importance of the nozzle design. For an arcjet it is essential to recover as much of the energy tied-up in translational, rotational, and vibrational modes as possible and convert this to directed kinetic energy of the exhaust plume. These higher energy modes will be excited as the gas is heated through a combination of radiative (from both the arc and the chamber walls) and convective mechanisms.

Different propellants are characterized by different time constants for relaxation of these modes into a state of equilibrium with translational modes from which this energy is available for recovery as directed kinetic energy as the flow expands in the nozzle. If the relaxation time is larger than the residence time in the nozzle then this energy is said to be "frozen" into the flow and cannot be recovered. Numerous gases have been evaluated over the years including hydrogen, ammonia, and hydrazine vapor.

3.1.2 Application to Diamond Film Synthesis

In 1988, Kurihara et al. [41] reported what they referred to as the "first successful synthesis and characterization of diamonds by the use of a DC plasma jet..." Prior to this, the DC plasma jet had been used for non-diamond applications such as nitriding, carburizing, and carbon nitriding of metals [42]. Given the growing interest in low pressure diamond CVD techniques in the late 1980's, the use of the DC plasma jet source for diamond was a natural extension of this effort. Most of the investigations to date have used commercially available plasma torches and heaters (Miller SG100, Thermal Dynamics F-5000 for example) in some cases with modifications to enable post discharge injection of the hydrocarbon gas. In the majority of these studies, the plasma jet is directed downward directly onto a water cooled substrate located 5 - 15 cm from the exit plane. Commercial plasma torches typically have an exit orifice diameter of less than 0.5 cm (designed for jet expansion to atmospheric pressure) which limits the area on the substrate which can be covered without the use of some form of substrate movement through the beam during deposition.

Loh and Cappelli at Stanford University were the first to investigate the supersonic expansion of the plasma jet into pressures less than 1 Torr first by adapting commer-

cial torches with appropriately designed nozzles [43] and later by using arcjets as described in the previous section specifically designed as thrusters for spacecraft [44]. In addition to enabling much higher exhaust velocities, the nozzles also resulted in larger exit plane cross sections with a diameter of 1 - 2 cm. Even larger plume cross sections are possible when expanding into lower pressures.

Several groups have focused their efforts at scaling up the substrate deposition area and/or power. Matsumoto et al. [45] mounted a substrate on X-Y translation stage which scanned the sample under the jet at rates up to 50 mm/sec during growth. While the uniformity of film thickness improved, the overall growth rate and quality tended to decrease with scanning speed. Hirata et al. [46,47] developed a one cathode, three anode device in an attempt to increase jet cross-sectional area. Another example of a design driven by a desire to scale up the deposition area and power is that of Lu et al. [48]. In this approach, the arc is designed to extend from the cathode through a long "discharge tunnel" roughly 0.5 m in length before attaching to the anode. Over this length the plasma jet diameter increases to roughly 10 cm. In addition, the length of the arc results in arc operation in a higher voltage, lower current mode (for a given jet cross-sectional area) than would be possible with a conventional torch. This has advantages when scaling to higher power levels ($>$ 100 kW) where high currents can result in significant electrode erosion and sample contamination. The methane precursor gas is injected just upstream of the anode current attachment area, requiring the methane to pass through the arc. Such a long arc requires an external magnet to stabilize and constrain the discharge. In addition, the magnetic design allows the arc attachment point to be rotated in order to better distribute heat loads to the anode and enhance mixing of the methane as it passes through.

It is also worth mentioning some other more significant departures from commer-

cially available devices which have been employed. Akatsuka [49] et al. who were among the first to investigate the thermal plasma jet technique, used a directed gas stream which was injected transverse to an arc and did not incorporate any gas acceleration such as a nozzle at all. Ohtake et al. [50] used a custom designed arcjet in which a single anode is located downstream and radially offset from the cathode. This asymmetrical arrangement requires the arc to bend through ninety degrees before attaching.

In work by Snail [51] et al., three identical plasma torches were arranged above the substrate in such a way that the plasma streams coalesce into a larger stream. In this way, the authors hoped to improve entrainment of the hydrocarbon precursor and establish a more uniform reactive gas mixture. A complete departure from the directed jet approach is that of Karner [52] et al., in which a rack of substrates was mounted surrounding a DC arc. This approach lacked the directed jet characteristic of the vast majority of DC arc thermal plasma sources and instead relied on diffusion of activated species radially toward the substrates. This approach had the advantage of enabling the batch processing of a large number of substrates.

In the majority of investigations, methane has been used as the carbon precursor gas with the discharge usually operating on some mixture of hydrogen and argon. As mentioned earlier, hydrogen is believed to be a critical component to growth of the film. Argon facilitates ignition and stable operation of the discharge. While argon is inert, it will participate in the chemistry through reactions facilitated by third body interactions. Methane concentrations of up to several tens of percent of the hydrogen flow (by volume) have been used although concentrations greater than 1-2 percent tend to produce a substantial amount of graphitic or amorphous carbon.

Although methane has been used in most work to date, there have been sev-

eral studies designed to assess the relative benefit using alternative hydrocarbons in hopes of increasing concentrations of radicals beneficial to growth. These efforts include those of Itoh [53] and Horii et al. [54] with chlorobenzene, Kotaki [55] with dichlorobenzene and Kotaki [56] and Itoh [53] with carbon tetrachloride. Alcohols have also been investigated by Akatsuka et al. [49] who used ethanol and Han et al. [57] who used methanol. Ohtake et al. [58] experimented with oxygen addition in the hydrogen-argon-methane plasma where the oxygen containing plasma was found to preferentially etch graphite over diamond by a factor of 57. Surface roughness and porosity were found to decrease with increased oxygen concentration at the price of reduced nucleation density and growth rate.

From the standpoint of achieving a high level of mixture uniformity, it may appear at first to be desirable to premix the hydrocarbon with the argon-hydrogen gas supply to the discharge as was done in some of the early investigations [41, 59, 60]. For the most part, however, this approach is avoided because the hydrocarbon pyrolysis in the very high temperature environment of the arc can lead to an increase in the cathode erosion rate [61] by a factor of up to 750 as well as soot formation, which can clog the throat and inhibit stable arc operation [50]. For this reason, most investigators choose to inject the hydrocarbon through some injection point located near the exit plane but downstream from the arc attachment point [43, 44, 48, 62-66]. Another approach is to supply the hydrocarbon through a remote (possibly water cooled) injector tube located near the substrate [50, 51, 58, 67]. Because it can easily be moved, use of a remote injector also facilitates the investigation of the effect of hydrocarbon residence time (and hence degree of pyrolysis) in the plasma.

The problems encountered when a hydrocarbon is used directly in the arc could be particularly problematic for commercial reactor designs where efficient use of the

precursor gas stock (as measured by the carbon utilization efficiency) needs to be as high as possible. In such a reactor, some form of gas recycling is likely if operational costs are to be kept down. In gas recycling schemes, the argon-hydrogen-hydrocarbon mixture pumped from the process chamber is fed back through the discharge (with some possible scrubbing for pump oil). Martorell et al. [61] have demonstrated an effective strategy to protect the cathode from the hydrocarbon in the recycled gas supply. In their scheme, the gas injection to the discharge is accomplished through two concentric, annular passages surrounding the cathode. The flow though the inner feed adjacent to the cathode is makeup hydrogen-argon flow with no hydrocarbon component. The flow through the outer annulus consists of the recycled hydrogen-argon-methane flow. The cathode erosion rates with this "gas shield" were measured (at a power level of 72 kW) to be 9 mg/hr, compared to 1500 mg/hr with methane flow and no shield flow. For comparison, the erosion rate with no methane at all was less than 2 mg/hr.

In the roughly twelve years since diamond deposition using DC arcjets was first reported, deposition over a wide range of power levels from several hundred watts to one hundred kilowatts has been attempted. Most of this work falls into three distinct ranges of power. Many of the commercial cutting torches as well as the arcjets designed for spacecraft propulsion fall in the range of 0 - 3 kW [41–44, 49, 59, 60, 67]. A second group is clustered in the range of roughly 5 - 12 kW, which also includes many commercial devices [45, 50, 51, 58, 62, 63, 65, 66]. For power levels above 25 kW, Baldwin et al. [64] use a modified Thermal Dynamics F-5000 at 27 kW but cite it as designed for operation at powers up to 150 kW. Martorell et al. [61] used a laboratory design at 72 kW and Lu et al. [48] also used a laboratory device described earlier with external magnetic field arc stabilization at a power level of 100 kW to deposit on areas

roughly 10 cm in diameter. In general the growth rate, which is often used as a figure of merit in assessments of different deposition techniques, depends on a number of variables such as substrate material, substrate temperature, jet velocity, biasing of the substrate, gas composition, and power per unit deposition area. The highest growth rate reported was that of Ohtake [50] at 930 μm/hr at a power level of 9.45 kW (growth area not reported) whereas Lu [48] reports 40 μm/hr at a power level of 100 kW (over an 11 cm diameter area).

The plasma jets described are all characterized by a high enthalpy and in some cases, very high velocity jet ($\geq$ 10 km/sec for the supersonic jets). Under these conditions the substrates will be subject to extreme thermal loads and even refractory metals will require water cooled mounts. By far, molybdenum has been the most commonly used substrate in DC plasma jet investigations. A few groups have used silicon wafers [41,43,59–61] although these are very prone to damage from overheating. Snail [51] et al. have succeeded in the homoepitaxial deposition on natural type IIa diamond. At least four additional surveys [41,42,59,63] have been conducted on other substrates including W, Pt, SiC, Al_2O_3, Fe, Nb, Ti, Co, Cu, and Ni.

One distinguishing feature (and advantage) of diamond growth in chemical vapor deposition process is the low pressures involved. While some of the DC plasma jet assisted growth studies were done at atmospheric pressure [64] (which is still orders of magnitude lower than non-CVD, high pressure diamond synthesis), most of the work [41,42,45,49–51,58,60,62,65] has been done at pressures of 100 - 400 Torr (13.3 - 53.2 kPa). Most of the remaining studies fall into a second group [61,63,66,67] at still lower pressures in the range of 5 - 100 Torr (0.67 - 13.3 kPa). Loh and Cappelli [43,44] exploited the supersonic jet expansion to an even lower pressure range of 0.08 - 1 Torr (11 - 133 Pa) to obtain the highest jet velocities reported (10 km/sec).

Finally it is important to discuss briefly efforts at enhancement of nucleation and film growth through the use of substrate biasing. Matsumoto [62] reports biasing a substrate (positive with respect to the cathode) to potentials up to 500 V. At a substrate collected current of 2 A, the growth rate doubled but uniformity was not improved. At 3 A the substrate temperature increased to the point where mostly graphite was deposited. In an effort to decouple the effects of substrate biasing from substrate (ohmic) heating, a second approach was attempted in which a water cooled copper ring located above the substrate was biased to 280 - 300 V while the substrate itself was allowed to float electrically. This resulted in a 2 - 3 A current draw through the ring and increase in the growth rate by a factor of 2.5. In addition, this second approach resulted in only a 10 C rise in temperature of the substrate compared with 100 C for the direct biasing of the substrate. Because the currents are reported rather than current densities (unspecified collection area) in this reference, it is difficult to compare these results with other studies.

The most significant enhancement reported as a result of substrate biasing is that of Baldwin [64] in which the substrate was directly biased up to 170 V corresponding to a current collection of 4.9 A/cm^2. At this current density the growth rate increased over the unbiased case by almost a factor of 7 (from 6 to 40 μm/hr). Perhaps the most interesting feature of these results was the insensitivity of growth rate to current density until a threshold of roughly 2.4 A/cm^2 was reached beyond which the growth rate increased.

It has been suggested [64] that the strong electric field produced by the biasing of the substrate (100 - 200 V over a few mm) accelerates the highly mobile free electrons in the boundary layer. The electron temperature eventually reaches some threshold value where electron-catalyzed reactions dominate the production of atomic hydrogen

or hydrocarbon radicals determining the growth rate. Baldwin and co-workers [64] have used a two-dimensional imaging technique in which the H_α and H_β line emission over the substrate is imaged for different substrate biasing conditions. These images indicate that the biasing has a significant effect on gas-phase composition in the boundary layer.

3.2 MPD Accelerator Assisted Diamond CVD

3.2.1 Description of the MPD Accelerator

The magnetoplasmadynamic (MPD) accelerator represents a different class of accelerator in which electromagnetic forces are predominantly used to accelerate the gas. Further distinctions are made as to whether the magnetic field is primarily due to an externally applied field or self-induced by the discharge current itself. Figure 3.2 is a schematic of a self-field MPD thruster. Investigation of the MPD thruster for application to space propulsion began in the mid 1960s with some early experiments using arcjets. It was found that as the propellant flowrate into the arcjet was reduced, a regime was encountered in which the thrust and exhaust velocity increased rapidly with current with a somewhat weaker dependence on flowrate [68]. In Figure 3.2 the gas is injected through an insulating backplate to which a coaxial pair of electrodes are mounted. A current which can range from several hundred to over ten thousand amperes is established between the electrodes. The central cathode is typically made of tungsten and operates at a temperatures of approximately 3000 C. Thermionic emission of electrons into the relatively low pressure annulus sustains the diffuse discharge. The qualitative dependence of thrust on current can in large part be explained through a simplified physical model in which the Lorentz body force is

integrated over the volume where acceleration takes place [40]. In this model, the axial components of the current lines produce an azimuthal magnetic field which in turn interacts with the radial and axial components of the current to produce electromagnetic body forces. Two components, referred to as the "blowing" and "pumping" components, are shown in Figure 3.2. The blowing contribution accounts for most of the thrust whereas the pumping component establishes a radial pressure distribution within the volume but does not contribute to thrust except at the cathode tip.

As the discharge current is increased for a given mass flowrate, it is believed that this pumping force leads to depletion of current carriers at the anode. Under these conditions, the discharge becomes unstable with a uniform current attachment transitioning to a spot attachment mode with very high localized current densities on both the anode and cathode. In addition to the spot attachment of the current, this transition is characterized by significantly increased cathode erosion rates, ablation of insulating surfaces and asymmetrical discharge with rapid voltage fluctuations with frequencies of hundreds of kilohertz and several megahertz [69]. For a given electrode geometry and propellant, this transition, referred to as "onset," occurs at a critical value of the parameter defined by the ratio of the current squared to the mass flowrate $J^2/\dot{m}$. Yoshikawa et al. [70] have observed this transition in hydrogen at a value of $J^2/\dot{m}$ of 185 kA^2 sec/g which they compare to a theoretically predicted value of 266 kA^2 sec/g.

Much of the early promise of this device as a thruster for space applications was tempered as it became evident that the device was subject not only to the same frozen flow losses as the arcjet, but the presence of an anode sheath potential fall which, at the high currents under consideration, resulted in significant power deposition to the anode. As the power level is increased to hundreds of kilowatts or higher, the amount

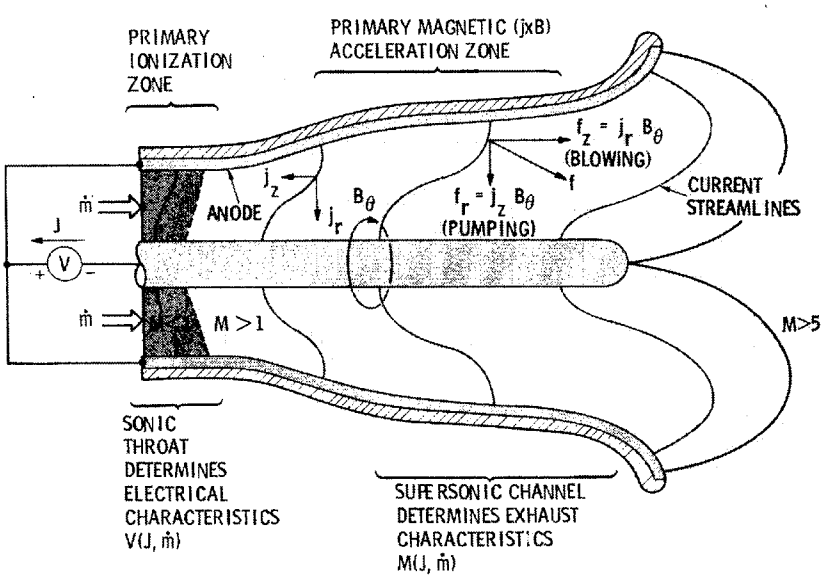

Figure 3.2: Self-Field Magnetoplasmadynamic (MPD) accelerator

of power lost to the anode fall becomes a tolerable fraction of the total power input and the overall device efficiency can exceed fifty percent. For this reason the MPD has emerged as an attractive candidate for high powered missions in which hundreds of kilowatts to megawatts of electrical power need to be processed in a compact device.

For a purely electromagnetic accelerator the thrust produced is found to scale as the square of the current (with blowing force due to the $\vec{j} \times \vec{B}$ body force) and the ratio of the cathode to anode radii. A derivation of the well known Maecker thrust equation can be found in the textbook by Jahn [40] for the case of a purely coaxial, self-field, electromagnetic thruster:

$$T = \frac{\mu_0}{4\pi}\left(\ln\frac{r_a}{r_c} + \frac{3}{4}\right)J^2 \tag{3.1}$$

In this equation, the thrust is seen to scale with the logarithm of the ratio of the anode to cathode radii. A more accurate, semi-empirical scaling relation has been

developed by Choueiri which captures the thrust dependence on mass flowrate as well as current [71]. The mean gas jet velocity (related to the specific impulse parameter in rocket performance) will scale as the ratio of the current squared divided by the mass flowrate. The mass flowrate required to produce a desired level of thrust will depend on the particular geometry since the pressure (and hence number density of current carriers) must be sufficient to adequately sustain the needed current. The geometry (cathode and anode length and radii) in turn is in large part determined by the need for the cathode to thermionically emit high current densities while operating below the melting point of tungsten.

The difficulty in testing devices at power levels of megawatts has led to numerous studies using so called "quasi-steady" devices. These are MPD thrusters driven by pulse forming networks capable of delivering tens of thousands of amperes over periods of several milliseconds. This time period is believed to be long compared with the timescales for the relevant plasma and gas kinetic phenomenon but short compared to thermal time constants. While the MPD accelerator has been tested with many propellants including argon, nitrogen, ammonia, and xenon, its use with hydrogen, which has the most relevance to materials processing applications, is considered here. In addition to quasi-steady operation, further attempts to improve efficiency, particularly at power levels below 100 kW, have employed some form of magnetic field augmentation, usually through the use of electromagnets and, less frequently, permanent magnets. In addition to enhancing the $\vec{j} \times \vec{B}$ body force for a given current, the applied magnetic fields help improve the uniformity of the discharge along the anode and extend the operational range of current before the critical onset value is reached. Most of the MPD devices use tungsten cathodes with added thorium (typically 2%). This has the effect of lowering the work function improving thermionic emission and

overall device efficiency. For space application, it is likely any MPD device would be radiation cooled. Most of the devices described below, however, have used water-cooled copper anodes. From a practical standpoint, a water-cooled anode has distinct advantages in the laboratory as the thermal demands of radiation cooled tungsten anodes are significantly relaxed without changing the basic physics being studied.

Through the 1980s, most of the hydrogen MPD work was being done at laboratories in Japan. A number of self-field, quasi-steady devices were tested by Yoshikawa and colleagues at hydrogen flowrates of 0.2 to 1.4 g/sec and instantaneous power levels of 350 kW to 4.2 MW [70, 72, 73]. Yoshikawa used a magnetic field probe to map azimuthal filed strength from which the discharge current contours can be inferred. They observed, as do others, the presence of a luminous jet along the core of the discharge. This cathode jet is believed to be formed by the relatively high density along the central axis produced by the radial pumping force. Toki et al. [74] also operated a purely self-field device in quasi-steady mode at power levels of 800 kW - 2.5 MW and flow rates of 1.8 g/sec. In this work the more commonly used solid rod cathode was compared with a hollow cathode. With suitable choice of hollow cathode orifice diameter and interelectrode spacing, Toki was able to produce comparable performance with the hollow cathode geometry while reducing cathode erosion rates by an order of magnitude.

Tahara and co-workers investigated both self and applied field devices in pulsed mode at flowrates of 0.4 - 2.8 g/sec and power levels of 500 kW - 3.7 MW [75-78]. This work also included an attempt to use current distributions inferred from magnetic field measurements in conjunction with a plasma fluid model to calculate properties within the discharge volume as well as downstream of the exit plane. The calculated properties included gas temperature and pressure, dissociation and ionization fraction

as well as velocity distributions. The validity of these estimates are somewhat limited by assumptions made such as ionization and chemical equilibrium. The conditions within the discharge are likely to be far from equilibrium due to the complex processes associated with heating within the intense arc.

Some work has focused on the use of permanent magnets as a means of improving efficiency without the mass penalty of heavy electromagnets. One such example is the work of Arakawa et al. [79, 80] with steady state operation at low power levels of 6 - 10 kW and mass flowrates of 0.9 mg/sec. In this work an array of 32 samarium-cobalt magnets were mounted along the perimeter of the flared anode. This arrangement enabled thrust efficiencies as high as 25 percent and jet velocities as high as 7.5 km/sec even though the power level was only 10.4 kW.

Researchers at the University of Stuttgart performed extensive investigations of steady state devices using a variety of diagnostics both within the discharge and in the exhaust plume. While most of these studies have been performed with argon, Merke et al. [69] have investigated performance with hydrogen including detailed studies of the frequency content of the voltage oscillations associated with the onset phenomenon. This work was at hydrogen flowrates of 0.15 g/sec at a power level of 17 - 180 kW.

Beginning in the mid 1960s, work in the United States by Patrick with hydrogen [81] evaluated the use of applied magnetic fields at power levels below 100 kW in steady state operation. From the 1970s most of the investigations have been performed at Princeton using argon. Much of the value of this body of work is that most of it was done using the same device geometry. That makes the "Princeton Benchmark Thruster," as it is known, probably the most thoroughly characterized MPD device. Recently, Choueiri and Ziemer [82] have compiled an extensive performance

database for this device operating in a quasi-steady mode at power levels of 1 -12 MW on hydrogen at mass flowrates of 0.5 and 1.0 g/sec. Data was also compiled with deuterium, xenon, and argon.

For a materials processing application, the important features of these devices are primarily the exit plane gas composition and power requirements to achieve a desired gas velocity. Reported mean jet velocities and required power levels are presented for a representative sample of the hydrogen MPD literature in Figure 3.3 and Figure 3.4. These are plotted as a function of the $J^2/\dot{m}$ parameter. For comparison, these plots include a data point for the electrothermal arcjet used by Loh and Cappelli [43] for diamond synthesis. As mentioned previously, for a purely electromagnetic thruster, the velocity scales linearly with the $J^2/\dot{m}$ parameter. Since all actual devices include some electrothermal and some electromagnetic acceleration contributions, there is no precisely defined boundary between these two operational modes. However, the data in Figure 3.4 spans the range from electrothermal to electromagnetic acceleration. The dotted line in Figure 3.4 denotes the theoretical limit for hydrogen in which all the enthalpy at a chamber temperature of 3000 K and pressure of 1 atm is converted to kinetic energy. This is a theoretical limit since equilibrium is assumed (no frozen losses) as well as infinite expansion. Loh reported gas temperatures for the 3 kW arcjet of 5000 K in the core falling to approximately 1000 K at the jet boundaries.

The most interesting feature of Figure 3.3 is the data from Arakawa [80] in which high jet velocity has been achieved at a power level two orders of magnitude below most of the other data. As discussed earlier, Arakawa used permanent magnets to enhance performance at lower power. This suggests the possibility that for materials processing applications, high jet velocity can be achieved at modest power levels by operating at high values of $J^2/\dot{m}$ to insure electromagnetic acceleration with the

	Toki 1985 Ref [74]	Yoshikawa 1982 Ref [70]	Arakawa 1988 Ref [80]	Tahara 1988 Ref [78]	Choueiri 1998 Ref [82]	Loh 1992 Ref [43]
$\dot{m}$ (g/sec)	1.8	1.38	9.0 x 10^{-4}	2.75	1.0	0.03
J_d (kA)	4.2 - 9.3	2.95 - 17.7	0.2 - 0.4	3.0 - 14.9	5.4 - 20.5	15
V_d (V)	195 - 265	119 - 236	30 - 26	169 - 248	218 - 583	200
P_d (kW)	819 - 2465	351 - 4180	6.0 - 10.4	507 - 3695	1177 - 11950	3
U_e (km/sec)	12.6 - 28.5	6.0 - 44.0	48.0 - 75.5	4.7 - 21.0	12.6 - 105	10.0
$J^2/\dot{m}$ (kA^2sec/g)	9.8 - 48	6.3 - 228	44.4 - 178	3.3 - 80.7	29.2 - 420	7.6 x 10^{-3}
$d_{cathode}$ (cm)	0.90	0.95	0.80	0.95	1.9	0.48
d_{anode} (cm)	6.0	3.4	7.0	5.8	10.2	–

Table 3.1: Performance data for direct current arc devices with hydrogen propellant: Electrothermal arcjet used by Loh and Cappelli included for comparison with predominantly electromagnetic MPD devices. All MPD data corresponds to quasi-steady operation with self magnetic field with the exception of Arakawa which incorporated permanent magnet field augmentation with steady state operation.

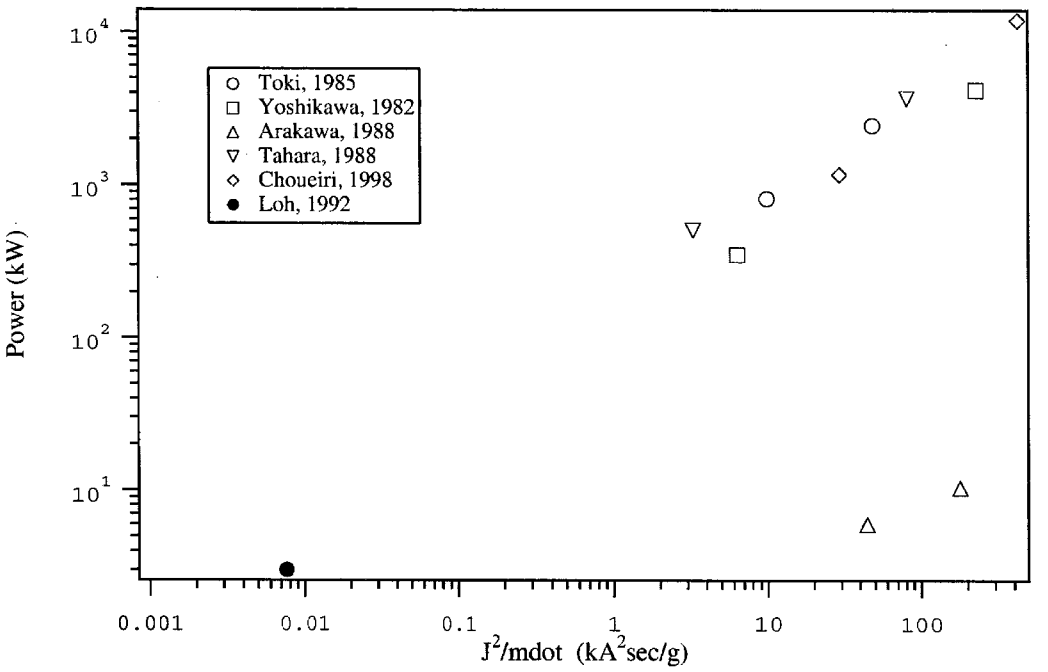

Figure 3.3: Discharge power as a function of $J^2/\dot{m}$ parameter for some previous work with hydrogen

possible use of external magnetic fields to enhance acceleration.

3.2.2 Application to Diamond Film Synthesis

Three characteristics in particular suggest the possibility that one could obtain significant enhancements in growth rate and deposition area of diamond film using an MPD device. These are the inherently higher level of dissociation and ionization of the gas species in the plume core, the higher jet velocity, and the scalability to larger deposition areas. These are discussed in detail below.

Because MPD discharges utilize electromagnetic forces to achieve plasma acceleration, they are not limited by thermal constraints at a physical nozzle throat. For this reason they are capable of operation at significantly higher power densities than

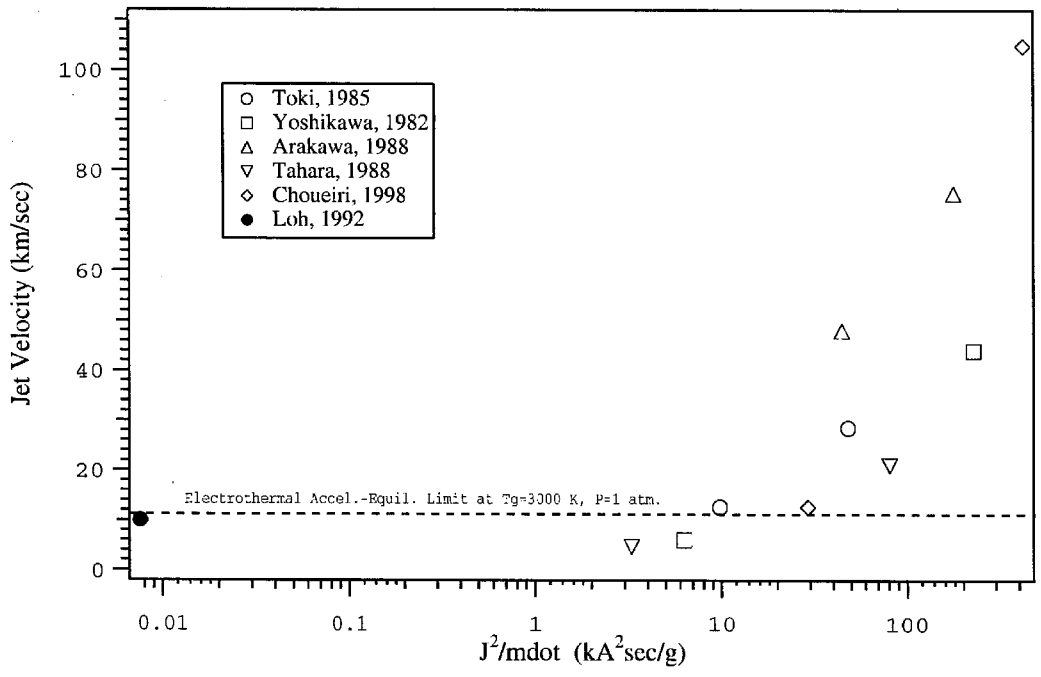

Figure 3.4: Mean gas jet velocity as a function of $J^2/\dot{m}$ parameter for some previous work with hydrogen

arcjets. One consequence of operating at a higher power is the production of a high enthalpy plume with significant dissociation and ionization. Higher levels of dissociation will increase the number densities of species required for growth of diamond and suppression of graphite. While dissociation of the hydrocarbon precursor gas and the hydrogen diluent gas is essential, it is not clear whether the higher ionization level will affect growth.

In an electromagnetic thruster, the thrust level scales approximately with the square of the current which is 1 - 2 orders of magnitude higher than the arcjet. As a result the mean gas velocities in the plume are expected to be higher than the arcjet. The consequence of higher jet velocity will be a higher stagnation temperature, higher Mach number, and correspondingly thinner stagnation boundary layer at the

substrate surface. It is anticipated this will result in sharper concentration gradients over the growth region and a higher flux of activated radicals to the surface.

Because the MPD is an electromagnetic device, it is more easily scaled up to higher power and/or larger electrodes to achieve deposition over a larger region of the substrate than a thermal arcjet. As evident from Equation 3.1, electrode geometry can be scaled to maintain a manageable cathode current density while increasing the overall power and exhaust plume cross-sectional area. Such scale-up could have significant commercial potential if the overall chemistry of the MPD plume is found to be effective for achieving growth.

In 1994, Tanabe et al. [83] published results on their use of an MPD for the deposition of what they refer to as "hybrid" amorphous carbons. These are amorphous carbons with mixed sp^2 and sp^3 bonding. These films were grown with a pulsed MPD device producing a 3 - 8 kA current pulse for approximately 1 ms (pulsed every 10 s). The authors estimate a 50 percent degree of ionization 10 cm downstream of the exit plane at a chamber pressure of 2.2 x 10^{-4} Torr. Substrate temperatures for these films varied between 25 - 600 C. Gases used for these tests included hydrogen and methane as well as oxygen and carbon tetrafluoride injected directly into the discharge. The authors state that "..no studies on synthesizing films using the MPD arc-jet have ever been reported, probably because it was developed as a thruster and not a film generator."

In 1991, Norton Co. reported [84] that it had acquired the rights to a magneto-plasmadynamic arc (MPDARC) source for use in diamond film production. To the best of the author's knowledge, however, neither Norton nor any other group has published results of application of an MPD source to diamond film synthesis.

Chapter 4

MPD Assisted Diamond CVD

4.1 Description of the JPL Cathode Test Facility

This chapter presents results from a series of experiments in which an MPD plasma source was used for diamond film deposition. The facility used for this work was originally set up at JPL for the purpose of investigating lifetime and thermal behavior of high current, thermionic cathodes such as those used in MPD (or Lorentz Force Accelerator) thrusters for space propulsion. A photo and diagram of the vacuum chamber which makes up this facility is shown in Figure 4.1.

The chamber is approximately 0.5 m in diameter and 2.4 m long. As shown in the diagram, it consists of three cylindrical segments which are bolted together with O-ring seals. A number of ports on these segments facilitate electrical and water feed, optical access to the area where the substrate is located, as well as access to the cathode. The chamber is pumped by a 610 l/s Roots Blower backed by a 140 l/s mechanical pump. This pumping combination was originally selected for this facility to enable sustained pumping of relatively high flowrates used in the cathode tests (>

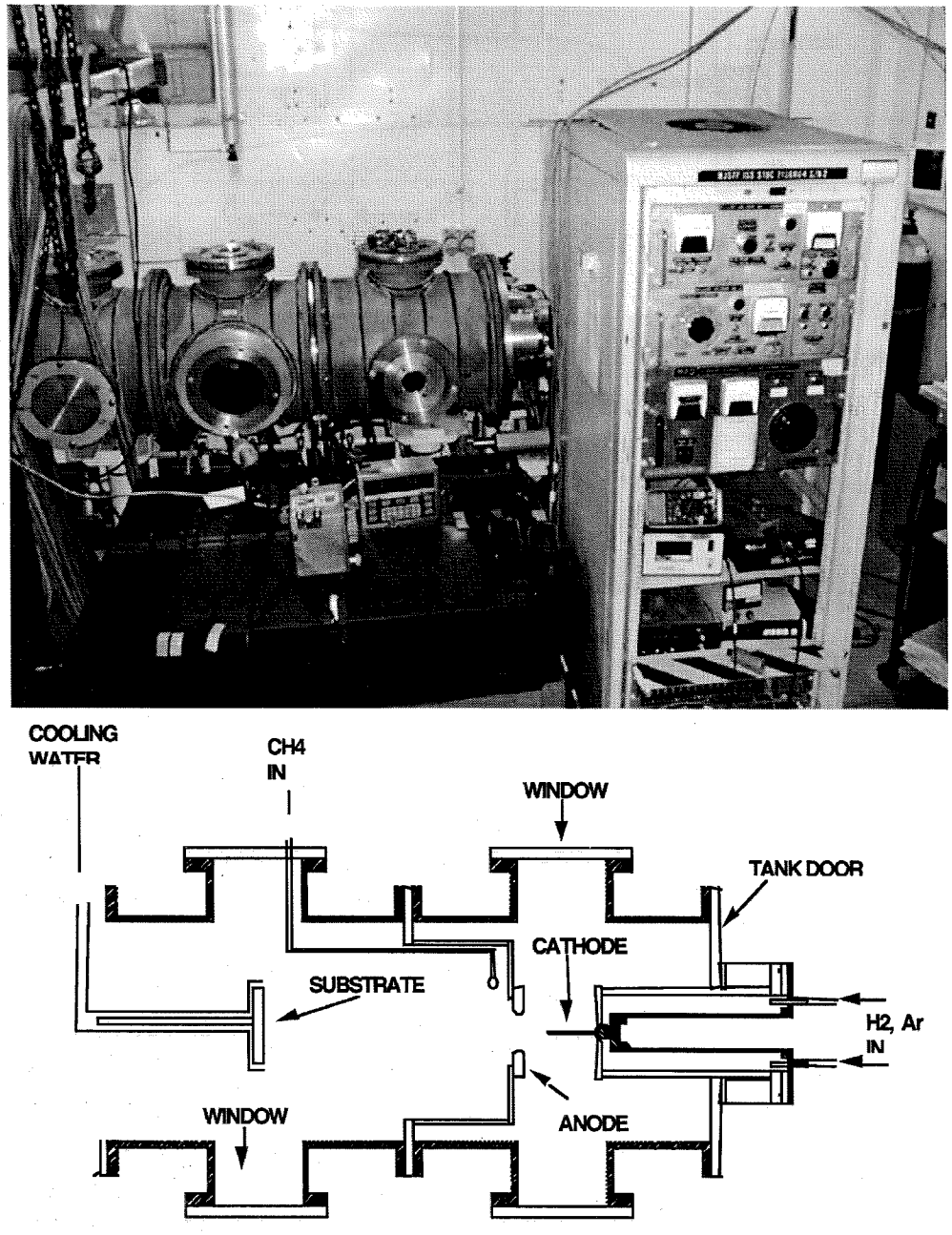

Figure 4.1: Cathode Test Facility at JPL used for MPD assisted diamond film deposition studies

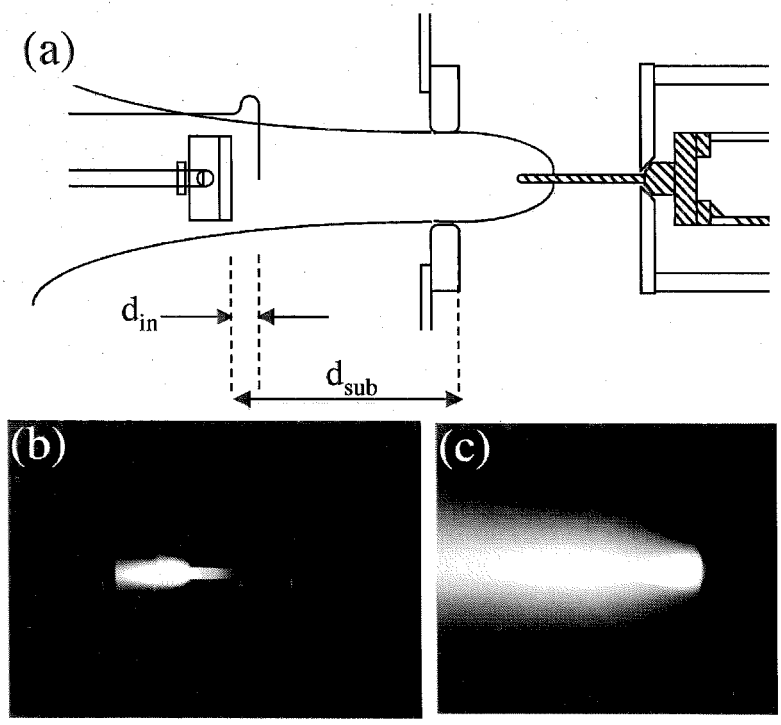

Figure 4.2: a) Internal layout of Cathode Test Facility showing anode, cathode, substrate, and methane injector b) Photograph of cathode in operation on argon c) Photograph of anode in operation on argon

0.3 g/s of argon). Because the efficiency of a blower decreases in the milli-Torr range, the ultimate pressure for this facility was only 10 - 20 mTorr (1.3 - 2.7 Pa).

Figure 4.2 shows the relative location of the water cooled substrate, anode, and cathode within the chamber along with an outline of the visible portion of the plume jet. The cathode is a 0.95 cm diameter, 7.6 cm long thoriated tungsten rod mounted in a water cooled copper mount. The cathode is mounted on the tank door which slides away from the end of the tank on rails for access. The anode consists of a separate, water-cooled copper ring supported by a separate water cooled cylinder supported between the first two tank segments. The anode opening is 7.6 cm in diameter. Figure 4.2(b) and (c) are photos of the discharge, perpendicular to the

cathode and downstream of the anode respectively. These images were taken with the device operating on pure argon at a current of 1000 A and a chamber pressure of 1100 Pa (8.3 Torr). As evident from the open electrode design, this particular configuration was originally designed for easy optical access to the cathode and not for high efficiency acceleration. The design is a derivative of the segmented anode "DT" MPD thruster series built and operated at Stuttgart [85].

In operation, an arc is established by applying a high voltage initially between the electrodes once gas flow has been started. An 850 V, 4 A start supply is used to initiate the arc which is then sustained by one of two available Miller 1500 A, 40 V power supplies. This arrangement enables operation up to 120 kW total power. For the studies reported here, operation was limited to 700 - 950 A at a discharge voltage of approximately 18 V (total power 13 - 17 kW) and was limited primarily by heat flux to the substrate as well as the anode.

No plume velocity measurements have been made with this device, but an upper bound on the gas velocity can be inferred from a review of tests at the Stuttgart facility at similar argon flowrates and operating current. The contoured, segmented anode of the Stuttgart would be expected to provide much more efficient electromagnetic acceleration so the performance at a current of 900 A at an argon flowrate of 0.8 g/sec provides a reasonable upper bound on jet velocity in the JPL facility. From Reference [85], Figure 3, the velocity can be estimated to be approximately 2500 - 3000 m/sec. This velocity is at least a factor of three lower than the jet velocity of an arcjet expanding supersonically into low pressure and represents a significant limitation of the facility used here.

The substrates used for these tests were molybdenum disks, 7.0 cm in diameter and 0.32 cm thick. The molybdenum disks were mounted with four screws to a

water cooled copper support. Three thermocouples are used to measure substrate temperature from behind at the substrate center, and at two points closer to the edge of the disk. Originally, the thermocouples were fixed to spring loaded contacts, recessed into the copper block which would insure contact with the back of the disk. With repeated use the spring mechanism became less reliable and a new approach was adopted in which thermocouple beads, approximately 1 mm in diameter, were inserted into blind holes on the back side of the molybdenum disk. These blind holes extended approximately 1 - 2 mm into the substrate.

Different approaches to control substrate temperature were evaluated including use of dedicated coolant loop using a mixture of water and ethylene glycol with a dedicated chiller. The cooling capacity of this system proved to be insufficient so facility water cooled by a chiller which serves several labs was used instead. The large thermal mass of this system enabled operation without any significant increase in supply-side water temperature.

For all of the tests reported, methane was used as the carbon precursor gas with a hydrogen/argon mixture used in the discharge. Figure 4.3 illustrates four different methane injection schemes investigated. For tests in which the substrate was biased, the gas injector was electrically isolated by means of ceramic standoffs.

4.2 Deposition Studies

As previously mentioned, the jet velocity expected from the MPD used was lower than an arcjet and certainly any MPD source developed for use as a space thruster. As a result, it is unrealistic to expect that the facility available for these tests would be representative, at least with respect to benefits one might expect due to high

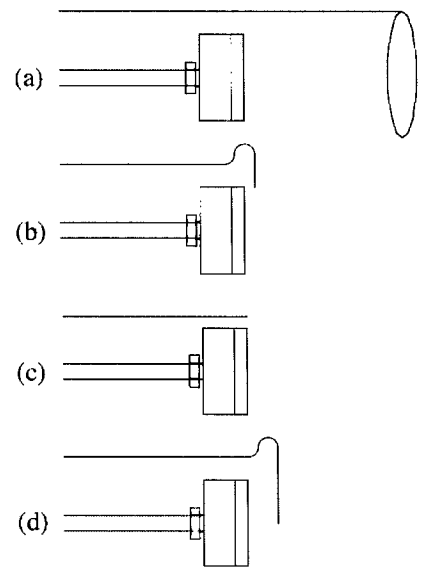

Figure 4.3: Four different methane injector locations investigated

jet velocity (and consequently thin boundary layers with sharp species concentration gradients). Nevertheless, one can expect that results of such an investigation could provide some insight into issues associated with a low pressure, high current discharge which results in higher levels of dissociation and ionization than one would expect in a plasma torch operating near atmospheric pressure. With these limitations in mind, the objectives of the investigation presented in the following sections was 1) demonstrate that diamond films can be deposited with an MPD plasma for gas activation, 2) explore the efficacy of different methane injector configurations, 3) investigate the effect of different methane/hydrogen concentrations, and 4) investigate the effect of substrate biasing. Each of these four objectives is directly relevant to operation with a more conventional MPD designed to achieve high jet velocity.

In all cases studied, the discharge was operated with a nominal mixture of 23 slm argon (0.7 g/sec) with 0.9 slm hydrogen (1.3 mg/sec). Hydrogen results in a higher potential fall through the anode sheath resulting in higher levels of energy deposition

and anode heating than argon. The mixture therefore serves to lower heat load to the anode as well as facilitating arc initiation. Other groups have successfully employed argon/hydrogen discharges in diamond CVD as reviewed in Section 3.1.2 and it is expected that the presence of argon contributes to the chemistry only through third body collision effects.

Substrate temperature was inferred from Type-K thermocouples installed on the back surface of the substrate. Two color optical pyrometry would have been preferable for surface temperature determination but only a one-color pyrometer was available. Observing the disappearing filament through the luminous red hydrogen plume at the substrate proved to be impractical. A large uncertainty in the substrate temperature is due to the significant variations of temperature, greater than 100 C in some cases, from one thermocouple to another suggesting nonuniform heat flux to the surface. The nonuniformity of heat flux to the surface was driven primarily by the fact that plume was not centrally aligned in the chamber and the ability to position the substrate within the plume was limited. The temperature measurements reported are time-averaged to account for the variation in temperature at a given location during the deposition time. This variation over the 70 - 180 minute test periods was typically less than 100 C.

Referring to Figure 4.1, one can see that the anode is mounted to a cylindrical support which is sandwiched between the first two tank segments. The cathode, on the other hand, is mounted to the sliding chamber end door and is therefore subject to slight misalignments every time the chamber is open and closed. This differs from more conventional MPD devices in which the cathode anode are part of a single structure in which the cathode and anode are not moved relative to each other. Misalignment is believed to be at least one contributing cause to the canting of the

plume jet slightly off the central axis.

The location of the substrate relative to the anode exit plane was dictated by thermal considerations. After some experimentation, a distance of approximately 14 cm (measured from the anode face closest to the cathode) was selected. The limitations of the cooling system precluded effective independent control of the substrate temperature. The separation of the substrate from the anode exit plane, combined with the plume canting, initially resulted in the plume core impinging at the edge of the substrate. This was corrected by construction of a substrate positioning system which allowed sufficient control to ensure the plume core was incident on the substrate center. Even with this improvement, the beam incidence on the substrate was several degrees off from an ideal normal incidence characteristic of a stagnation flow geometry.

4.2.1 Methane Injector Location

In deposition experiments using supersonic arcjets, the methane injection occurs very near the exit plane of the divergent nozzle as in the case of Loh, et al. [43,44] discussed in Section 3.1.2. In the present tests, the initial location used for methane injection was a ring with many small holes located just downstream of the anode as depicted in Figure 4.3(a). In this configuration, the injection ring was approximately 14 cm from the substrate surface. The tests performed with this injector ring consistently produced amorphous sooty deposits on the substrate. As will be discussed in Section 5.3, there is an optimal period of time over which methane pyrolysis should be allowed to occur in order to insure the highest possible concentrations of desirable species such as methyl radicals and atomic hydrogen. For the ring injector configuration, even if one assumes the methane is fully entrained in the plasma jet and travels with a velocity

of 2000 m/s, the relatively large distance of the injector from the substrate results in a residence time of 70 μsec. With such a relatively long time for decomposition to occur, the mole fraction of atomic carbon is sufficiently high to produce significant amounts of amorphous deposits.

As a result of these initial tests, the remainder of the testing consisted of using injectors mounted to the substrate support with a single injector tube mounted with different orientations and distances from the substrate surface. After some unsuccessful attempts at using alumina injection tubes, a design using 1.6 mm (o.d.) molybdenum proved effective. The diameter of the visible plume at the substrate position was at least 8 - 10 cm. As a result, the injector tube was subject to significant heat loads even when located off to the side as in Figures 4.3 (b) and (c). The ends of the tubes routinely were heated to incandescence, the high temperatures resulting in significant buildup of amorphous carbon on the ends which effectively altered the injection point and in the most severe cases became flow obstructions. Injector-substrate separation was varied from 0.5 cm to 1.5 cm. Centrally positioned methane injection (as in Figure 4.3 (d)) was used, but the problem of carbon buildup on the tube was far worse when the injector was located in the core than off to the side. Figure 4.4 shows one injector tube located in the center position and positioned 1.5 cm from the substrate surface. This run was done with a methane-hydrogen ratio of 3.2 percent (by volume) over a period of 82 minutes.

In Figure 4.4 the relatively large carbon growth is asymmetrical with the elongated structure extending downstream in the discharge towards the substrate surface. From the figure it becomes apparent that this structure is redirecting the point and orientation from which gas injection is occurring. In this case the test was terminated at the point where the growth actually appeared to begin physically contacting the

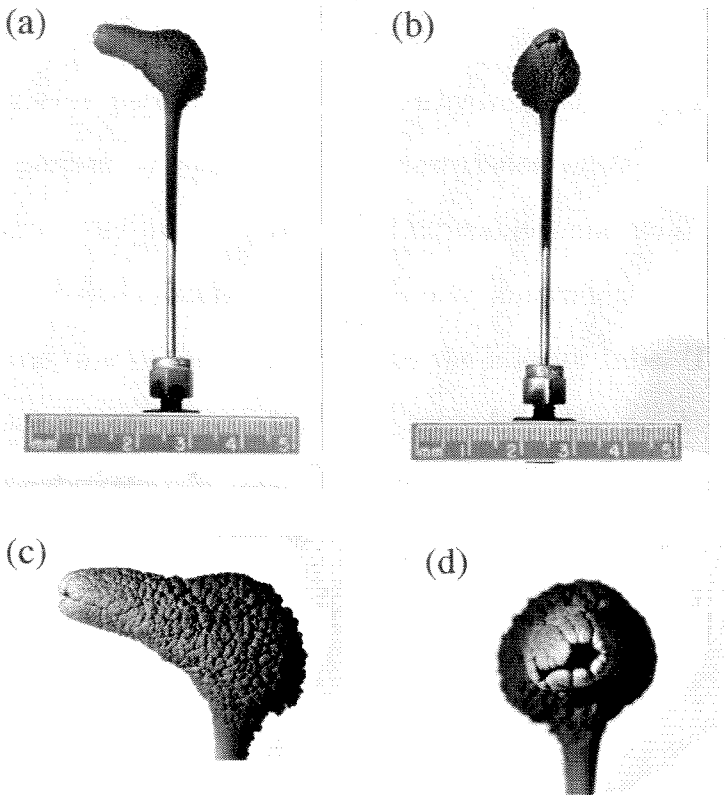

Figure 4.4: Molybdenum injector tube showing amorphous carbon buildup accumulated over 82 minutes of operation

substrate surface. It is also apparent that the carbon deposit can become a significant flow obstruction, with a dimension not insignificant compared to the substrate diameter. As a result of this problem, the injector was located off to side of the substrate as in Figure 4.3 (b) and (c).

In the side location, the carbon deposition was also present but not as problematic. This is likely due to the fact the injector temperature was lower since it was out of the core flow. In this side location, there was still some carbon build-up on the injector and also on the region of the substrate closest to the injector although not nearly as extensive as observed with the centrally mounted injector.

4.2.2 Methane Concentration

Most of the tests were performed at methane/hydrogen concentrations of approximately 1.5 or 3.5 percent by volume. In early tests below a 1.5 percent concentration, there was only some very limited evidence of crystallites and no films. In tests with both the central and side mounted injectors, sooty, amorphous carbon deposits were evident on the substrate in the area closest to the injector tube. This strongly suggests that methane concentration decreased away from the point of injection as it diffused over the substrate. At some position over the substrate the concentration becomes suitable for growth to occur. In all cases, the methane would diffuse from the point of injection over the substrate in complex way depending on the flow field and injector orientation.

4.2.3 Results

Results are presented in this section from six different deposition runs using both the central and side mounted injection tubes and methane concentrations of 1.5 and 3.5 percent. Figures 4.5 through 4.10 show SEM images of the film morphology including an edge view from which the film thickness was determined. Also included in the figures is the Raman spectra taken in approximately the same location as the SEM images as well as the X-Ray diffraction spectra.

The largest continuous films deposited in any of these tests was no more than several square millimeters in size. From Figure 4.1, one can see that the substrate and plasma source are oriented along the horizontal, long axis of the chamber. As a result, upon cooling, some portion of the deposited films would often separate from the substrate in the chamber (and in many cases be lost during tank venting). This would be evident as a distinct region on the substrate where the light gray film would

Test No.	Meth/Hyd Ratio (by vol.)	Inj-sub Distance (d_{in}) (cm)	Inj. Loc.	Anode-Sub Distance (cm)	Deposition Time (min.)	Sub. Temp. (C)
5	3.4	1.3	center	14.1	77	316 - 856
7	3.2	1.5	center	14.1	82	457 - 758
8	3.4	0.5	side	14.1	77	600 - 730
9	3.5	0.5	side	14.6	79	809 - 918
10	1.5	0.5	side	14.6	181	466 - 810
15	1.6	0.5	side	16.2	100	500 - 648

Table 4.1: Test conditions for grounded substrate tests. Side injector location corresponds to position shown in Figure 4.3(b), center injector location as in Figure 4.3(d)

be missing.

For some cases the variation in temperatures across the substrate were several hundred degrees C. Such large variations were at least in part due to the fact the substrate was almost as wide (7 cm in diameter) as the plasma jet itself. Also as described earlier, limits in the positioning system along with plume asymmetries contributed to the plume impinging at up to several degrees from the normal for some cases. Table 4.1 summarizes the deposition conditions for each of these runs including the temperature range measured across the substrate. The range listed represents the spread between the minimum and maximum, time-averaged, substrate temperature measured by the thermocouples.

Morphology

In Figures 4.5 through 4.10, the first SEM image corresponding to a top view of the films are all at the same magnification. From examination of these images the overall morphology can be said to broadly fall into one of three groupings. In Tests 5 and 9 (Figures 4.5 and 4.6) the crystallites which have coalesced into a film are

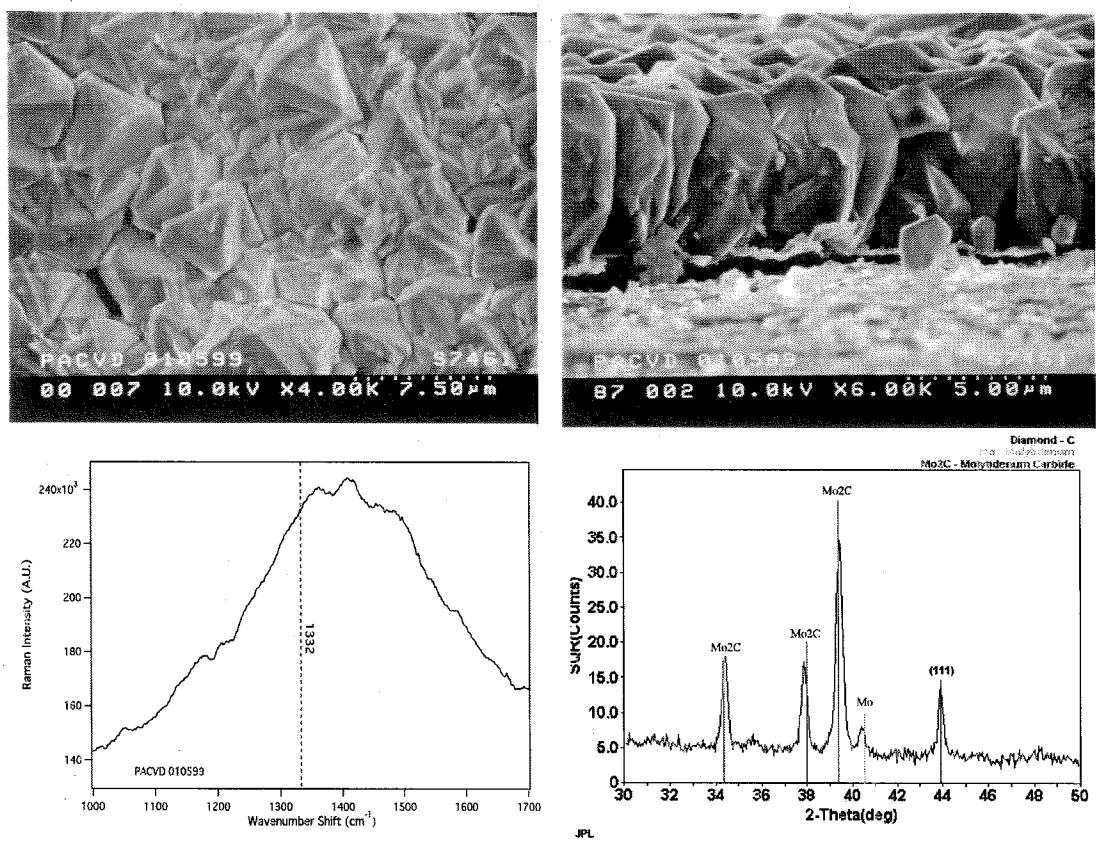

Figure 4.5: Test 5: SEM image, Raman and XRD spectra for MPD assisted film deposition: Meth/Hyd = 3.4%, d_{in} = 1.3 cm, Injector located centrally as in Figure 4.3(d)

approximately 3 - 5 microns across. In Test 5 the facets are comparable to the crystallite dimensions whereas for Test 9, the facets are much finer, less than 1 micron on the larger crystallites.

In Tests 10 and 15 (Figures 4.7 and 4.8), the films also appear to be formed of crystallites which have coalesced but here the characteristic dimension of both the crystallites and their facets is roughly 1.5 microns.

Tests 7 and 8 (Figures 4.9 and 4.10) are the only two tests where the diamond actually appears to have begun developing into a film in which the vertical growth

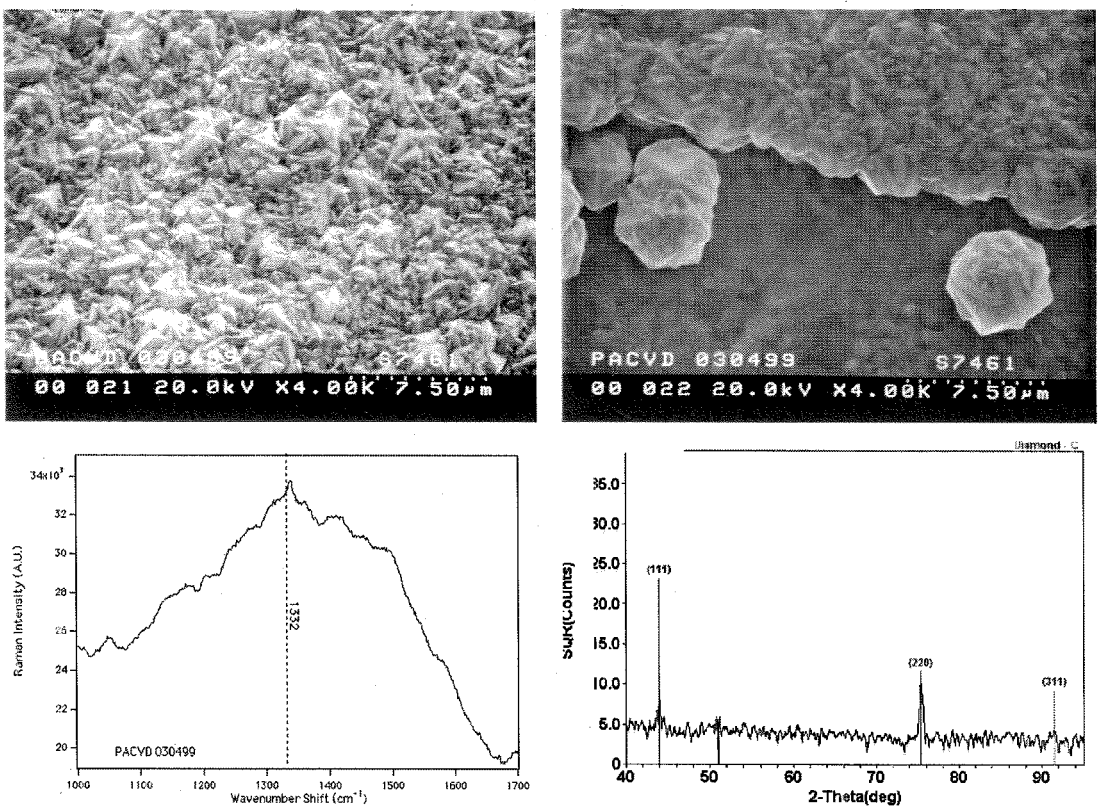

Figure 4.6: Test 9: SEM image, Raman and XRD spectra for MPD assisted film deposition: Meth/Hyd = 3.5%, d_{in} = 0.5 cm, Injector located on side as in Figure 4.3(b)

is many times the characteristic crystallite dimension as can be seen in the cross-sectional images in these Figures.

In all tests, the triangular faceting characteristic of a (111) oriented plane appears the most prevalent which is supported by the XRD spectra.

Raman Spectroscopy

Raman spectroscopy is a technique which has been widely employed in the evaluation of diamond films. When an incident photon induces a transition in the vibrational state of an atom in a crystal lattice, the subsequent relaxation of the exited, tran-

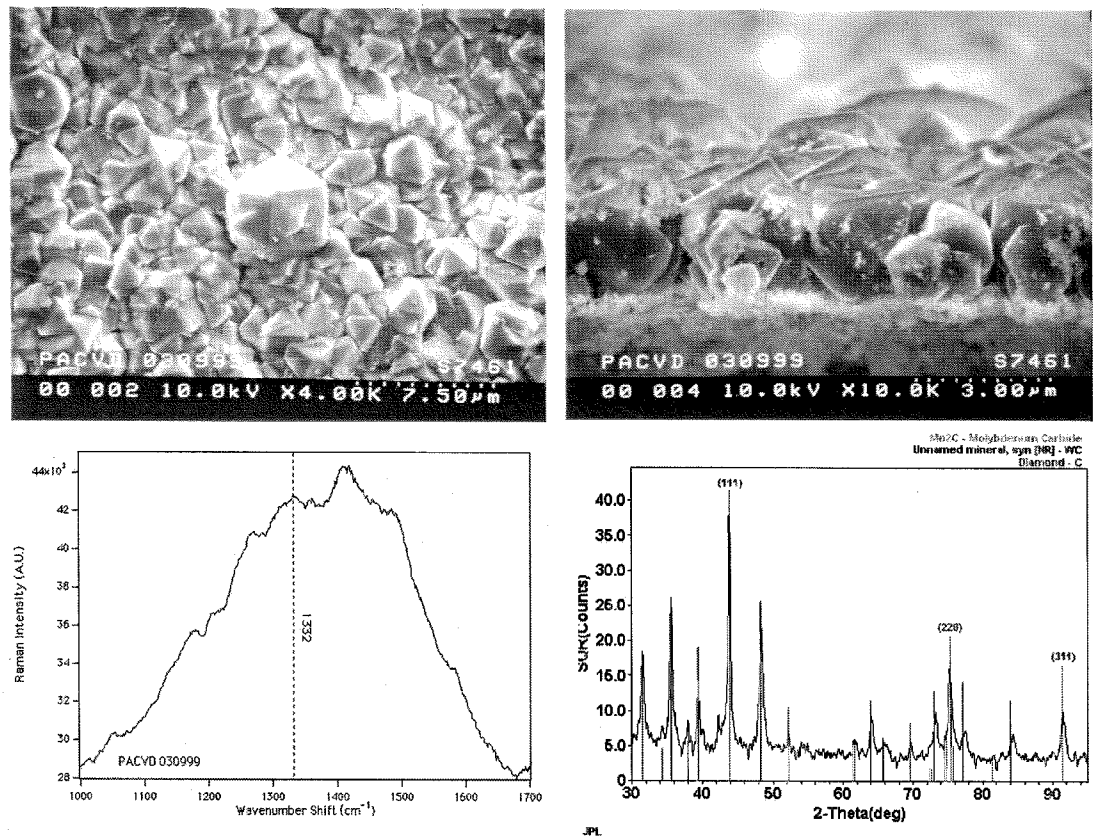

Figure 4.7: Test 10: SEM image, Raman and XRD spectra for MPD assisted film deposition: Meth/Hyd = 1.5%, d_{in} = 0.5 cm, Injector located on side as in Figure 4.3(b)

sitional state to a lower energy state can result in a shift in the wavelength of the reemitted photon. This inelastic process produces a distinct spectral line in diamond at a wavelength shift of 1332 cm^{-1}. For a sample which is relatively free of impurities and defects, this line is very sharp with a full width-half maximum (FWHM) spread of less than 10 cm^{-1}. This peak is due to diamond crystallites with a high level of sp^3 bonding present. For lower quality samples some other features which are sometimes observed include a broad peak at 1510 cm^{-1} due to amorphous carbon with sp^2 bonding and also a broad feature at 1350 cm^{-1} due to graphite [86].

The instrument used for this work was a HoloProbe Raman System manufactured by Kaiser Optical Systems Inc. A 785 nm laser with a power level of 50 mW was used which is focused through a microscope onto the sample enabling a spatial resolution of 0.5 - 2.0 μm.

Figures 4.5 through 4.10 show the Raman spectra for deposited samples. While some minor features are evident, none of these spectra contained the 1332 cm^{-1} peak characteristic of sp^3 bonded diamond. In addition, all the spectra appear to display a broader background, possibly due to luminescence of the samples. Two possible explanations for the poor Raman spectra of these samples are incorporation of nitrogen and a high level of defects localized along the grain and twin boundaries.

In one study by Vandevelde [87] a systematic investigation was made of the effect of different levels of nitrogen incorporation, one of the most common impurities in diamond. While relatively low levels of nitrogen in the gas phase ($<$ 100 ppm) can contribute to higher quality structures, a high nitrogen concentration in the gas phase results in films with a higher degree of graphitic and amorphous carbon [87].

In the Vandevelde study, nitrogen concentrations in the gas stream were increased from 95 ppm to 714 ppm. This increase resulted in a decrease in both the sharpness and intensity of the 1332 cm^{-1} Raman peak as shown in Figure 4.11. In addition to its affect on the Raman line characteristic, addition of nitrogen was also found to result in a preferred (100) orientation in the film morphology.

It is likely that nitrogen present in the gas stream during deposition played some role in the overall poor quality of the films as evident in the Raman spectra. Despite numerous attempts to eliminate all gas leaks in the chamber used for deposition, it is estimated the background residual partial pressure of air could have been as high as 10 mTorr. For a nominal operating chamber pressure of 8.5 Torr, this corresponds

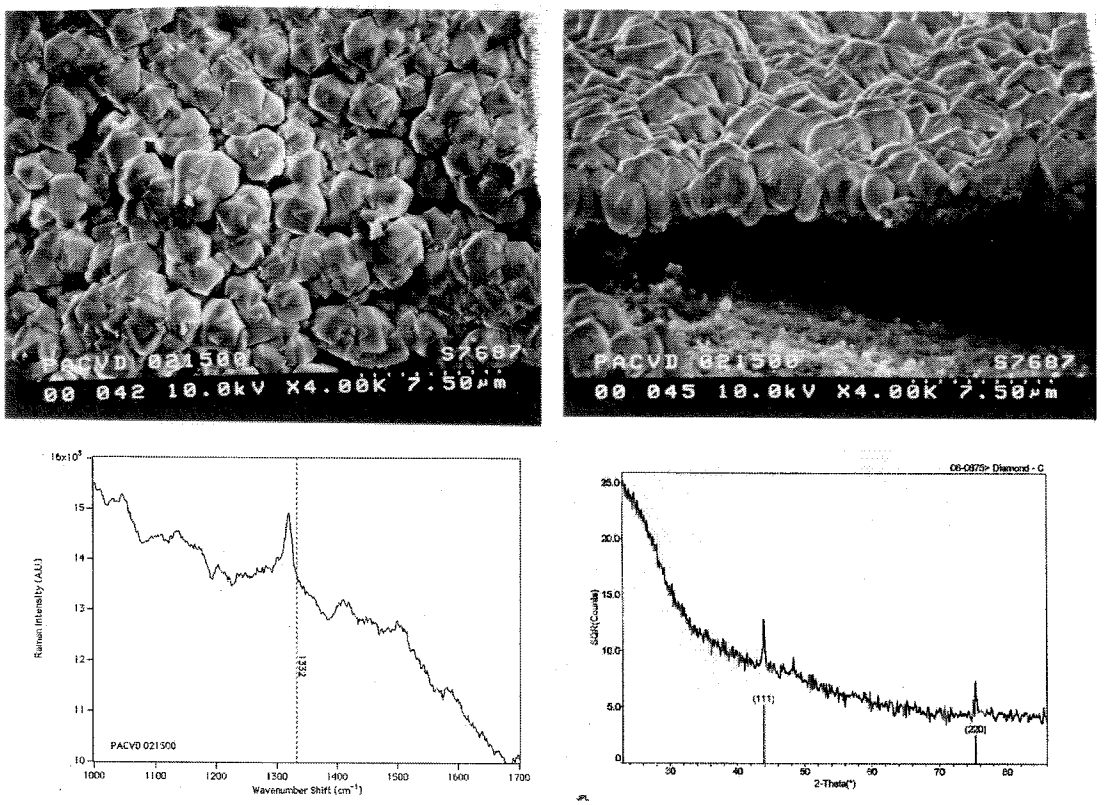

Figure 4.8: Test 15: SEM image, Raman and XRD spectra for MPD assisted film deposition: Meth/Hyd = 1.6%, d_{in} = 0.5 cm, Injector located on side as in Figure 4.3(b)

to a nitrogen concentration of approximately 930 ppm. Based on the the Vandevelde study, such a high concentration could easily account for the suppression of sp^3 bonded carbon.

A second possible explanation is the generally fine grain size of the films deposited with extensive twin boundaries. Von Kaenel and his group investigated the evolution of several Raman spectral features for films deposited for varying periods of time [88]. The samples in this study were deposited with a microwave reactor on a silicon substrate. In particular, in addition to the sharp Raman line at 1332 cm^{-1} with a full width-half maximum spread of 6 - 10 cm^{-1}, they also tracked the evolution of disor-

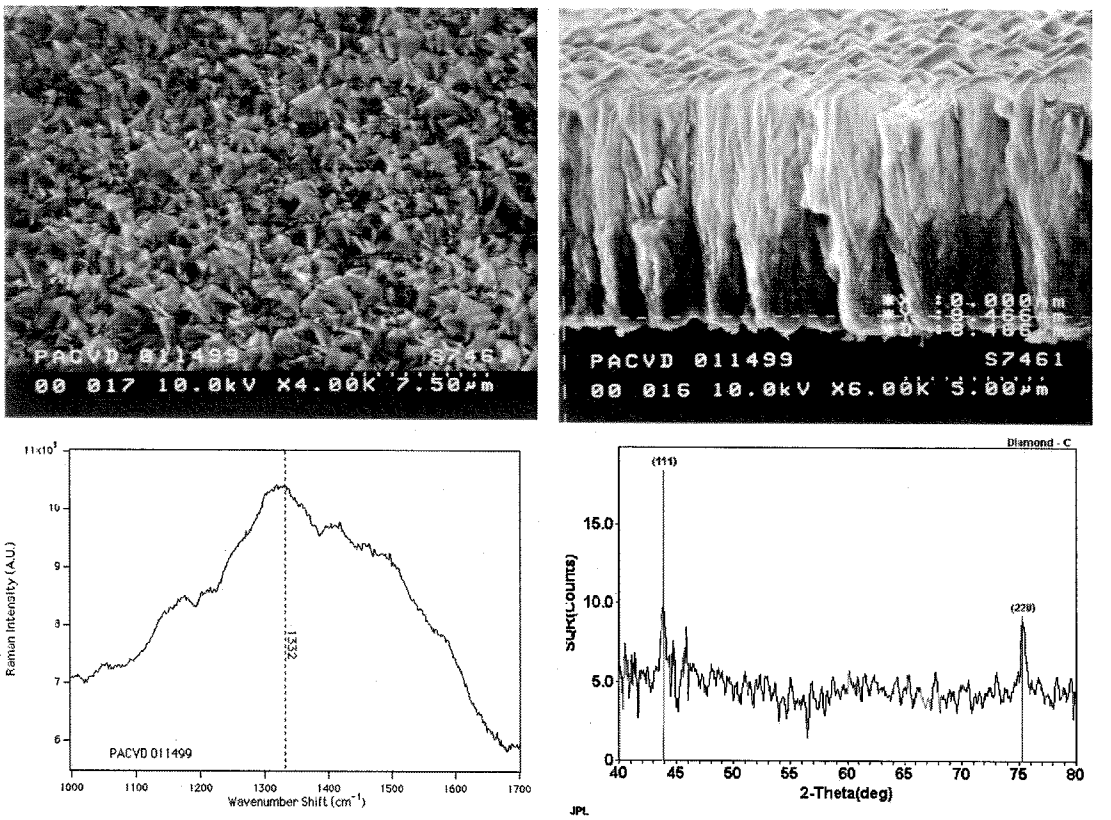

Figure 4.9: Test 7: SEM image, Raman and XRD spectra for MPD assisted film deposition: Meth/Hyd = 3.2%, d_{in} = 1.5 cm, Injector located centrally as in Figure 4.3(d)

dered graphite peak at approximately 1340 cm^{-1} (FWHM $\approx$ 300 cm^{-1}), graphite-like carbon peak at approximately 1520 cm^{-1} (FWHM $\approx$ 150 cm^{-1}), and what they believed to be a broad luminescence background at peak at approximately 1815 cm^{-1} (FWHM $\approx$ 500 cm^{-1}).

Electron Spin Resonance (ESR) was used as an independent technique to quantify defect densities due to carbon dangling bonds or dangling bond-hydrogen complexes [88]. The ESR signal was found to correlate well with the graphite-like defects as indicated by the Raman spectra. Because of this strong correlation, the authors proposed that the defects are largely due to these bonding defects, as verified by the

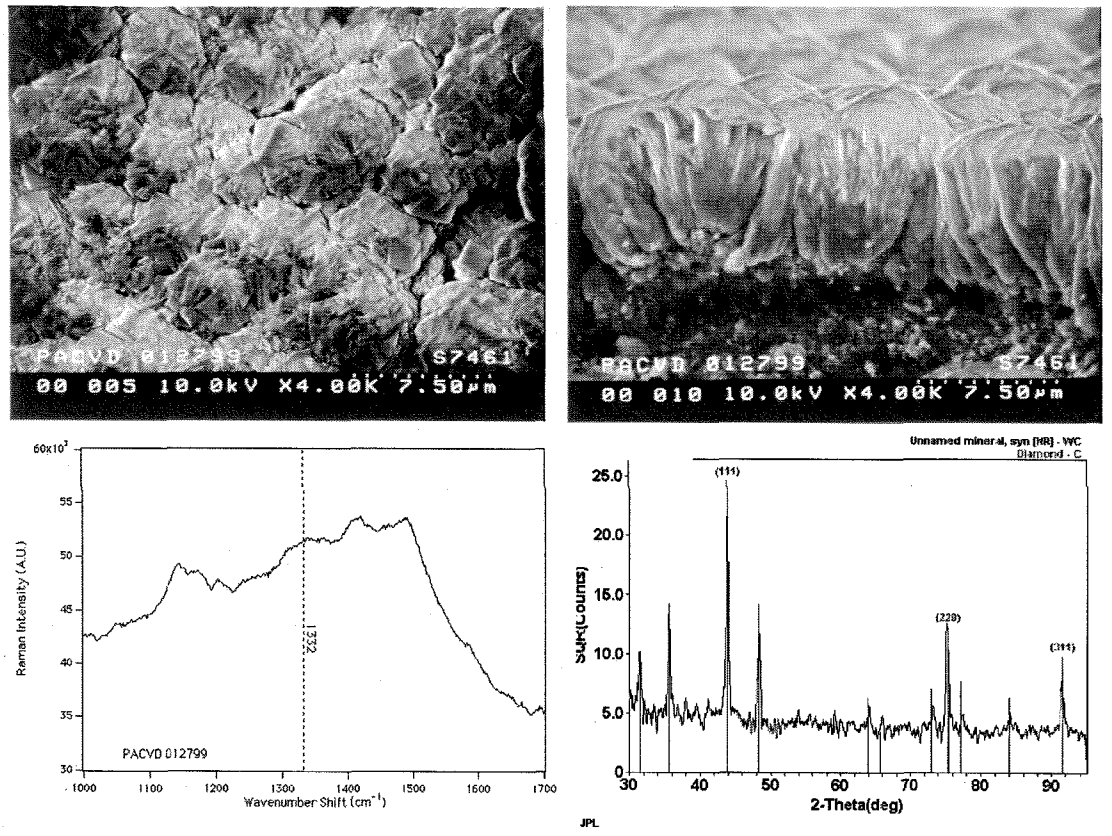

Figure 4.10: Test 8: SEM image, Raman and XRD spectra for MPD assisted film deposition: Meth/Hyd = 3.4%, d_{in} = 0.5 cm, Injector located on side as in Figure 4.3(b)

ESR measurements, which are believed to be located primarily along the grain and twin boundaries. This was further supported by the fact that the quality is found to improve as the film grows over a period of four hours and the grain size increases. Finally as the growth continues further and grain size ceases to change further with time, the defect density is also found to stop changing with time.

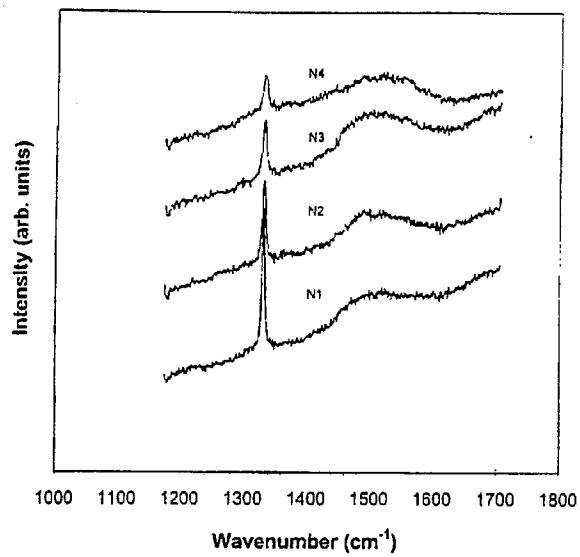

Figure 4.11: Sensitivity of Raman spectra to nitrogen concentration during deposition: spectra labeled N1 through N4 correspond to nitrogen levels of 95, 191, 286, and 714 ppm respectively (from Reference [87])

X-Ray Diffraction

The last panel in Figures 4.5 through 4.10 are the XRD spectra for each sample. In cases where film could be separated easily from the substrate, the scans were performed on the loose flakes/powder. Otherwise, the substrate was scanned in the approximate region where the SEM had identified some film or crystallites.

At least one diamond peak can be unambiguously identified in each of the samples tested. In some cases other materials were identified as well and are indicated on the spectra. These included molybdenum carbide (Test 5 and 10), tungsten carbide (Test 8 and 10), and molybdenum (Test 5). The molybdenum is likely due to either the substrate itself or the injection tube while the tungsten is from the cathode.

Test No.	Meth/Hyd Ratio (by vol.)	Inj-sub Dist. (cm)	Inj. Loc.	Anode-Sub Distance (cm)	Dep. Time (min.)	Sub. Temp. (C)	Bias Voltage (V)
12	1.6	0.5	side	14.7	93	603 - 752	50
13	1.6	0.5	side	14.7	97	885 - 951	75
14	1.5	0.5	side	14.8	90	973 - 1171	50
16	1.6	0.5	side	16.2	93	300 - 643	50
17	1.6	0.5	side	16.2	84	876 - 909	50
18	1.6	0.5	side	16.2	155	328 - 537	75

Table 4.2: Test conditions for biased substrate tests. Side injector location corresponds to position shown in Figure 4.3(b).

4.2.4 Substrate Biasing

Several tests were performed with positive substrate biasing to study any effects on deposition rate or morphology. As discussed in earlier chapters, the MPD operates at lower discharge pressures and higher currents than an arcjet which leads to higher levels of dissociation and ionization. Several groups have reported enhancement of deposition when the substrate is positively biased as discussed in Section 3.1.2. This is believed to be due to the acceleration of electrons in the sheath which leads to additional atomic hydrogen via electron impact dissociation.

In this work tests were performed with the substrate biased to 25, 50, and 75 volts above facility ground. Above 75 V arcing became more frequent and precluded going to higher voltages. The methane injector tube was grounded to the facility and electrically isolated from the substrate by ceramic spacers built into its mount. While the exact location of the arcing was not determined, it was most likely to the injector tube which was located only 0.5 cm away from the substrate.

No films were deposited in any of the biased deposition tests. Figure 4.12 shows some of the isolated crystallites observed after the 75 V test cases. Table 4.2 sum-

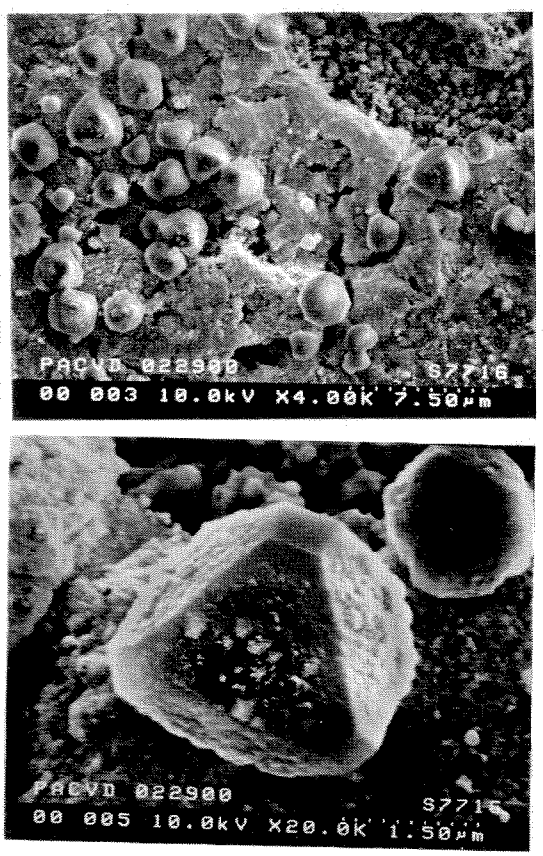

Figure 4.12: Test 18: SEM image of isolated crystallites deposited during test with 75 V positive bias. Meth/Hyd = 1.6%, Injector-Substrate separation = 0.5 cm, Injector located on side as in Figure 4.3(b)

marizes the test conditions for these tests. Because of the limited extent of even crystallite formation, no Raman or XRD spectra was obtained for these tests, therefore, a conclusive identification was not made.

One possible explanation for the absence of any significant growth for the biased cases may be due to the level of ionization and the low drift velocity of the hydrogen in the plume. While ionization is apparently beneficial to the extent that it provides free electrons which can enhance dissociation in the sheath, too high a level of ionization will likely be counterproductive. The reasoning for this is that any positive

hydrogen ion must overcome the potential barrier through the sheath to reach the substrate surface. For a bias of 25 V, a hydrogen ion would require a kinetic energy corresponding to a velocity of 69.2 km/sec. This corresponds to a specific impulse for an electric thruster of over 7000 sec which is high, even for an MPD device. Therefore, one would expect that for any MPD device, and certainly the one used for these tests with a jet velocity of several kilometers per second at most, a high level of ionization would drastically reduce atomic hydrogen flux to the growth surface.

4.3 Conclusions

This chapter has presented results from a series of tests using an MPD plasma source for gas activation in diamond synthesis. Figures 4.5 through 4.10 and Table 4.1 summarize these results for six different tests. In these studies, crystalline films were deposited and identified as diamond through X-Ray diffraction spectra. All Raman spectra for these samples showed a broadband background with no distinct feature at the characteristic 1332 cm^{-1} wavelength shift characteristic of diamond. This indicates poor quality of the films deposited which could be due to a number of causes including significant residual nitrogen in the growth environment due to the pumping facility used in the facility.

Figure 4.13 presents the growth rate calculated for each of these tests as a function of substrate temperature, methane concentration and injector location. As noted earlier, the significant uncertainty in the temperatures are a result of significant radial temperature variation across the relatively large substrate. For all of the deposition tests presented in this Chapter the hydrogen mass flowrate was approximately 1.3 mg/sec. If one assumes the plume diameter at the substrate is 10 cm (estimated

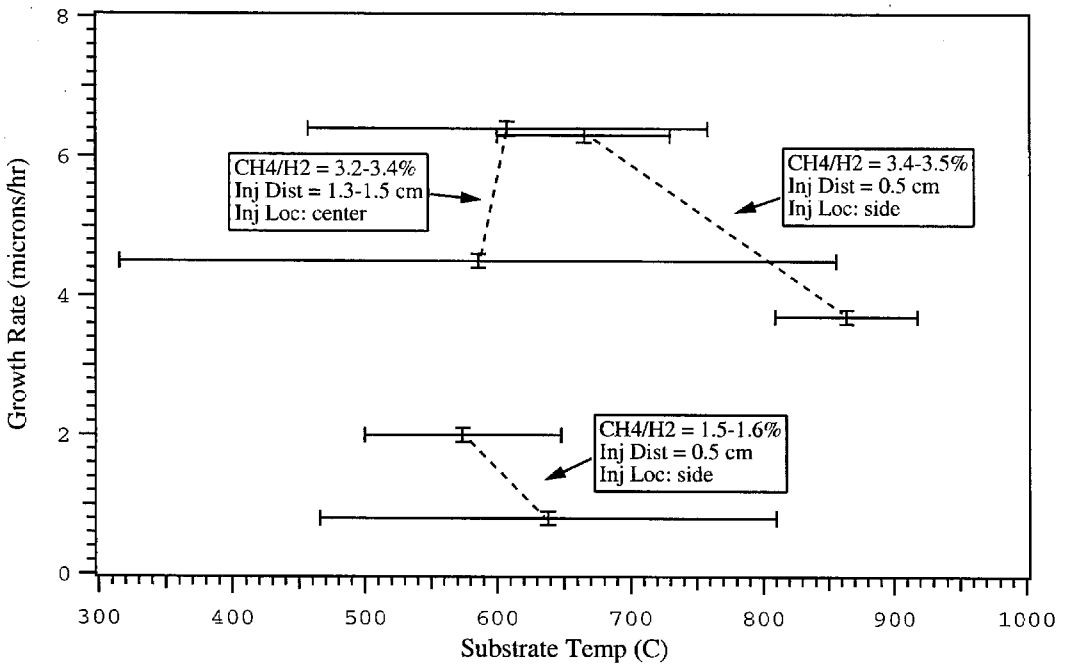

Figure 4.13: Growth rate assuming zero nucleation time for grounded substrate tests presented in Figures 4.5 through 4.10 as a function of substrate temperature

from visual inspection and comparison with the 7 cm diameter substrate), and that the methane is uniformly distributed in the plume, then it is possible to estimate the maximum theoretical growth rate if 100 percent of the carbon reaching the substrate is incorporated into the film. For the methane-hydrogen ratios of 1.5 and 3.5 percent this maximum growth rate is 15 and 35 μm/hr respectively. So the highest growth rates measured at the two mixture ratios were 13 - 18 percent of their maximum limiting value.

In addition, some issues associated with the injection of the methane became apparent during these studies. The severe heat fluxes associated with the MPD plume, even at low jet velocities, requires either very effective active cooling or increasing the distance between the exit plane and the substrate. Increasing the distance results

in increased residence time for methane pyrolysis if the methane injection port is located at the MPD exit plane. This was overcome by moving the injector closer to the substrate. As a result, however, excessive heating at the injector opening resulted in high rates of amorphous carbon deposition at the tip with subsequent flow disruption.

Finally several tests were also performed to investigate the effect of substrate biasing on film deposition. None of these tests produced extended films or even significant areas of crystallite deposition. One possible reason for this is the higher level of ionization insures that a smaller fraction of the available atomic hydrogen population will have sufficient energy to overcome the potential barrier through the sheath and make it to the growth surface.

In summary, diamond deposition was demonstrated using an MPD accelerator as a gas activation source. Growth rates and deposition areas were lower than the 10 μm/hr over 1 - 2 cm^2 which have been reported for supersonic arcjet deposition at higher velocity [44]. Film quality was low, most likely due to a combination of residual nitrogen and electrode vapor contamination. Metallic contaminants from the tungsten cathode and molybdenum methane injector likely were the causes of tungsten carbide and molybdenum carbide detected in some of the samples.

Chapter 5

Comparison of Electromagnetic and Electrothermal Plasma Sources

5.1 Atomic Hydrogen Transport to the Substrate

In Section 3.2.2, three potential benefits of the MPD plasma source for diamond CVD were identified. These were 1) larger plume cross sectional area permitting more uniform deposition over larger substrates, 2) higher jet velocities, resulting in thinner boundary layers with sharper concentration gradients and higher fluxes of atomic hydrogen, and 3) higher levels of dissociation/ionization benefiting the use of a secondary biased-substrate discharge to promote electron heating and even higher levels of dissociation. Table 3.1 summarized the dimensions and operating characteristics of a number of plasma sources which have been operated by a variety of groups in both steady and quasi-steady modes. From an inspection of the anode

radii for these devices it can be seen that exit beam diameters of 5 -10 cm are not uncommon. While the question of uniformity across this cross sectional area has yet to be addressed, it is apparent that MPDs, because they do not rely on nozzle expansion for gas acceleration, may possess inherent area scaling advantages over more conventional arcjet sources as listed in item 1 above.

In Section 5.1.1 some of the characteristics of the hydrogen MPD plume will be discussed and used as a basis in Section 5.1.2 for estimating the relative advantage of the higher jet velocity over that of an arcjet to deliver a higher flux of atomic hydrogen to the growth surface. In Section 5.2 the effectiveness of heating electrons in the boundary layer through a secondary discharge will be investigated.

The larger exit plane area of the MPD may be advantageous from the standpoint of larger substrate coverage, but it also worsens the problem of achieving uniform methane entrainment and mixing in the hydrogen jet flow. As will be seen in Section 5.3, one would ideally like for this entrainment to happen on a timescale of several microseconds.

5.1.1 Hydrogen MPD Plume Characteristics

Section 3.2 summarized the work of a number of groups that have investigated MPD operation on hydrogen propellant. Most of the available information deals with the performance of the device as a thruster, however, with data consisting primarily of measured and calculated efficiencies, thrust levels, and specific impulse. Far less information is available with respect to plume characterization, especially with hydrogen. One of the more complete data sets is that of Tahara et al. [77]. This work is a combination of numerical calculation and experimental measurements. Most of the properties in the plume are calculated using an axisymmetric flowfield simulation.

	$r = 0$	$r = r_a$
U_a (km/sec)	71	35
T_g (eV)	2.2	1.1
P_g (Pa)	119	—
α_e	0.9 - 1.0	0.75
α_d	0.9 - 1.0	0.9 - 1.0

Table 5.1: Estimated plume data from calculations of Tahara et al., Ref. [77]: Calculations correspond to quasi-steady MPD operation with hydrogen at J=5 kA, $\dot{m}$=0.4 g/sec, r_a=2.5 cm and r_c=0.95 cm. Data are listed for locations corresponding to centerline and radial location equal to the anode radii at an axial location 4.0 cm downstream.

A significant weakness of this work is the assumptions made regarding thermal and chemical equilibrium. Table 5.1 lists estimates of axial jet velocity U_a, gas temperature T_g, static pressure P_g and degree of ionization α_e and dissociation α_d obtained from Reference [77]. The values correspond to an downstream axial position of approximately 4 cm and radial locations of both centerline and r = 2.5 cm. For the stream pressure, only a centerline value is listed due to a lack of contour plot data provided in the reference at this location (the centerline value had to be extrapolated from data closer to the exit plane).

The velocity listed represents an upper bound since the simplifications involved in the numerical model, such as assuming an expression for conductivity equal to that of a fully ionized plasma, and neglect of energy losses which limit the amount of energy which can be converted into kinetic energy.

The use of the Saha equilibrium relation likely results in an overestimate of the degree of ionization. It is more likely the electron temperature is much higher than the translational heavy particle temperature, especially close to the exit plane. One expects therefore the actual heavy particle temperature to be lower, and the electron

temperature higher than this equilibrium estimate. The hydrogen is likely to be nearly if not fully dissociated at these temperatures and pressure.

The data in Table 5.1 therefore provides a reference point only for the discussion in the following sections; for a 5 cm diameter device, operating at a current level of 5 kA and voltage of approximately 120 V, one can expect average jet velocities of 25 - 35 km/sec, a static pressure in the stream of 100 - 150 Pa, fully dissociated hydrogen temperature of at least 10000 K, and ionization levels of at least 50 percent. For a jet cross section of 5 cm, a one percent methane to hydrogen ratio, and the hydrogen mass flowrate of 0.4 g/sec used in the Tahara MPD, the maximum theoretical growth rate of a diamond film if 100 percent of the carbon reaching the substrate is incorporated into the film is 11800 μm/hr (11.8 mm/hr).

5.1.2 Scaling of Hydrogen Transport with Pressure and Velocity

In this section we use the hydrogen MPD plume characteristics from Section 5.1.1 to evaluate the relative advantages of the higher gas temperature and velocity of an MPD over more conventional arcjet sources. First the mean free paths will be estimated for conditions representative of both the plume and substrate stagnation flows. This information is important in order to understand the flow regimes and validity of continuum assumptions at different points in the flow. A scaling relation for the atomic hydrogen mole fraction at the substrate, relative to that in the free stream, developed by Goodwin [89] is then used to compare atomic hydrogen transport to the substrate surface for the two sources.

Since the hydrocarbon fraction in the process flow is typically only a few percent at most, the atomic hydrogen mean free path is estimated neglecting methane content.

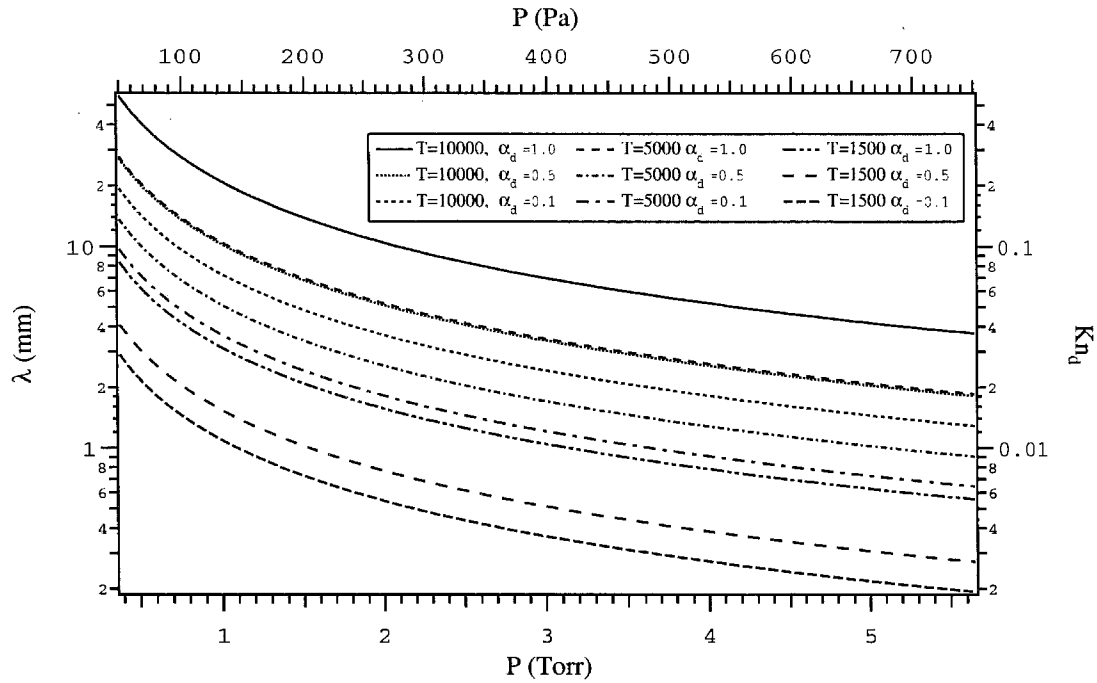

Figure 5.1: Atomic hydrogen mean-free-path and Knudsen number (based on a 10 cm. substrate diameter) as a function of pressure, temperature (in Kelvin), and degree of dissociation

Following methods described in Vincenti and Kruger [90] and also used by Loh [91] in his analysis of the arcjet plume, the mean free path is given by

$$\lambda_H = \frac{\bar{c}_H}{\theta_H + \theta_{H_2}} \tag{5.1}$$

where the mean thermal speed of the hydrogen atoms $\bar{c}_H$ is given by

$$\bar{c}_H = \sqrt{\frac{8kT_g}{\pi m_H}} \tag{5.2}$$

The terms θ_H and θ_{H_2} represent the collision frequency of hydrogen atoms with hydrogen atoms and molecules respectively and are given by

$$\theta_H = \sqrt{2}\pi n_H d_H^2 \bar{c}_H$$

and

$$\theta_{H_2} = \pi n_{H_2} d_r^2 \bar{c}_r$$

where the reduced (hard sphere) diameter d_r is

$$d_r = \frac{d_H + d_{H_2}}{2}$$

and the reduced mean thermal velocity $\bar{c}_r$ is given by Equation 5.2 using the reduced mass

$$m_r = \frac{m_H m_{H_2}}{m_H + m_{H_2}} \tag{5.3}$$

The calculated atomic hydrogen mean free path and Knudsen number (based on a substrate diameter of 10 cm) are shown in Figure 5.1. The range of temperatures is representative of values near the substrate (1500 K), and two stream temperatures (5000 K and 10000 K). From the data in Table 5.1, 10000 K is likely to be a low bound for a several hundred kilowatt MPD whereas 5000 K is a high bound for an arcjet. Downstream of the plasma source, at a pressure of 100 Pa and gas temperature of 10000 K, Figure 5.1 illustrates the flow is in a transition regime between continuum and free molecular flow ($0.01 < Kn_d < 1$). The supersonic stagnation flow will form a bow shock in front of the substrate. The pressure in the boundary layer will be lower than the stagnation pressure due to pressure loss through the shock. In the calculations which follow, the normal shock relations have been used to estimate the total pressure loss through the bow shock. The mean free path in the stream is tens of millimeters so the shock will be diffuse. These diffuse shocks have been observed by Loh in arcjet flows [91]. From studies done with air in shock tubes [92], the shock stand-off distance for a 180 degree wedge (flat disk) of diameter d will range from $5.5d$ to $1.3d$ for approach Mach numbers ranging from 1.2 to 1.7.

For a gas temperature of 10000 K, static pressure of 100 Pa, and a jet velocity of 25 km/sec, the corresponding Mach number is 2.1 and the stagnation pressure (downstream of the shock) is 5.4 Torr (714 Pa) for a ratio of specific heats γ equal to 1.67 (all atomic hydrogen). If one assumes a ratio of specific heats γ equal to 1.4 (all molecular hydrogen), these stream conditions correspond to a Mach number of 3.3 and a stagnation pressure of 10.8 Torr (1436 Pa) downstream of the shock. From Figure 5.1, for a temperature in the boundary layer close to the substrate of 1500 K, one can see either of these bounds (5.4 - 10.8 Torr) correspond to $Kn_d < 0.01$ which is in the continuum flow regime.

From the data in Figure 5.1 it is evident that the flow in the MPD jet will be in a free molecular regime in the region downstream of the source exit plane where methane injection would occur. From kinetic theory, the viscosity of the fully dissociated hydrogen stream can be expressed in terms of the gas density ρ, thermal velocity $\bar{c}$, and mean free path λ as [93]

$$\mu = \frac{1}{3}\rho\bar{c}\lambda \tag{5.4}$$

The Reynolds number in terms of the substrate diameter d_s can then be written

$$Re_{d_s} = \frac{3U_a d_s}{\bar{c}\lambda} \tag{5.5}$$

where U_a is the stream velocity. Considering the case of a fully dissociated hydrogen flow with a temperature of 10000 K and pressure of 100 Pa, the Reynolds number corresponding to stream velocities of 15 - 30 km/sec are 1.1 - 2.2. Although the velocities are very high, the high temperature and low density result in a laminar flow into which the methane must be injected.

Goodwin [89] has derived a useful relationship for understanding atomic hydrogen

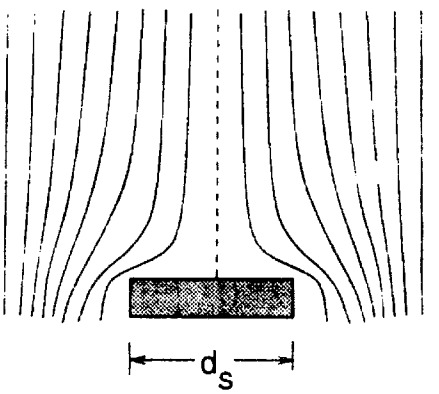

Figure 5.2: Idealized stagnation flow geometry with uniform free-stream approaching substrate with diameter d_s (Ref. [89])

transport to the substrate surface in both diffusion and convection limited processes. In his analysis, an idealized stagnation flow geometry is assumed in which the incident jet is uniform and undisturbed by the substrate is shown in Figure 5.2. This idealized flow geometry is approximated in practice if one considers only fraction of the substrate with a diameter smaller than that of the incident jet.

Details of the derivation of Goodwin's scaling relation are provided in the Appendix. The ratio of the atomic hydrogen mole fraction at the surface X_{H_o} to that in the free stream X_{H_∞} is found to scale with the pressure p in the stagnation region and the velocity gradient parameter a as

$$\frac{X_{H_o}}{X_{H_\infty}} = \left(1 + 110\sqrt{\frac{p}{a}}\right)^{-1} \tag{5.6}$$

where p has units of Torr and a has units of $\sec^{-1}$. The velocity gradient parameter can be interpreted by referring to Figure 5.3. The radial velocity component will increase from its value of zero in the free stream to some maximum value just outside the momentum boundary layer, then decrease to a value of zero (through the no-

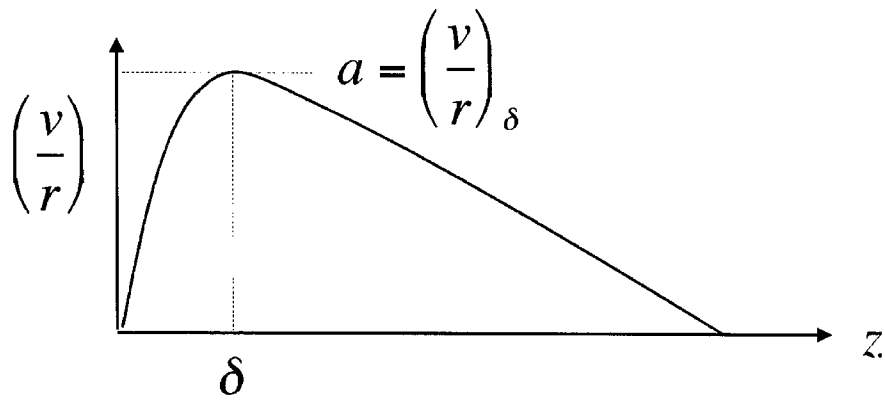

Figure 5.3: The velocity gradient parameter can be interpreted physically as the maximum value of the ratio of the radial velocity to the radial coordinate. This maximum corresponds to the radial velocity at the edge of the boundary layer.

slip condition) at the surface. The velocity gradient parameter a can be interpreted as the maximum value of the ratio of the radial velocity component divided by the radial coordinate. This maximum occurs at the edge of the boundary layer where the velocity is greatest.

Some limiting assumptions made in deriving Equation 5.6 include the applicability of continuum flow approximations, neglect of any gas phase chemistry, as well as the assumption of uniform density and transport properties implicit in the assumed expression for the boundary layer thickness (see Equation A.5 in the Appendix). While these limiting assumptions preclude using Equation 5.6 to calculate an absolute numerical estimate of the atomic hydrogen concentration, the relation does illuminate the relative effects of process pressure, velocity (and Mach number) as well as substrate diameter in maximizing the hydrogen flux to the substrate.

Goodwin evaluates the implications of this scaling relationship for both diffusion and convection dominated processes. For a convection dominated process, the second term on the right-hand side of Equation 5.6 should be of order one so that the ratio

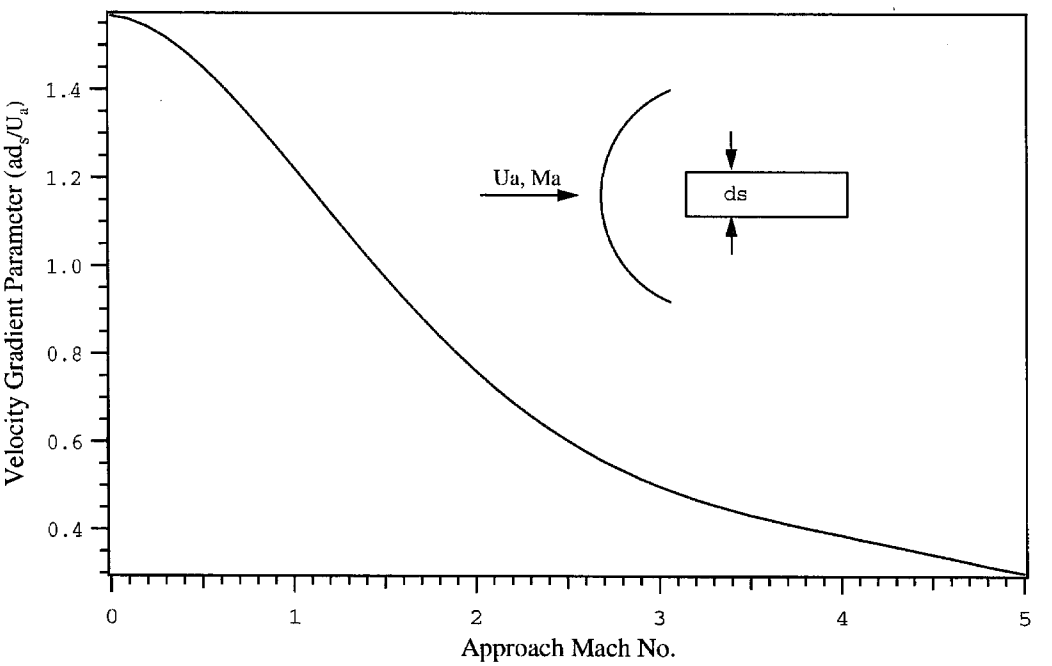

Figure 5.4: Velocity gradient parameter as estimated by White [94] as a function of approach Mach number for the case of impingement on a flat disk

of atomic hydrogen at the substrate to that in the free stream is of order one. This implies a processes characterized by a high velocity jet (or smaller substrate diameter) resulting in a high velocity gradient such that the ratio p/a is less than 10^{-4} Torr sec. A diffusion limited process, on the other hand, will be one in which lower velocities (or larger substrates) result in a value of the velocity gradient parameter a such that the ratio p/a is greater than 10^{-4} Torr sec.

In reality, the pressure p is not decoupled from the velocity, since the higher the approach Mach number, the higher the stagnation pressure will be. The result is that there exists an optimal Mach number which minimizes the p/a ratio and hence maximizes the atomic hydrogen through Equation 5.6. Reference [89] explores this optimal Mach number for the case of an electrothermal accelerator. In an electrother-

mal accelerator, the amount of kinetic energy which can be recovered in the jet is limited by the stagnation temperature in the arc-heating chamber (and is usually limited by material constraints). In an electromagnetic accelerator the velocity is not directly coupled to the stagnation temperature.

Equation 5.6 can be used to evaluate and compare the relative hydrogen concentration and optimal Mach number for an electrothermal and electromagnetic plasma source; however, a few more comments are warranted regarding the applicability of Equation 5.6 to the velocity and temperature regime characteristic of an MPD plume. The derivation of Equation 5.6 assumed a regime characterized by continuum flow. From Figure 5.1, at a gas temperature of 10000 K, a velocity of 25 km/sec, and static pressure of 100 Pa, the stagnation pressure (including effect of shock pressure loss) ranges from 5.4 - 10.8 Torr for $\gamma = 1.67$ and $\gamma = 1.4$ respectively (with corresponding Mach numbers of 2.1 - 3.3). So for a Mach number greater than 2, the use of Equation 5.6 (with respect to the continuum flow assumption) is justified. The approximations made for the boundary layer thickness include constant properties which are harder to justify for the case of an MPD stagnation flow where the stagnation temperature (translational) outside the boundary layer can be greater than 30000 K. In Reference [89] the boundary layer thickness approximations are found to agree with a numerical solution of the stagnation flow to within $\pm$ 20 percent for free stream temperatures up to 5000 K. The agreement is expected to be poorer for the very high temperatures expected in an MPD stagnation flow. For this reason Equation 5.6 is only used for a relative comparison.

As the flow impinges upon the substrate, the purely axial jet is decelerated, the axial velocity component going to essentially zero at the surface (Equation A.1 in the Appendix implies a small velocity, the Stefan velocity, at the surface). The velocity

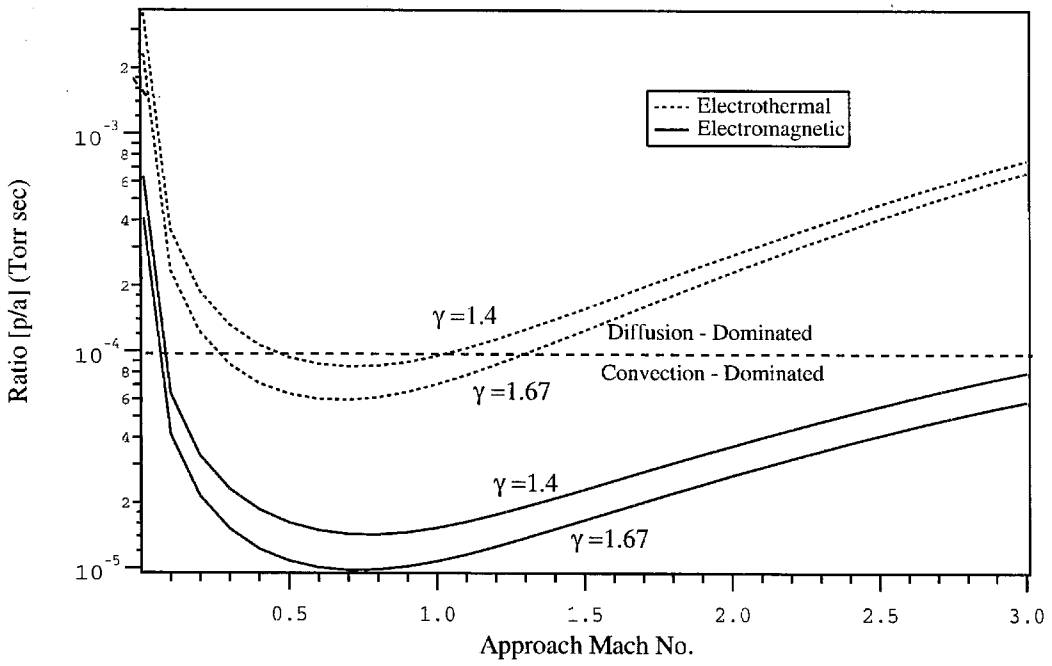

Figure 5.5: Ratio of the stagnation pressure to the velocity gradient parameter for electrothermal and electromagnetic accelerators: Bounding curves shown for all atomic or all molecular hydrogen flows.

gradient parameter scales with the ratio of the approach velocity U_a to the substrate diameter d_s as

$$a = C(M_a)\frac{U_a}{d_s} \tag{5.7}$$

The scaling function $C(M_a)$ is experimentally determined for specific stagnation surface geometries. White [94] provides experimental data for a sphere and estimates the function for a flat disk. This estimate is shown in Figure 5.4. A bow shock will be present in the case of a supersonic incident flow and is accounted for in the estimate by White.

Using the velocity gradient parameter function from Figure 5.4, the ratio p/a was calculated for the case of an electrothermal accelerator, in which the stream velocity is

related to the Mach number M_a and stagnation temperature T_o through the standard gasdynamic relations [89]

$$U_a = M_a \left(\frac{\gamma R T_o}{M}\right)^{\frac{1}{2}} \left(1 + \left(\frac{\gamma - 1}{2}\right) M_a^2\right)^{-\frac{1}{2}} \tag{5.8}$$

where M is the gas molecular weight, and γ is the ratio of specific heats. The stream velocity given by Equation 5.8 approaches a limiting value as the Mach number approaches infinity. This result is in contrast to an electromagnetic accelerator, where the attainable stream velocity is determined by the power available and efficiency of the energy conversion process. The sonic velocity will still be determined by the static temperature, but the velocity (and Mach number) can, at least in principle, be increased arbitrarily.

Figure 5.5 shows the stagnation pressure to velocity gradient ratio for both an electromagnetic and electrothermal accelerator. For the electrothermal case, a stagnation temperature limit of 5000 K (an upper bound) has been assumed. For the electromagnetic case, the Mach number is based on a sonic speed calculated at a static temperature of 10000 K. A static pressure of 100 Pa and 400 Pa has been assumed for the electromagnetic and electrothermal cases respectively. The two families of curves correspond to ratio of specific heats γ corresponding to purely atomic or purely molecular hydrogen. The dotted line delineates the approximate boundary ($p/a \approx 10^{-4}$ Torr sec) between diffusion and convection dominated processes as defined by Goodwin.

From Figure 5.5 it is apparent that although the jet velocity of an electromagnetic accelerator is not limited by gas dynamic energy recovery, and hence the stagnation temperature, the stagnation pressure which scales as the square of the Mach number increases faster than the velocity gradient parameter resulting in a minimum for this

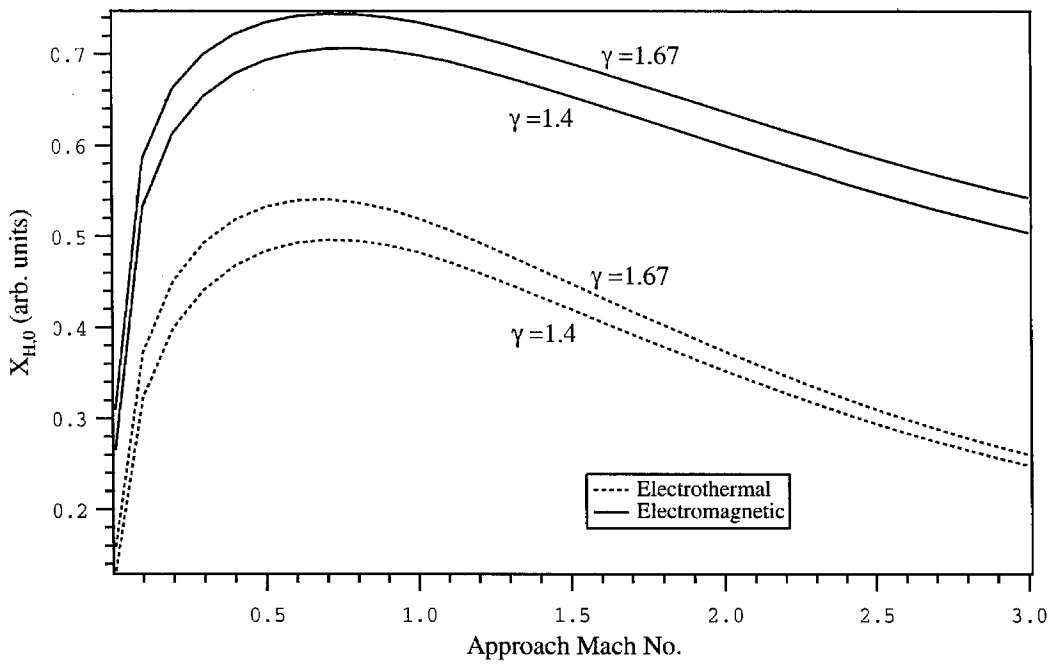

Figure 5.6: Relative atomic hydrogen mole fraction at substrate surface for electrothermal and electromagnetic accelerators: Bounding curves shown for all atomic or all molecular hydrogen flows.

ratio. The important conclusion from this is that even for an MPD accelerator, at sufficiently high Mach numbers the atomic hydrogen flux to the surface will once again be diffusion limited as in a lower velocity process. Referring back to Equation 5.6 one can anticipate that the presence of a minimum in the p/a ratio results in an optimal Mach number for the electromagnetic case as Goodwin observed for the electrothermal case. The results from using Equation 5.6 with the same assumptions used in calculating Figure 5.5 are shown in Figure 5.6.

Both families of curves in Figure 5.6 show the same general behavior. The electromagnetic and electrothermal cases reach a maximum value at approximately the same Mach number. For a ratio of specific heats $\gamma = 1.67$ the optimal approach Mach number is found to be 0.7 for both the electrothermal and the electromagnetic case.

This optimal value is relatively unchanged for the case with $\gamma = 1.4$ with values for the electrothermal and electromagnetic cases equal to 0.7 and 0.8 respectively. The optimal Mach numbers correspond to stagnation pressures of 1.10 - 1.15 Torr for a static pressure of 100 Pa so the flow will be borderline transition-continuum (depending on location in the thermal boundary layer). The constant property assumptions inherent in Equation 5.6 preclude its use for absolute prediction of hydrogen transport but some insight into the relative performance between the two cases is possible. Comparing the hydrogen concentrations at the optimal Mach number, the relative improvement of the electromagnetic case over the electrothermal case is found to be 38 percent with $\gamma = 1.67$ increasing to 42 percent with $\gamma = 1.4$.

5.2 Bias Enhanced Electron Heating

As described in section 3.1.2, several groups have been able to enhance deposition through the use of a secondary discharge through the stagnation boundary layer. It is believed that the biasing serves to heat the free electrons which can then increase the rates of hydrogen and hydrocarbon dissociation in the stagnation boundary layer. In an MPD plume, levels of dissociation and ionization can be significantly higher than in an arcjet. In this section, mechanisms of energy deposition in the plume will be investigated to better understand what the effect of the higher level of ionization is on the effectiveness of a bias discharge in electron heating.

In his thesis, Baldwin [95] investigated the electron catalyzed chemistry in the boundary layer using both experimental and analytical techniques. The increase in electron temperature over the heavy gas temperature was estimated through the use of a simplified electron energy balance. In this analysis the energy addition to the

electrons through ohmic heating is balanced by energy transfer to the heavy species through elastic and inelastic collisions. It was observed that much of the energy is lost through inelastic collisions of electrons with hydrogen molecules and therefore does not go into electron heating. A similar approach is used here to investigate the effectiveness of electron heating through the use of a biased substrate. In addition to looking at gas composition representative of an MPD source, additional inelastic cross sections are incorporated including rotational excitation of hydrogen and vibrational excitation of methane through electron impact.

5.2.1 Simplified Electron Energy Balance

In Reference [96] Meeks provides a detailed solution for the problem of a weekly ionized argon plasma impinging on a cooled, biased substrate. Her sheath solution is self-consistent with the Poisson equation being solved jointly with the conservation equations. In this section, the approach used by Baldwin [95] will be followed to estimate the efficacy of electron heating through a secondary discharge across the stagnation boundary layer. In both the work of Meeks and Baldwin, the neutral particles are assumed to be in equilibrium with each other but not with the electrons. The electrons are assumed to be described by a separate Boltzman distribution. The electron energy equation can be written [95]

$$\frac{D}{Dt}(\frac{3}{2}n_e k T_e) + n_e \frac{5}{2} k T_e \vec{\nabla} \cdot \vec{u} + \vec{\nabla} \cdot \vec{q_e} - \vec{j_e} \cdot \vec{E} = \frac{3}{2} k n_e (T_g - T_e) \sum_{i=1}^{n} 2 \frac{m_e}{m_i} \nu_{ei} + \dot{R}_{inel} \quad (5.9)$$

The first term on the left-hand side of Equation 5.9 represents the time dependent variation of the electron energy. This is followed by a term representing convective transport of thermal energy due to spatial velocity gradients. The third term rep-

resents thermal conduction in terms of the electron heat flux $\vec{q_e}$. The last term on the left-hand side is the Joule heating term which represents energy addition through resistive heating due to a current density $\vec{j_e}$ established by an applied electric field $\vec{E}$. The first term on the right-hand side represents the coupling of energy between the electrons and heavy species through momentum transfer collisions with frequency ν_{ei}. This is almost the same form of the energy equation as used by Baldwin except that the last term representing the inelastic energy loss, $\dot{R}_{inel}$, is included explicitly as done by Meeks. In Reference [95] Baldwin uses an inelastic collision loss factor which multiplies the momentum energy transfer term on the right-hand side instead of a separate term for the inelastic losses. The inelastic energy loss term is intended to account for the enhanced energy transfer from electrons to various excitable modes in the hydrogen and hydrocarbon molecules.

For the purpose of evaluating the simplified energy balance, Baldwin further considers the case of a uniform, steady, one-dimensional, plasma in which the Joule heat addition is balanced by elastic and inelastic collision losses. With these simplifying assumptions, the energy equation reduces to

$$-j_e E = \frac{3}{2} k n_e (T_g - T_e) \sum_{i=1}^{n} 2 \frac{m_e}{m_i} \nu_{ei} + \dot{R}_{inel} \tag{5.10}$$

Using Ohm's law along with the scalar conductivity to express the electric field as $E = j/\sigma$, the equation can be rewritten in terms of the electron temperature increase over the gas temperature

$$T_e - T_g = \frac{\frac{j^2}{\sigma} - \dot{R}_{inel}}{\frac{3}{2} k n_e \sum_{i=1}^{n} 2 \frac{m_e}{m_i} \nu_{ei}} \tag{5.11}$$

where the sum is over all the electron momentum transfer collision frequencies with

the heavy species. The scalar conductivity σ is given by

$$\sigma = \frac{n_e e^2}{m_e(\sum_{i=1}^{n} \nu_{ei} + \sum_{j}^{m} \sum_{i=1}^{n} (\nu_{ei})_j)} \tag{5.12}$$

In this equation the collision frequencies are summed over all elastic and inelastic processes. The elastic collision frequency ν_{ei} is given by

$$\nu_{ei} = n_i v_{ei} Q_{ei} \tag{5.13}$$

where Q_{ei} is the elastic collision cross section and the mean relative thermal speed v_{ei} is given by

$$v_{ei} = \sqrt{\frac{8kT_e}{\pi m_r}}$$

which is based on the electron temperature and the reduced mass m_r

$$m_r = \frac{m_e m_i}{m_e + m_i} \tag{5.14}$$

The second term with the double sum in Equation 5.12 represents the frequency of the j^{th} inelastic collisional process of electrons with the i^{th} heavy species.

$$(\nu_{ei})_j = n_i v_{ei} (Q_{ei})_j \tag{5.15}$$

In actuality, the stagnation boundary layer will be characterized by significant concentration and temperature gradients as well as a collisional sheath so the mechanisms for energy exchange are far more complex than suggested by Equation 5.11. However, given that the secondary discharge is the primary mechanism for energy input directly to the electrons, Equation 5.11 represents a bounding case since the neglected processes represent additional energy losses for the electrons, not energy sources. This equation is a closed-form energy balance applied to a control volume

with a cross-sectional area roughly equal to that of the substrate and thickness equal to that of the electric sheath.

5.2.2 Electron-Hydrogen and Electron-Methane Excitation Cross Sections

This section summarizes the cross sections used for evaluation of Equation 5.11. The electron temperature was not expected to be significantly higher than that of the heavy species in the stagnation region. In selecting what processes to include, the energy range of interest was limited to electron energies in the range of 0.1 - 1.0 eV since heavy species temperatures of 0.34 - 0.43 eV were considered for the calculations. Published cross sections for electron impact dissociation of methane, for example, indicate a threshold of approximately 10 eV and so therefore were not considered.

The momentum transfer cross sections for electrons with atomic and molecular hydrogen are given in Baldwin [95] and shown in the top panel of Figure 5.7. Most of the sources reviewed in Reference [97] show the vibrational excitation of hydrogen to be significant only at energies above 1 eV. Rotational excitation on the other hand for ($J = 0 \rightarrow 2$ and $J = 1 \rightarrow 3$) are excited at energies below 0.1 eV. These cross sections are shown in middle panel of Figure 5.7.

The cross sections for electron impact vibrational excitation of methane were obtained from Reference [98] and are shown in the bottom panel of Figure 5.7. The methane molecule has nine vibrational modes, four of which have distinct energies [98] ($\epsilon_1 = 0.363$ eV, $\epsilon_2 = 0.190$ eV, $\epsilon_3 = 0.374$ eV, and $\epsilon_4 = 0.162$ eV). In the measurements reported by Tawara, the energy differences between the 1 and 3, and 2 and 4 levels were indistinguishable. The cross sections for these two pairs of levels are therefore shown as two (and not four) curves in Figure 5.7.

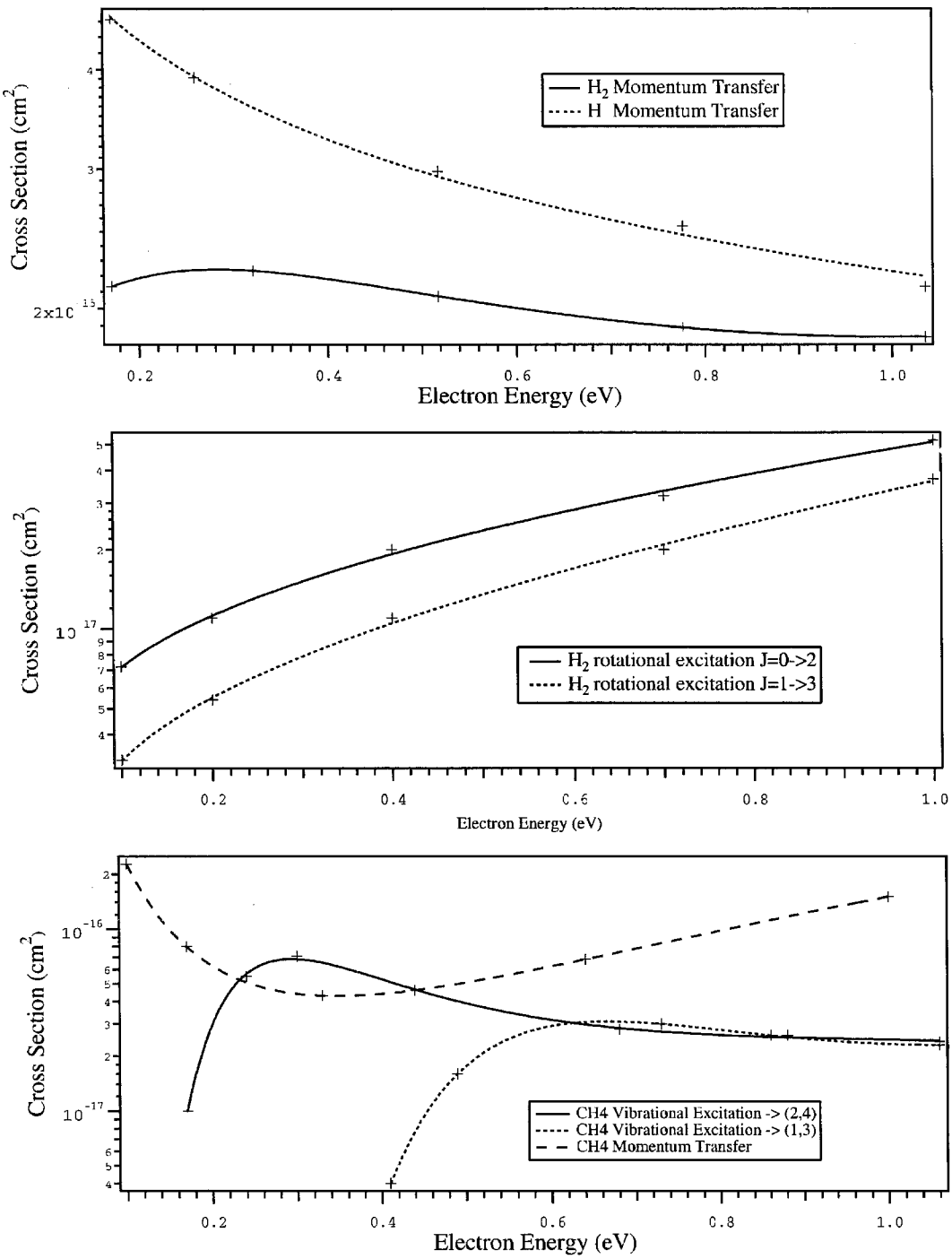

Figure 5.7: Top: Electron impact, momentum transfer cross sections for H and H_2 from Ref [95], Middle: Cross sections for electron impact induced rotational excitation of H_2 from Ref [97], Bottom: Cross sections for electron-methane momentum transfer and electron impact induced vibrational excitation of H_2 from Ref. [98]

Cross Section	a_0	a_1	a_2	a_3	a_4
CH_4 momentum transfer	-15.824	2.0077	0.62859	-3.3609	-1.8019
CH_4 vib $\rightarrow (1,3)$	-16.633	-0.4047	6.4998	22.772	-25.558
CH_4 vib $\rightarrow (2,4)$	-16.609	-0.23993	-0.78007	-12.132	-16.097
H momentum transfer	-14.652	-0.4188	0	0	0
H_2 momentum transfer	-14.735	-0.00798	1.1173	2.0934	0.99655
H_2 rot $0 \rightarrow 2$	-16.291	1.296	0.65474	0.21224	0
H_2 rot $1 \rightarrow 3$	-16.44	1.6978	1.0185	0.3781	0

Table 5.2: Polynomial fit coefficients for cross sections shown in Figure 5.7

For use in subsequent calculations, the cross sections Q have been fit using fourth order polynomial functions of the form:

$$logQ = a_0 + a_1\eta + a_2\eta^2 + a_3\eta^3 + a_4\eta^4 \tag{5.16}$$

where $\eta = log(T_e)$ with T_e given in eV and Q in units of cm^2. The coefficients are summarized in Table 5.2.

These values for the cross sections were used in the evaluation of the inelastic energy loss term in Equation 5.11. The energy loss term is a function of the collision rates and the energy loss per collision event ϵ_{ij};

$$\dot{R}_{inel} = n_e \sum_{i=1}^{n} \sum_{j=1}^{m} (\nu_{ei})_j \epsilon_{ij} \tag{5.17}$$

where again the collision frequency $(\nu_{ei})_j$ represents the frequency of the j^{th} collisional process of electrons with the i^{th} heavy species.

For the electron energy loss per event ϵ_{ij} (again for the j^{th} collisional process of electrons with the i^{th} heavy species) a value of 0.176 eV was used for the vibrational excitation of methane to the 2^{nd} or 4^{th} level and 0.369 eV for excitation to the 1^{st} or 3^{rd} levels. The rotational excitation of hydrogen can be expressed in terms of the

rotational quantum number as [99]

$$E_r = \frac{\hbar^2}{2I} r(r+1) \tag{5.18}$$

Using a value of $\frac{\hbar^2}{2I} = 7.56 \text{ x } 10^{-3}$ eV for H_2 from Reference [99] yields an energy of 0.045 eV for $J = 0 \rightarrow 2$ and 0.076 eV $J = 1 \rightarrow 3$.

5.2.3 Electron Heating

In this section the electron energy balance given by Equation 5.11 is used along with the cross sections presented in the last section to estimate the increase in electron temperature for a given applied current density. The bias voltage required to obtain a given current density will vary with the plasma conductivity for each case, and solution of the sheath potential profile requires a significantly more involved calculation such as done by Meeks [96] for an argon jet. Four different cases are considered and summarized in Table 5.3. These different cases are intended to be representative of a hydrogen-methane plasma one might expect in a CVD application. The degree of dissociation of the hydrogen, α_d, defined as the ratio of the number density of atomic hydrogen (both neutral and ions) to the total number of hydrogen atoms present;

$$\alpha_d = \frac{n_H + n_{H^+}}{n_H + n_{H^+} + 2n_{H_2}} \tag{5.19}$$

has been set to 0.9 for the four cases considered. The ionization fraction, α_e, defined as the ratio of the number density of ions (or electrons) to the heavy particle number density of the mixture

$$\alpha_e = \frac{n_e}{n_o} = \frac{n_{H^+}}{n_o} \tag{5.20}$$

has been set to 0.25 or 0.05. Higher levels of ionization are typically achieved within the MPD source as well as downstream, but one expects lower levels of ionization closer to the substrate where pressures are higher in the stagnation region. Temperatures of 4000 K and 5000 K are assumed which is low for the free stream translational temperature but not unreasonable for some point within the thermal boundary layer where the temperature drops from its free-stream value to the temperature corresponding to the substrate (roughly 1500 K). A pressure of 100 Pa is used in Case 1 and is representative of the pressure in the free stream. A pressure of 333 Pa (2.5 Torr) as used in Cases 2, 3 and 4 is more representative of the stagnation pressure for a flow with a Mach number of approximately 1.5 and a free stream pressure of 100 Pa. The pressure determines the total number density through the following equation:

$$P = (1 - \alpha_e) n_o k T \tag{5.21}$$

The ratio of the methane to hydrogen volumetric flow rates f_q is an additional independent variable which is related to the ratio of the methane to hydrogen mass flow rates f_m through the following relations.

$$f_q = \frac{\dot{Q}_{CH_4}}{\dot{Q}_{H_2^0}} \tag{5.22}$$

In Equation 5.22, $\dot{Q}_{H_2^0}$ is the inlet flow of hydrogen prior to any dissociation or ionization. The inlet hydrogen number density n_{H^0} is related to the stream values through conservation of hydrogen atoms;

$$n_{H^0} = n_H + n_{H^+} + 2n_{H_2} \tag{5.23}$$

Equation 5.23 insures that the calculated mole fractions for different levels of dissociation and ionization are consistent with the value of f_q specified (which is

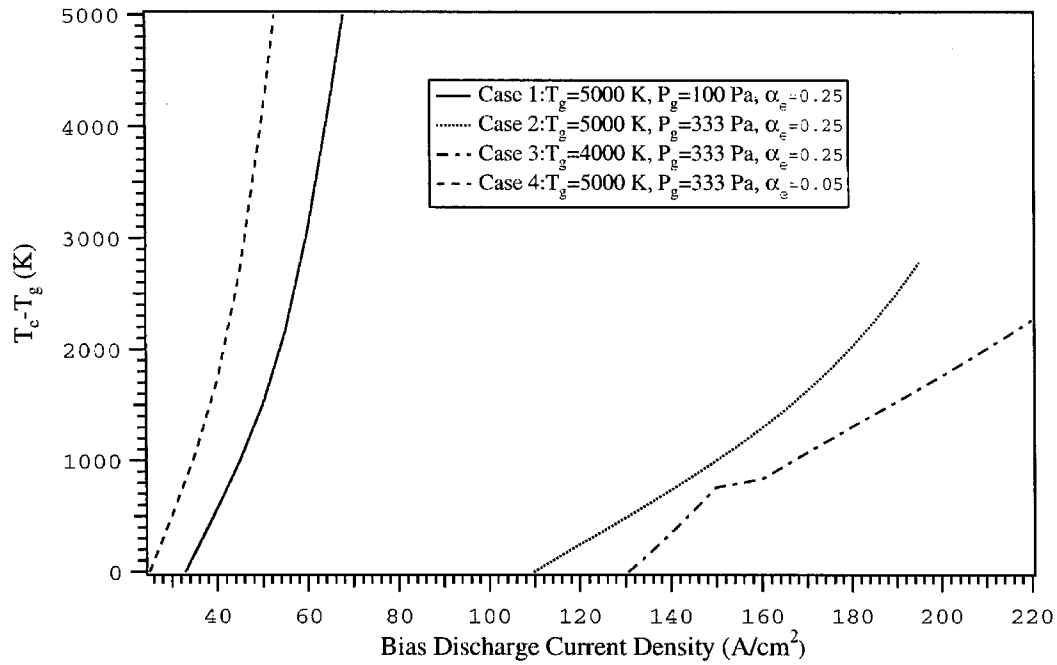

Figure 5.8: Electron temperature increase as a function of substrate bias current density

based on supply flowrates, before any dissociation or ionization has occurred). The volumetric flow ratio can then be related to the mass flow ratio through

$$f_m = \frac{\dot{m}_{CH_4}}{\dot{m}_{H_2^0}} = \frac{M_{CH_4}}{M_{H_2}} f_q \tag{5.24}$$

In solving for the mole fractions, the ratio of methane mass flow to the total mass flow is used and is given by

$$f = \frac{\dot{m}_{CH_4}}{\dot{m}_{tot}} = \frac{f_m}{1 + f_m} \tag{5.25}$$

Equations 5.21 - 5.25 are used to determine a consistent set of mole fractions and species densities which can be used in evaluation of Equation 5.11.

The results of solving Equation 5.11 for the four cases listed in Table 5.3 are shown in Figure 5.8. The solutions are seen to fall generally into two pairs of curves.

	CASE 1	CASE 2	CASE 3	CASE 4
$T\ (K)$	5000	5000	4000	5000
$P\ (Pa)$	100	333	333	333
α_d	0.9	0.9	0.9	0.9
α_e	0.25	0.25	0.25	0.05
f_q	0.01	0.01	0.01	0.01
$n_o\ (m^{-3})$	1.159 x 10^{21}	3.861 x 10^{21}	4.826 x 10^{21}	4.596 x 10^{21}
X_{CH_4}	0.0396	0.0396	0.0396	0.0569
X_{H_2}	0.0400	0.0400	0.0400	0.0471
X_H	0.5204	0.5204	0.5204	0.8007
X_{H+}	0.2000	0.2000	0.2000	0.0476
X_e	0.2000	0.2000	0.2000	0.0476

Table 5.3: Summary of composition sets assumed for electron heating calculations

Inspection of Equation 5.11 suggests a strong sensitivity to electron number density since it appears in the denominator of both Equation 5.11 and Equation 5.12 for the scalar conductivity. The two steeper curves at the lower current densities correspond to cases 1 and 4 and correspond to an electron number density of approximately 10^{20} m^{-3}. These two cases have the lowest number densities of electrons either because of the lower assumed stagnation pressure (100 Pa vs. 333 Pa) or because of the lower ionization fraction ($\alpha_e = 0.05$ vs. $\alpha_e = 0.25$). The higher electron density (approximately 10^{21} m^{-3}) for cases 2 and 3 result in higher conductivity and hence require higher current density for a given level of heating. The discontinuity seen in the curve for case 3 at a current density of 150 A/cm^2 is a result of the fact that one of the electron impact vibrational excitations of methane has a low energy threshold of approximately 0.41 eV. A general trend which was observed by Baldwin [95] is also evident here; the presence of molecules with excitable modes significantly increases the required current for effective electron heating. This is more clearly observed in Figure 5.9 where the results from Case 1 are plotted with different inelastic modes

suppressed.

The leftmost curve in Figure 5.9 is actually the two curves corresponding to all the hydrogen modes plus the methane momentum transfer. The addition of the methane momentum transfer collision rate does not produce any discernible difference in the curve. The two inner curves correspond to all the hydrogen collision terms plus the methane vibrational terms added alternately and the rightmost curve includes all terms. Each successive inelastic term considered increases the required current density. As a point of reference, if one considers the current required to raise the electron temperature by 4000 K, the addition of all the methane terms increases the required current density by approximately 12 A/cm^2. This is a significant amount if one considers the fact that a 10 cm substrate has a surface area of 78.5 cm^2 in which case just the difference due to the methane energy loss terms corresponds to an increase in the secondary discharge current by 942 A.

The results presented in Figures 5.8 and 5.9 indicate that although some level of free electrons is desirable to enable electron catalyzed chemistry, the levels of ionization one is likely to find in an MPD deposition reactor, even for the best case shown in Figure 5.8, is likely to require at least 50 A/cm^2 to elevate the electron temperature by 5000 K. This number is likely to increase significantly if more inelastic terms associated with all the species present were included. A current density of 50 A/cm^2 corresponds to a secondary discharge current of over 3900 A which is of the same order as the primary arc current. The conclusion from this analysis is therefore that the high ionization level (and low plasma resistivity) combined with inelastic losses through molecular collisions will make electron heating through a secondary discharge impractical.

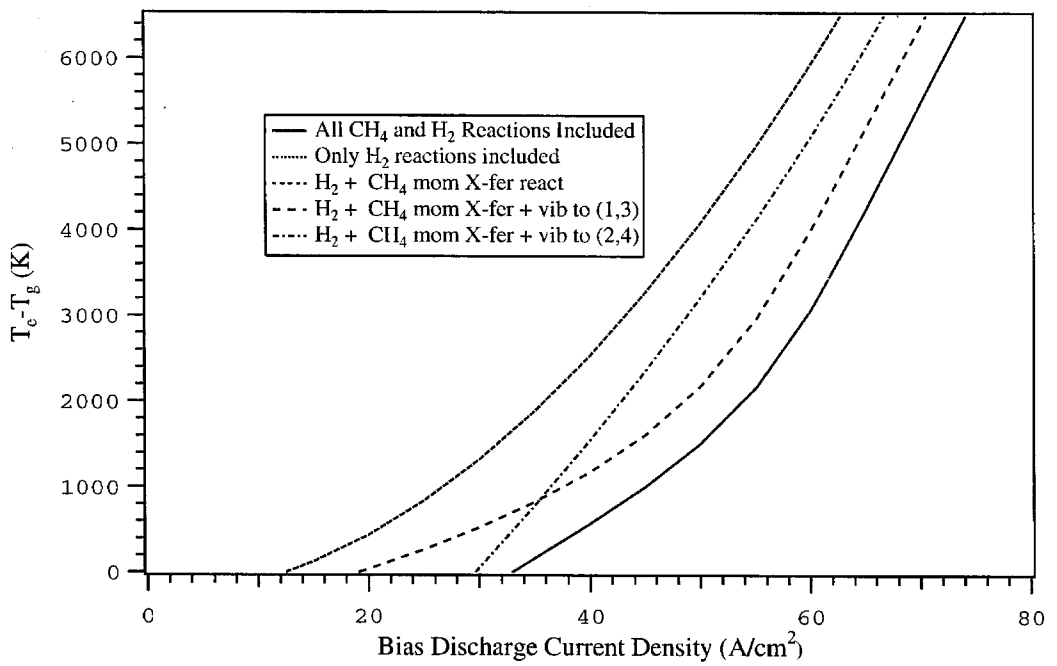

Figure 5.9: Electron temperature increase as a function of substrate bias current density with different inelastic mechanisms turned on or suppressed

5.3 Timescale for Methane Decomposition

In Chapter 4, some effects of different methane injector location were investigated experimentally. Location of the injector directly in the gas stream improves entrainment of the methane but creates a flow disruption which grows with time due to carbon deposition on the injection tube. Location of the injector at the plume boundary is preferable but introduces other challenges since the methane must effectively be entrained and diffuse in a very short time.

As described in Section 1.1, methyl has been identified as an important precursor for diamond deposition [2]. By investigating the time dependence of methane pyrolysis in the hydrogen stream, one can at least establish some bounds on the timescales available for effective mixing to occur such that transport of methyl to the substrate

Reaction	A (cm^3/mole sec)	n	E (cal/mole)
$H_2 - M \rightleftharpoons H + H + M$	2.23 x 10^{12}	0.5	92,536
$H_2 + e \rightleftharpoons H + H + e$	3.29 x 10^{13}	0.5	92,536
$H + e \rightleftharpoons H^+ + e - e$	1.51 x 10^{31}	-3.0	313,749

Table 5.4: Forward rate coefficients for hydrogen reactions from Ref. [101] for Arrhenius relation $k = AT^n exp(-E/RT)$

is maximized. The residence time to maximize the methyl mole fraction, and therefore transport to the substrate, is estimated in this section.

To investigate the decomposition of methane, the commercially available Chemkin software package for gas-phase chemical analysis was used along with the AURORA well-stirred reactor analysis program. This software was originally developed at Sandia National Laboratory and is currently marketed by Reaction Design Inc. The kinetic reaction set from the mechanism of Miller and Bowman [100] without nitrogen and oxygen chemistry was used. This was supplemented with additional hydrogen dissociation and ionization reactions from Kruger [101] including the two electron-hydrogen reactions listed in Table 5.4.

The two cases considered are listed in Table 5.5. The only difference between these two cases is the pressure. For Case 5 the pressure is again taken to be more representative of the value in the plume. Similarly, the pressure for Case 6 is more representative of the stagnation region. Another difference with the Cases 1 - 4 considered earlier is the diluent hydrogen flow is now assumed to be 100 percent dissociated. This is more representative of the lower pressure case where injection is assumed to occur near the MPD exit plane. Even at a temperature of 5000 K, recombination will likely have begun to occur at the point where the pressure has increased to 333 Pa. Case 6, with α_d =1.0 has been included for comparison of the

	CASE 5	CASE 6
$T\ (K)$	5000	5000
$P\ (Pa)$	100	333
α_d	1.0	1.0
α_e	0.25	0.25
f_q	0.01	0.01
$n_o\ (m^{-3})$	1.159 x 10^{21}	3.861 x 10^{21}
X_{CH_4}	0.0419	0.0419
X_{H_2}	0.0	0.0
X_H	0.5580	0.5580
X_{H+}	0.2000	0.2000
X_e	0.2000	0.2000

Table 5.5: Summary of composition sets assumed for methane decomposition calculations

decomposition rate with pressure.

The temperature value of 5000 K was selected because this is the upper limit of the thermodynamic property database for most of the species in the Chemkin thermodynamic library. Several of the species have an upper limit of 4000 K. This limitation prevents analysis at a more representative temperature of 10000 K in the plume or even higher in the stagnation region. Figure 5.10 shows two sets of curves with species mole fractions plotted both against log and linear time scales. The upper (linear) plot indicates that after approximately 10 μsec the mole fractions have almost reached their steady state values. Over this timescale there is no significant recombination of atomic hydrogen. One measure of an effective reactor design is its ability to maximize the delivery of methyl to the substrate. In the logarithmic plot, the time variation of species concentration are more easily seen. The concentration of CH_3 is seen to reach a maximum at approximately 3 μsec after which it begins to drop. A good reactor design would match the injector location and jet characteristics

so that this maximum occurs at the substrate. For a jet velocity of 25 km/sec, a residence time of 3μsec implies a length scale of 7.5 cm.

In Figure 5.11 a subset of the entire species set in Figure 5.10 is shown comparing concentration histories at 100 Pa and 333 Pa. For the higher pressure data the atomic hydrogen fraction actually increases slightly. This is a result of the reactions in Table 5.4 in which the rate of recombination of the hydrogen ion is producing neutral atomic hydrogen faster than the molecular hydrogen recombination is consuming it. Examining the methyl mole fraction history, the increase in pressure is seen to shorten the time to reach the maximum to 1μsec. Again considering a jet velocity of 25 km/sec, the characteristic length for optimal methyl delivery is approximately 2.5 cm. The time to maximize methyl concentration calculated in this section are only bounding values because they have been calculated at a temperature of 5000 K. At a temperature of 10000 K the decomposition will proceed more rapidly.

The residence time of 1 - 3 μsec does not account for the time required for the methane to diffuse into the 5 - 10 cm diameter jet. An estimate of the timescale τ for the methane with a diffusion coefficient D_{CH_4} to diffuse a distance l_d into the hydrogen can be obtained from the approximate expression [89]

$$\tau \approx \frac{l_d^2}{D_{CH_4}} \tag{5.26}$$

At 100 Pa and 4000 K (the upper limit of the Chemkin transport database), the diffusion coefficient D_{CH_4} of a dilute mixture of methane into atomic hydrogen is 899 cm^2/sec. Using the above expression, one obtains an estimate of 28 msec to diffuse 5 cm. The disparity between this estimate and the 3 μsec to maximize the methyl mole fraction underscores the difficulty in post-accelerator injection of the methane into a relatively large diameter jet.

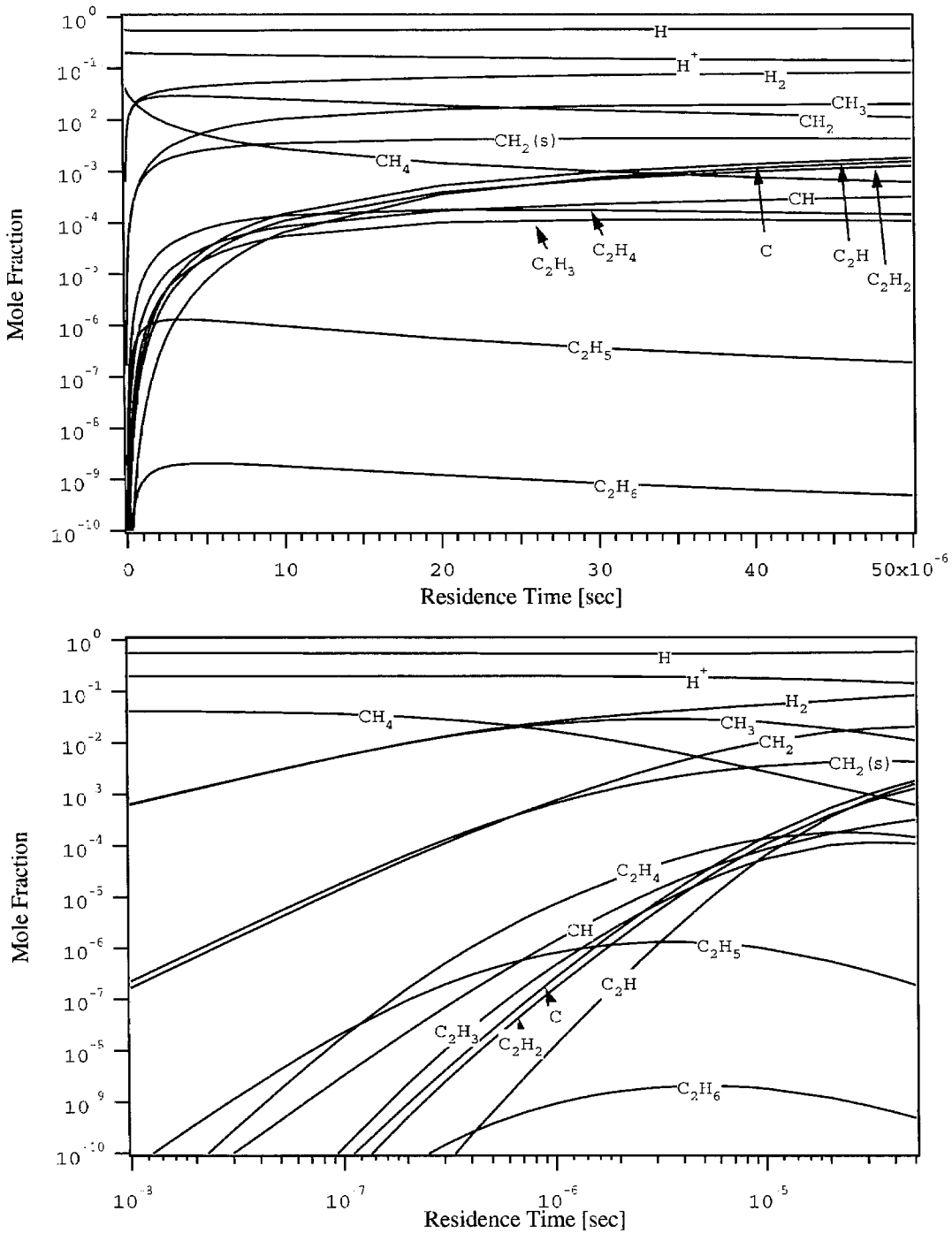

Figure 5.10: Composition of hydrogen-methane mixture at 5000 K and 100 Pa as a function of residence time in the plume

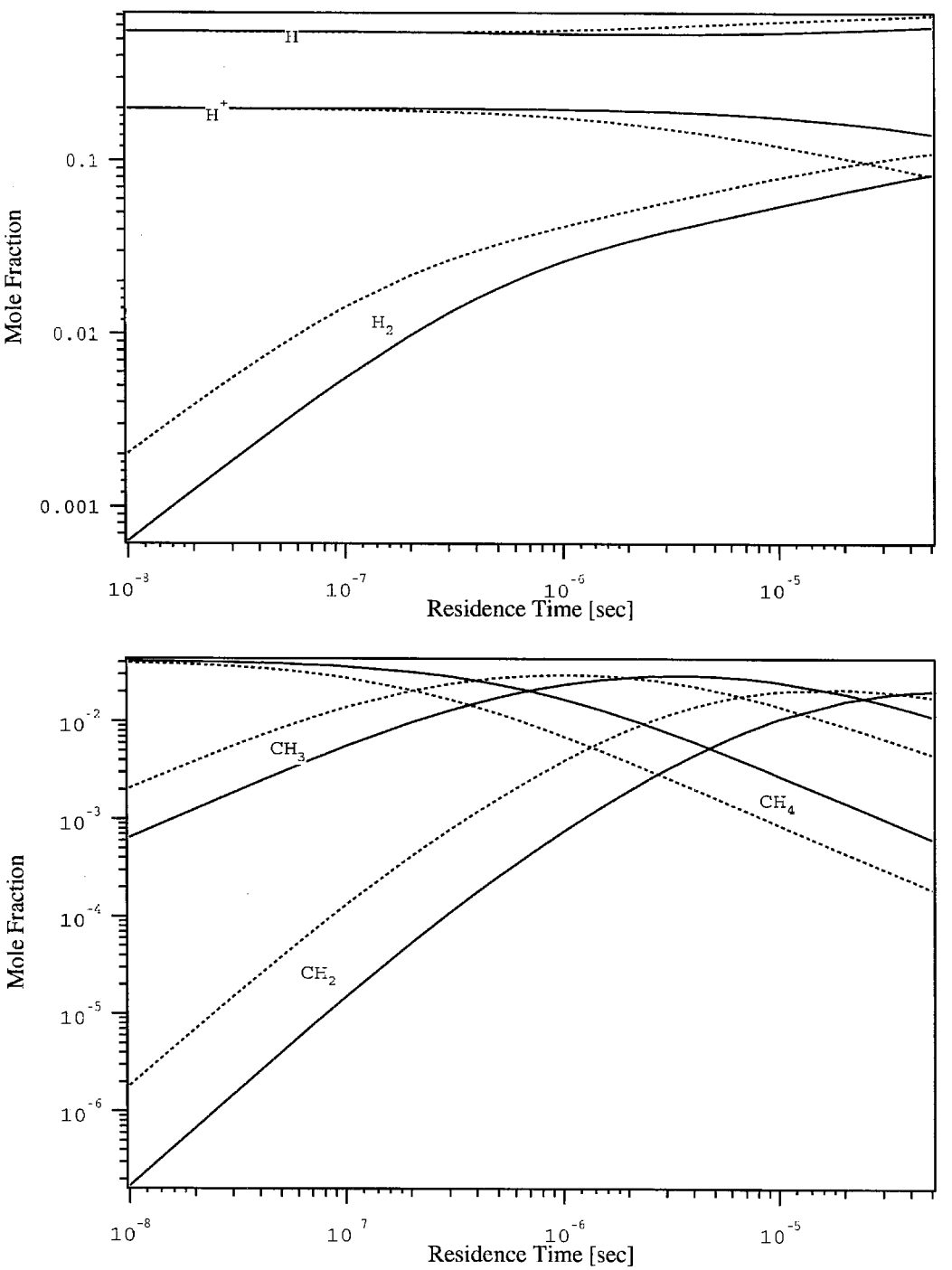

Figure 5.11: Mole fractions of select species at 5000 K at pressures of 100 Pa (solid line) and 333 Pa (dashed line) as a function of residence time in the plume

Chapter 6

Summary and Recommendations for Future Work

6.1 Summary

The work in this thesis has focused on two major areas; one involving the use of diamond film to benefit electric thrusters subject to sputter erosion, the second involving the use of an electromagnetic thruster as a means of improving growth rates of diamond. The first area was a result of an ongoing effort within NASA to find ways to maximize the lifetime of electric thruster components subject to life-limiting sputter erosion from ion bombardment. The electrodes used in electrostatic ion thrusters to focus and accelerate a beam of xenon ions to velocities in excess of 30 km/sec are subject to such erosion, making them one of mission life-limiting technologies on these systems. Current ion optics are made of molybdenum, and the next generation will use grids made from a carbon-carbon composite. Diamond has a number of desirable properties relevant to their use for ion optics including a high thermal conductivity, a

coefficient of thermal expansion lower than molybdenum, and a controllable (through doping levels) electrical conductivity.

Two approaches for utilizing some of these desirable properties in ion grid fabrication were described. These are deposition of diamond coatings on a molybdenum grid or deposition, and subsequent machining, of a free standing film to serve as the grid. The primary reason for using diamond in the first place was to minimize erosion; therefore, the sputter yields of diamond film had to be measured. The combined experimental and analytical determination of the absolute sputter yield subject to xenon ion bombardment at energies of 150 - 750 eV are described in Chapter 2. In this energy range, it is found that diamond should provide a factor of 7 - 12 reduction in erosion rate over molybdenum and at least a factor of 1.5 over carbon-carbon.

With the erosion rates established, the focus of this work then shifted to the evaluation of a potential technique for obtaining higher growth rates over larger areas of interest to industrial producers of diamond. Arcjets have been used extensively for commercial production of diamond films. The work of Loh and Cappelli in particular identified the benefits of a low pressure, supersonic plasma jet as a gas activation source for diamond CVD. Many of the same attributes pertain to the MPD accelerator, with some additional benefits possible due to the ease of scaling, higher jet velocity, and higher levels of ionization and dissociation. In particular, electrothermal thrusters are limited by material temperature limits, which bound the stagnation temperature, to velocities of 10 - 15 km/sec. With electromagnetic accelerators on the other hand, high jet velocities in excess of 20 km/sec are readily attainable by operating at high currents and low mass flowrates (up to the onset limit). Answering the question of whether these MPD characteristics would in fact be advantageous in a diamond deposition application was the goal of the remaining effort.

An experimental facility designed for high current cathode research was used in a series of experiments using an MPD plasma for diamond CVD. Because the source used was designed for good optical access rather than high jet velocity, the process conditions produced were more representative of the high temperature, ionization, and dissociation levels one would expect from an MPD in an actual reactor without the high velocity. Numerous trials were conducted using methane to hydrogen ratios of 1.5 - 3.5 percent, four different methane injector configurations, and substrate biasing at potentials of 25 - 75 V positive with respect to facility ground. These tests were performed at discharge currents of 700 - 950 A and approximately 18 V (12 - 17 kW).

For mixture ratios less than 1.5 percent only limited crystallites were deposited with no continuous film. Amorphous carbon deposits were observed on parts of substrate closest to the injector tube suggesting large methane concentration gradients and poor mixing of methane into gas stream. Several of the runs produced continuous film of a few square millimeters in size. The orientation of substrate in the chamber may have resulted in some loss of film upon cool down as evidenced by regions where the film had clearly separated from the molybdenum substrate and been lost. The plume core was observed to not be colinear with the chamber axis resulting in nonuniform heat flux to the substrate. This fact, and the limited number of thermocouples on the back side of the 7 cm diameter substrate, contributed to a large uncertainty in the deposition temperature.

The film morphology was crystalline with predominantly (111) oriented facets. The X-ray diffraction spectra for each of the samples presented indicates at least one unambiguous diamond peak with other peaks due to metals or metallic carbides present in most of the cases. Growth rates of 0.8 to 6.3 μm/hr were measured. The

films all exhibited poor Raman spectra with a broad background and no well defined peak at 1332 cm^{-1}. There are several possible explanations for the poor Raman spectra including the presence of background levels of nitrogen over 900 PPM along with defects along grain and twin boundaries. Contamination from impurities such as tungsten carbide and molybdenum carbide as indicated by XRD are another possibility. These contaminants are a consequence of metal vapor from the thermionic cathode, which operates at close to the melting point of tungsten, and the molybdenum injector tube.

In addition to the tests with the grounded substrate, six tests were performed with the substrate biased positive with respect to ground at 50 - 75 V. No films were deposited for any of these cases and only a limited coverage with crystallites observed after one of the tests. Positive biasing has been proposed as a means for energy addition to the free electrons in the sheath, enhancing the dissociation of hydrogen through collisional processes. Since a hydrogen ion will require a velocity of approximately 69 km/sec to overcome the potential barrier due to a positive bias of even 25 V, its likely the biasing in these tests, where most of the hydrogen may have been in the form of ions, was inhibiting any appreciable flux of hydrogen to the surface.

Summarizing the conclusions from the deposition experiments: 1) Methane injection can be problematic. This becomes a trade between carbon build-up on the injector (with possible flow obstruction) versus poor entrainment and mixing. 2) Cathode erosion products will be present and likely affect film quality. 3) If too large a fraction of the arriving atomic hydrogen is ionized, positive biasing may impede rather than enhance overall hydrogen flux.

In Chapter 5, the question of high velocity and high ionization level was investi-

gated analytically. Because very little plume data is available for MPDs operating on hydrogen, the experimental and analytical work of Tahara was reviewed to establish some bounds on expected plume characteristics. Because his calculations assume thermal and chemical equilibrium, this data was only used to get upper bounds on velocity and heavy particle gas temperature. For conditions expected with an MPD, Knudsen numbers in the plume are calculated to be approximately 0.1 in the free stream and 0.002 - 0.05 (i.e., transition-continuum boundary) in the stagnation boundary layer. Static heavy particle temperatures in plume are expected to be on the order of 10000 K in the core. For Mach numbers in the range 1 - 1.5, the stagnation temperature can be expected to reach peak values of over 20000 K. This temperature far exceeds range of available thermodynamic and transport databases for hydrocarbon mixtures needed to model stagnation boundary layer chemistry and growth rates so a scaling relation developed by Goodwin was used to compare the relative levels of atomic hydrogen at the substrate for an electrothermal and electromagnetic source. Because of the high velocities and lower pressures, the electromagnetic source operates in more of a convection-dominated regime. As a result, the hydrogen mole fraction was estimated to increase by approximately 40 percent over that of an electrothermal accelerator.

In order to estimate the level of electron heating obtainable for a given bias current density, a simplified form of the electron energy equation was used to define an energy balance. This estimate for the electron heating is an upper (best case) bound since many loss mechanisms are not considered which will only drive the electron temperature down. Results showed that, even for pressures of a few Torr and ionization fractions of 5 - 25 percent, the required current, for a few thousand degree increase in electron temperature over gas temperature, was on the order of several

tens of A/cm^2. For a 10 cm substrate this implies currents which are a significant fraction of the primary arc current and therefore not practical to implement.

Estimates were made of the optimal residence time of the methane in the plume in order to maximize the methyl flux to the substrate. Again, due to limits on the fits in the thermodynamic database, these were performed at 5000 K and pressures of 100 Pa and 333 Pa, approximating the pressure in the plume and stagnation region respectively. At these temperatures and pressures, there is little recombination of the hydrogen and the methyl mole fraction reaches a maximum at 1 - 3 μsec. For a jet velocity of 25 km/sec, this residence time implies a length scale of 2.5 - 7.5 cm. Given the microsecond timescales for optimal chemistry, the time available for diffusion and entrainment of the methane into a 10 cm diameter jet is likely to be insufficient and will minimize any advantage to be gained from the larger plume cross section associated with the MPD sources.

6.2 Recommendations for Future Work

Given the disadvantages of the MPD source with respect to 1) contamination of the film due to metal vapor from the high current electrodes and 2) poor entrainment of the carbon precursor gas due to the short residence time in the plume, it is concluded that the potential advantages over more conventional plasma sources with respect to higher growth rates is not significant enough to warrant further investigation at this time.

The low sputter yield of diamond has opened a new potential application in the coating of electric thruster components subject to xenon ion bombardment. This reduction in the erosion rate makes coating of grid electrodes with CVD diamond an

attractive option for extending the lifetime of ion thrusters and should be explored further. A logical next step towards this application would be the coating of an ion thruster grid or Hall thruster insulator with subsequent long duration testing. For components which must operate for thousands of hours, this application is likely to require doped films several hundred microns thick for any free standing structures and possibly for coatings as well. For an ion thruster grid, which is approximately 30 cm in diameter, different coating sources suitable for large area deposition, such as microwave and combustion reactors, should be evaluated. The best option will result in coatings which are of high quality and uniformity over both the webbing between, and along the inner surfaces of, the holes. The coated grids can then be evaluated through suitable accelerated wear tests to assess performance.

Appendix A

Goodwin Scaling Relation for Atomic Hydrogen Transport

In deriving the relation for atomic hydrogen transport, Goodwin [89] assumes the diffusion of atomic hydrogen to the substrate (resulting in a flux Γ_H) is balanced by the rate at which atomic hydrogen is lost from the gas phase due to surface recombination

$$\Gamma_H = n_o D_H \left(\frac{dX_H}{dz}\right)_o = \gamma_H n_o X_{H_o} \frac{\bar{c}_H}{4} \tag{A.1}$$

where D_H is the diffusion coefficient of a dilute mixture of atomic hydrogen through molecular hydrogen, γ_H is the recombination coefficient of atomic hydrogen at the substrate surface, n_o is the molar gas density at the surface, X_{H_o} is the hydrogen mole fraction at the surface, and $\bar{c}_H$ is the atomic hydrogen thermal velocity. The concentration gradient is expressed with respect to the z coordinate which is normal to the substrate surface. The concentration gradient dX_H/dz is approximated as the difference between the mole fraction at the surface X_{H_o} and the free stream X_{H_∞}

divided by the concentration boundary layer thickness, δ_H, which is a characteristic length scale for diffusion

$$\left(\frac{dX_H}{dz}\right)_o \approx \frac{X_{H_\infty} - X_{H_o}}{\delta_H} \tag{A.2}$$

With these approximations, the ratio of the atomic hydrogen mole fraction at the surface, to that in the free stream outside the concentration boundary layer, can be expressed in terms of nondimensional parameters as

$$\frac{X_{H_o}}{X_{H_\infty}} = \left(1 + \frac{\gamma_H}{Kn_\delta}\right)^{-1} \tag{A.3}$$

where the Knudsen number Kn_δ is defined in terms of the atomic hydrogen mean free path λ_H and concentration boundary layer thickness

$$Kn_\delta = \frac{\lambda_H}{\delta_H} \approx \frac{4D_H}{\bar{c}_H \delta_H} \tag{A.4}$$

The approximate equality in Equation A.4 results from using a simple expression from kinetic theory [93] ($D_H = \frac{1}{3}\bar{c}_H \lambda_H$) to relate the diffusion coefficient to the mean free path. Goodwin uses an analytical expression for the concentration boundary layer thickness obtained following the analysis in Kays and Crawford [102] for an axisymmetric stagnation point flow

$$\delta_H \approx 1.32 \left(\frac{\nu}{a}\right)^{0.5} \left(\frac{D_H}{\nu}\right)^{0.4} \tag{A.5}$$

where ν is the kinematic viscosity and a is the velocity gradient parameter.

Using kinetic theory to express the diffusion coefficient and viscosity in terms of the pressure, and an experimentally measured value for the recombination coefficient [89] ($\gamma_H \approx 0.1$ at 1200 K), Equations A.3 - A.5 can be combined to obtain an expression

for the ratio of the atomic hydrogen mole fraction at the surface X_{H_o} to that in the free stream X_{H_∞} which scales with the pressure p in the stagnation region and the velocity gradient parameter a

$$\frac{X_{H_o}}{X_{H_\infty}} = \left(1 + 110\sqrt{\frac{p}{a}}\right)^{-1} \tag{A.6}$$

where p has units of Torr and a has units of $\sec^{-1}$.

Bibliography

[1] K.E. Spear. Diamond-Ceramic Coating of the Future. *Journal of the American Ceramic Society*, 72(2):171–191, 1989.

[2] D.G. Goodwin. Scaling Laws for Diamond Chemical Vapor Deposition. I. Diamond Surface Chemistry. *Journal of Applied Physics*, 74(11):6888–6894, 1993.

[3] M.E. Coltrin and D.S. Dandy. Analysis of Diamond Growth in Subatmospheric DC Plasma-Gun Reactors. *Journal of Applied Physics*, 74(9):5083–5820, 1993.

[4] D.S. Dandy and M.E. Coltrin. A Simplified Analytical Model of Diamond Growth in Direct Current Arcjet Reactors. *Journal of Materials Research*, 10(8):1993–2010, 1995.

[5] P.K. Bachmann and W. van Enckevort. Diamond Deposition Technologies. *Diamond and Related Materials*, 1:1021–1034, 1992.

[6] J.M. Monheiser and P.J. Wilbur. An Experimental Study of Impingement Ion Production Mechanisms. In 28^{th} *Joint Propulsion Conference*, Nashville, TN, July 6-8, 1992. AIAA 92-3826.

[7] J.R. Brophy, J.E. Polk, and L.C. Pless. Test-to-Failure of a Two-Grid, 30-cm. Diameter Ion Accelerator System. In 23^{rd} *International Electric Propulsion Conference*, Seattle, WA, September 1993. IEPC-93-172.

[8] X. Peng, D. Keefer, and W. Ruyten. Plasma Particle Simulation of Electrostatic Ion Thrusters. In 21^{st} *International Electric Propulsion Conference*, Orlando, FL, July 18-20, 1990. AIAA 90-2647.

[9] X. Peng and W. Ruyten. Further Study of the Downstream Plasma Condition on Accelerator Grid Erosion in an Ion Thruster. In 28^{th} *Joint Propulsion Conference*, Nashville, TN, July 6-8, 1992. AIAA 92-3829.

[10] X. Peng and W. Ruyten. Charge Exchange Grid Erosion Study for Ground-Based and Space-Based Operations of Ion Thrusters. In 23^{rd} *International Electric Propulsion Conference*, Seattle, WA, September 13-16, 1993. IEPC-93-173.

[11] D. Rosenberg and G.K. Wehner. Sputtering Yields for Low Energy He, Kr, and Xe Ion Bombardment. *Journal of Applied Physics*, 33(5):1842–1845, 1962.

[12] C.H. Weijsenfeld, A. Hoogendoorn, and M. Koedam. Sputtering of Polycrystalline Metals by Inert Gas Ions of Low Energy (100 - 1000 eV). *Physica*, 27:763–764, 1961.

[13] C.E. Garner and J.R. Brophy. Fabrication and Testing of Carbon-Carbon Grids for Ion Optics. In 28^{th} *Joint Propulsion Conference*, Nashville TN, July 6-8, 1992. AIAA 92-3149.

[14] J.F. Prins. Bipolar Transistor Action in Ion Implanted Diamond. *Applied Physics Letters*, 41(10):950–952, 1982.

[15] R.F. Davis, editor. *Diamond Films and Coatings, Chapter 8, Electronic Applications of Diamond Films and Coatings.* Noyes Publications, Park Ridge, NJ, 1993.

[16] M.W. Geis. Diamond Transistor Performance and Fabrication. *Proceedings of The IEEE*, 79(5):669–675, 1991.

[17] R.C. Weast and M.J. Astle, editors. *CRC Handbook of Chemistry and Physics, 60th Edition.* CRC Press, Boca Raton, FL, 1981.

[18] G. Popovici and M.A. Prelas. Nucleation and Selective Deposition of Diamond Thin-Films. *Physica Status Solidi A-Applied Research*, 132(2):233–252, 1992.

[19] R.F. Davis, editor. *Diamond Films and Coatings; Development, Properties, and Applications.* Noyes Publications, Park Ridge, NJ, 1993.

[20] W. Zhu, B.R. Stoner, B.E. Williams, and J. T. Glass. Growth and Characterization of Diamond Films on Non-Diamond Substrates for Electronic Applications. *Proceedings of The IEEE*, 79(5):621–646, 1991.

[21] M.N.R. Ashfold, P.W. May, C.A. Rego, and N.M. Everitt. Thin-Film Diamond by Chemical-Vapor-Deposition Methods. *Chemical Society Reviews*, 23(1):21–30, 1994.

[22] J.J. Blandino, D.G. Goodwin, C.E. Garner, and J.R. Brophy. Evaluation and Development of Diamond Grids for Ion Optics. In *31st Joint Propulsion Conference*, San Diego, CA, July 10-12, 1995. AIAA 95-2663.

[23] T.J. Whetten, A.A. Armstead, T.A. Grzybowski, and A.L. Ruoff. Etching of Diamond with Argon and Oxygen Ion- Beams. *Journal of Vacuum Science and Technology A-Vacuum Surfaces and Films*, 2(2):477–480, 1984.

[24] I. Miyamoto and N. Taniguchi. Polishing and Sharpening of Diamond Point Tools by Ion Sputter-Machining. *Precision Engineering-Journal of The American Society for Precision Engineering*, 4(4):191–194, 1982.

[25] A. Hirata, H. Tokura, and M. Yoshikawa. Smoothing of Chemically Vapor-Deposited Diamond Films by Ion-Beam Irradiation. *Thin Solid Films*, 212(1-2):43–48, 1992.

[26] K. Kobayashi, K. Yamamoto, N. Mutsukura, and Y. Machi. Sputtering Characteristics of Diamond and Hydrogenated Amorphous-Carbon Films by RF Plasma. *Thin Solid Films*, 185(1):71–78, 1990.

[27] J. Ullmann, A. Delan, and G. Schmidt. Ion Etching Behavior and Surface Binding-Energies of Hard Diamond-Like Carbon and Microwave Chemical-Vapor-Deposition Diamond Films. *Diamond and Related Materials*, 2(2-4):266–271, 1993.

[28] A. Hoffman, S. Prawer, and R. Kalish. Structural Transformation of Diamond Induced by 1- KeV Ar-Ion Irradiation as Studied by Auger and Secondary-Electron Spectroscopies and Total- Secondary-Electron-Yield Measurements. *Physical Review B-Condensed Matter*, 45(22):12736–12745, 1992.

[29] J. Ullmann, A. Weber, B. Mainz, J. Stiegler, and T. Schuhrke. Low-Energy Ion-Induced Damage of Polycrystalline Diamond Films. *Diamond and Related Materials*, 3(4-6):663–671, 1994.

[30] A. Joshi and R. Nimmagadda. Erosion of Diamond Films and Graphite in Oxygen Plasma. *Journal of Materials Research*, 6(7):1484–1490, 1991.

[31] O. Dorsch, M. Werner, and E. Obermeier. Dry-Etching of Undoped and Boron-Doped Polycrystalline Diamond Films. *Diamond and Related Materials*, 4(4):456–459, 1995.

[32] G.S. Sandhu and W.K. Chu. Reactive Ion Etching of Diamond. *Applied Physics Letters*, 55(5):437–438, 1989.

[33] N.N. Efremow, M.W. Geis, D.C. Flanders, G. A. Lincoln, and N.P. Economou. Ion Beam Assisted Etching of Diamond. *Journal of Vacuum Science Technology*, 3(1):416–418, 1985.

[34] C.E. Garner, J.R. Brophy, Pless L.C., and J.W. Barnett. The Effect of Nitrogen on Xenon Ion Engine Erosion. In 21^{st} *International Electric Propulsion Conference*, Orlando, FL, July 18-20, 1990. AIAA 90-2591.

[35] H.D. Hagstrum. Effect of Monolayer Adsorption on the Ejection of Electrons from Metals by Ions. *Physical Review*, 104(6):1516–1527, 1956.

[36] J.K. Kim, H. Kheyrandish, and J.S. Colligon. Influence of Charge-Exchange on Ion-Neutral Arrival Rates in an Ion-Assisted Deposition System. *Journal of Vacuum Science and Technology A-Vacuum Surfaces And Films*, 12(5):2733–2738, 1994.

[37] R. Samanta Roy. *Numerical Simulation of Ion Thruster Plume Backflow for Spacecraft Contamination Assessment.* PhD thesis, MIT, 1995.

[38] J. Mueller, J.R. Brophy, and D.K. Brown. Endurance Testing and Fabrication of Advanced 15-cm and 30-cm Carbon-Carbon Composite Grids. In *31st Joint Propulsion Conference*, San Diego, CA, July 10-12, 1995. AIAA 95-2660.

[39] R. Behrisch, editor. *Sputtering by Particle Bombardment I; Physical Sputtering of Single-Element Solids.* Springer-Verlag, Berlin Heidelberg, 1981.

[40] R.G. Jahn. *Physics of Electric Propulsion.* McGraw-Hill Book Co., New York, NY, 1968.

[41] K. Kurihara, K. Sasaki, M. Kawarada, and N. Koshino. High-Rate Synthesis of Diamond by DC Plasma-Jet Chemical Vapor-Deposition. *Applied Physics Letters*, 52(6):437–438, 1988.

[42] R. Furukawa, H. Uyama, and O. Matsumoto. Diamond Deposition with Plasma-Jet at Reduced Pressure. *IEEE Transactions on Plasma Science*, 18(6):930–933, 1990.

[43] M.H. Loh and M.A. Cappelli. Supersonic DC-Arcjet Plasma at Subtorr Pressures as a Medium for Diamond Film Synthesis. In 28^{th} *Joint Propulsion Conference*, Nashville, TN, July 6-8, 1992. AIAA 92-3534.

[44] M.H. Loh and M.A. Cappelli. Supersonic DC-Arcjet Synthesis af Diamond. *Diamond and Related Materials*, 2(2-4):454–461, 1993.

[45] S. Matsumoto, Y. Manabe, and Y. Hibino. Diamond Deposition Using an X-Y Stage in a DC Plasma-Jet Chemical Vapor-Deposition. *Journal of Materials Science*, 27(21):5905 5910, 1992.

[46] A. Hirata and M. Yoshikawa. Enlargement of the Diamond Deposition Area by One- Cathode 3-Anode Arc-Discharge Plasma-Jet Chemical- Vapor-Deposition. *Diamond and Related Materials*, 2(11):1402–1408, 1993.

[47] A. Hirata and M. Yoshikawa. Effects of Electrode Arrangement and Pressure on Synthesis of Diamond Films by Arc Discharge Plasma Jet Chemical Vapor Deposition. *Diamond and Related Materials*, 4(12):1363–1370, 1995.

[48] F.X. Lu, G.F. Zhong, J.G. Sun, Y.L. Fu, W.Z. Tang, J.J. Wang, G.H. Li, J.M. Zang, C.H. Pan, C.X. Tang, T.L. Lo, and Y.G. Zhang. A New Type of DC Arc Plasma Torch for Low Cost Large Area Diamond Deposition. *Diamond and Related Materials*, 7(6):737–741, 1998.

[49] F. Akatsuka, Y. Hirose, and K. Komaki. Rapid Growth of Diamond Films by Arc-Discharge Plasma CVD. *Japanese Journal of Applied Physics Part 2-Letters*, 27(9):L1600–L1602, 1988.

[50] N. Ohtake and M. Yoshikawa. Diamond Film Preparation by Arc-Discharge Plasma- Jet Chemical Vapor-Deposition in the Methane Atmosphere. *Journal of The Electrochemical Society*, 137(2):717–722, 1990.

[51] K.A. Snail, C.M. Marks, Z.P. Lu, J. Heberlein, and E. Pfender. High-Temperature, High-Rate Homoepitaxial Synthesis of Diamond in a Thermal Plasma Reactor. *Materials Letters*, 12(5):301–305, 1991.

[52] J. Karner, M. Pedrazzini, and C. Hollenstein. High Current DC Arc (HCDCA) Technique for Diamond Deposition. *Diamond and Related Materials*, 5(3-5):217–220, 1996.

[53] K. Itoh, N. Horii, and O. Matsumoto. Effect of Chlorine Species on Diamond Deposition from Plasma Jets with Chlorobenzenes as Carbon Sources. *Journal of the Electrochemical Society*, 145(8):2895–2900, 1998.

[54] N. Horii, N. Suzuki, K. Itoh, T. Kotaki, and O. Matsumoto. Deposition of Diamond from Plasma Jets with Chlorobenzenes as Carbon Source. *Diamond and Related Materials*, 6(12):1874–1882, 1997.

[55] T. Kotaki, N. Horii, H. Isono, and O. Matsumoto. Deposition of Diamond from a Plasma Jet with Dichlorobenzene as Carbon Source. *Journal of the Electrochemical Society*, 143(6):2003–2010, 1996.

[56] T. Kotaki, Y. Amada, K. Harada, H. Uyama, and O. Matsumoto. Diamond Deposition from an Ar-CCl4-H2 Plasma-Jet at 13.3 kPa. *Diamond and Related Materials*, 2(2-4):342–346, 1993.

[57] Q.Y. Han, T.W. Or, Z.P. Lu, J. Heberlein, and E. Pfender. High Rate Deposition of Diamond Using Liquid Organic Precursors in Atmospheric Plasmas. In *Proceedings of the Second International Symposium on Diamond Materials*, volume 93-17, pages 115–122, Washington, DC, May 5-10, 1991.

[58] N. Ohtake and M. Yoshikawa. Effects of Oxygen Addition on Growth of Diamond Film by Arc-Discharge Plasma-Jet Chemical-Vapor- Deposition. *Japanese Journal of Applied Physics Part 1-Regular Papers, Short Notes and Review Papers*, 32(5A):2067–2073, 1993.

[59] K. Kurihara, K. Sasaki, and M. Kawarada. Diamond-Film Synthesis Using DC Plasma-Jet CVD. *Fujitsu Scientific and Technical Journal*, 25(1):44–51, 1989.

[60] K.R. Stalder and R.L. Sharpless. Plasma Properties of a Hydrocarbon Arcjet Used in the Plasma Deposition of Diamond Thin-Films. *Journal of Applied Physics*, 68(12):6187–6190, 1990.

[61] I.A. Martorell, W.D. Partlow, R.M. Young, J.J. Schreurs, and H.E. Saunders. Gas Recycling and Flow Control for Cost Reduction of Diamond Films Deposited by DC Arc-Jet. *Diamond and Related Materials*, 8(1):29–36, 1999.

[62] S. Matsumoto, I. Hosoya, and T. Chounan. Substrate Bias Effect on Diamond Deposition by DC Plasma-Jet. *Japanese Journal of Applied Physics Part 1-Regular Papers, Short Notes and Review Papers*, 29(10):2082–2086, 1990.

[63] M. Kawarada, K. Kurihara, and K. Sasaki. Diamond Synthesis on a Metal-Substrate. *Diamond and Related Materials*, 2(5-7):1083–1089, 1993.

[64] S.K. Baldwin, T.G. Owano, M. Zhao, and C.H. Kruger. Enhanced Deposition Rate of Diamond in Atmospheric Pressure Plasma CVD: Effects of a Secondary Discharge. *Diamond and Related Materials*, 6:202–206, 1997.

[65] W.Z. Tang, G.F. Zhong, F.Z. Shen, and F.X. Lu. Input Power Dependence of Growth Rate and Quality of Diamond Films Deposited in a DC Arcjet System. *Diamond and Related Materials*, 8(2-5):211–214, 1999.

[66] G.F. Zhong, F.Z. Shen, F.X. Lu, and W.Z. Tang. Preparation and Characterization of High Quality Diamond Films by DC Arc Plasma Jet CVD Method. *Journal of University of Science and Technology Beijing*, 6(4):281–284, 1999.

[67] S.W. Reeve, W.A. Weimer, and D.S. Dandy. Diamond Growth Using Remote Methane Injection in a Direct-Current Arcjet Chemical-Vapor-Deposition Reactor. *Applied Physics Letters*, 63(18):2487–2489, 1993.

[68] A.C. Ducati, G.M. Giannini, and E. Muehlberger. Experimental Results in High Specific Impulse Thermoionic Acceleration. *AIAA Journal*, 2(8):1452–1454, 1964.

[69] W.D. Merke, M. Auweter-Kurtz, H. Habiger, H. Kurtz, and H.O. Schrade. Nozzle Type MPD Thruster Experimental Investigations. In 20^{th} *DGLR/AIAA/JSASS International Electric Propulsion Conference*, Garmisch-Partenkirchen, W. Germany, October 3-6, 1988. AIAA 88-028.

[70] T. Yoshikawa and Y. Kagaya. Thrust and Efficiency of New K-III MPD Thruster. In 16^{th} *AIAA/JSASS/DGLR International Electric Propulsion Conference*, New Orleans, LA, November 17-19, 1982. AIAA 82-1887.

[71] E. Choueiri. Scaling of Thrust in Self-Field Magnetoplasmadynamic Thrusters. *Journal of Propulsion and Power*, 14(5):744–753, 1998.

[72] T. Yoshikawa, Y. Kagaya, and H. Tahara. Thrust Measurement of a Quasi-Steady MPD Arcject. In 18^{th} *AIAA/DGLR/JSASS International Electric Propulsion Conference*, Alexandria, VA, September 30 - October 2, 1985. AIAA 85-2003.

[73] Y. Kagaya, Y. Yokoi, H. Tahara, and T. Yoshikawa. Thrust Performance and Current Distribution in a Quasi-Steady MPD Arcjet. In 17^{th} *JSASS/AIAA/DGLR International Electric Propulsion Conference*, Tokyo, Japan, May 1984. AIAA 84-31.

[74] K. Toki, Y. Shimizu, and K. Kuriki. Hollow Cathode MPD Thruster. In 18^{th} *AIAA/DGLR/JSASS International Electric Propulsion Conference*, Alexandria, VA, September 30 - October 2, 1985. AIAA 85-2057.

[75] H. Tahara, Y. Kagaya, and T. Yoshikawa. Quasi-Steady MPD Arcjets with Applied Magnetic Fields. In 18^{th} *AIAA/DGLR/JSASS International Electric Propulsion Conference*, Alexandria, VA, September 30 - October 2, 1985. AIAA 85-2001.

[76] H. Tahara, H. Yasui, Y. Kagaya, and T. Yoshikawa. Development of a Quasi-Steady MPD Arcjet Thruster for Near-Earth Missions. In 19^{th} *AIAA/DGLR/JSASS International Electric Propulsion Conference*, Colorado Springs, CO, May 11-13, 1987. AIAA 87-1001.

[77] H. Tahara, H. Yasui, Y. Kagaya, and T. Yoshikawa. Experimental and Theoretical Researches on Arc Structure in a Self-Field Thruster. In 19^{th} *AIAA/DGLR/JSASS International Electric Propulsion Conference*, Colorado Springs, CO, May 11-13, 1987. AIAA 87-1093.

[78] H. Tahara, Y. Kagaya, and T. Yoshikawa. Hybrid MPD Thruster with Axial and Cusp Magnetic Fields. In 20^{th} *DGLR/AIAA/JSASS International Electric Propulsion Conference*, Garmisch-Partenkirchen, W. Germany, October 3-6, 1988. AIAA 88-058.

[79] Y. Arakawa and A. Sasoh. Steady-State Permanent Magnet MPD Thruster. In 19^{th} *AIAA/DGLR/JSASS International Electric Propulsion Conference*, Colorado Springs, CO, May 11-13, 1987. AIAA 87-1021.

[80] Y. Arakawa and A. Sasoh. Steady-State MPD Arc Thruster with a Permanent Magnet. *Journal of Propulsion and Power*, 4(3):287–288, 1988.

[81] R.M. Patrick and A.M. Schneiderman. Performance Characteristics of a Magnetic Annular Arc. *AIAA Journal*, 4(2):283 -290, 1966.

[82] E.Y. Choueiri and J.K. Ziemer. Quasi-Steady Magnetoplasmadynamic Thruster Measured Performance Database. In 34^{th} *AIAA Joint Propulsion Conference*, Cleveland, OH, July 13-16, 1998. AIAA 98-3472.

[83] Y. Tanabe, G. Burkhard, T. Ishikura, K. Tsunoda, H. Hasuo, M. Tamaru, H. Tamura, A. Sawaoka, and K. Uematsu. Characterization and Modification of Amorphous- Carbon Films Consisting of Sp(2) and Sp(3) Bonds Using Magneto-Plasma Dynamic Arc-Jet. *Japanese Journal of Applied Physics Part 1-Regular Papers, Short Notes and Review Papers*, 33(12A):6684–6690, 1994.

[84] Norton: A Leader in Diamond Film Manufacturing. Ceramic Bulletin, 70(2):205, 1991.

[85] T. Wegmann, M. Auweter-Kurtz, H.A. Habiger, H.L. Kurtz, and H.O. Schrade. Experimental Investigation of Steady State High Power MPD Thrusters. In 28^{th} *Joint Propulsion Conference*, Nashville TN, July 6-8, 1992. AIAA 92-3464.

[86] G.M. OConnor, C.J. McDonagh, T.J. Glynn, and G.P. Morgan. Material Characterisation Using Optical Spectroscopic Techniques. *Journal of Materials Processing Technology*, 56(1-4):211 221, 1996.

[87] T. Vandevelde, M. Nesladek, K. Meykens, C. Quaeyhaegens, L.M. Stals, I. Gouzman, and A. Hoffman. On Nitrogen Incorporation During PE-CVD of Diamond Films. *Diamond and Related Materials*, 7(2-5):152–157, 1998.

[88] Y. Vonkaenel, J. Stiegler, and E. Blank. Evolution of the Density of Graphite-Like Defects During CVD Diamond Growth. *Diamond and Related Materials*, 4(7):972–976, 1995.

[89] D.G. Goodwin. Scaling Laws for Diamond Chemical Vapor Deposition. II. Atomic Hydrogen Transport. *Journal of Applied Physics*, 74(11):6895–6906, 1993.

[90] W.G. Vincenti and C.H. Kruger. *Introduction to Physical Gas Dynamics*. John Wiley & Sons, 1965.

[91] H.M. Loh. *A Study of Diamond Synthesis in an Expanding Arcjet Plasma Flow*. PhD thesis, Stanford University, 1997.

[92] W. Griffith. Shock-Tube Studies of Transonic Flow over Wedge Profiles. *Journal of the Aeronautical Sciences*, pages 249–257, April 1952.

[93] J. Jeans. *An Introduction to the Kinetic Theory of Gases.* Cambridge University Press, 1967.

[94] F.M. White. *Viscous Fluid Flow.* McGraw-Hill, 1974.

[95] S.K. Baldwin. *Experimental Investigation of Atmospheric Pressure Nonequilibrium Plasma Chemistry for Plasma Assisted Chemical Vapor Deposition (PACVD) of Diamond Thin Films.* PhD thesis, Stanford University, 1996.

[96] E. Meeks. Modeling the Boundary-Layer Interactions Between Weakly Ionized Plasmas and Cooled, Planar Electrodes in Stagnation Point Flows. Technical Report HTGL Report No. T-293, Stanford University, 1993.

[97] H. Tawara, Y. Itikawa, H. Nishimura, and M. Yoshino. Cross Sections and Related Data for Electron Collisions with Hydrogen Molecules and Molecular-Ions. *Journal of Physical and Chemical Reference Data*, 19(3):617–637, 1990.

[98] H. Tawara, Y. Itikawa, H. Nishimura, H. Tanaka, and Y. Nakamura. Cross Section Data for Collisions of Electrons with Hydrocarbon Molecules. *Nuclear Fusion*, 2(S):41–64, 1992.

[99] R. Eisberg and R. Resnick. *Quantum Physics of Atoms, Molecules, Solids, Nuclei, and Particles.* John Wiley & Sons, 1974.

[100] J.A. Miller and C.T. Bowman. Mechanism and Modeling of Nitrogen Chemistry in Combustion. *Progress in Energy and Combustion Science*, 15(4):287–338, 1989.

[101] C.H. Kruger. Nonequilibrium Effects in Thermal Plasma Chemistry. *Plasma Chemistry and Plasma Processing*, 9(4):435–443, 1989.

[102] W.M. Kays and M.E. Crawford. *Convective Heat and Mass Transfer.* McGraw-Hill, 1980.